Friedel oscillations and the Fermi wavevector in low-dimensional ultracold Fermi gases

von
Keno Riechers

MIN-Fakultät
Fachbereich Physik
Masterarbeit im Studiengang Physik

Institut für Laserphysik
Universität Hamburg
Dezember 2016

Erstgutachter: Prof. Dr. Henning Moritz
Zweitgutachter: Prof. Dr. Ludwig Mathey

Abstract

This thesis addresses the question whether Friedel oscillations are observable in ultracold atomic Fermi gases based on the example of our experimental setup. The influence of the precise potential shape as well as the temperature on Friedel oscillations that emerge from a central barrier in a one-dimensional box-shaped potential is studied in a numerical simulation. Furthermore, a method to flatten an inhomogeneous potential by means of a digital micromirror device is presented which was tested in a simulation and remains to be implemented in the experiment. In order to predict the visibility of the Friedel oscillations a detailed analysis of the experimental signal to noise is carried out. After all the results suggest that an observation of Friedel oscillations is in general possible in our experiment. Yet, it will be challenging and an average over multiple absorption images will be required for significant reduction of the photon shot noise. Other experiments that work with heavier fermionic atoms or with higher resolutions are found to be more suitable for this intent. Furthermore, this work reports on experiments based on the Kapitza-Dirac effect that were used for the characterization of the magnification of our imaging system and the calibration of an optical lattice. The theory of this effect and the evaluation of the data are discussed in detail. Last, a comparison between in-situ and time of flight images of a two-dimensional non-interacting homogeneous Fermi gas is presented that allowed for the determination of the Fermi vector and to give an upper bound on the temperature of the system.

Zusammenfassung

Diese Arbeit diskutiert anhand des Beispiels unseres Experiments, ob Friedel Oszillationen in ultra-kalten atomaren Fermi Gasen beobachtbar sind. Der Einfluss der Form des Potentials sowie der Temperatur auf die Friedel Oszillationen, die von einer Barriere in einem eindimensionalen kastenförmigen Potential hervorgerufen werden, wird im Rahmen einer numerischen Simulation untersucht. Es wird ferner eine Methode eingeführt, um mit Hilfe eines 'digital micromirror device' Inhomogenitäten eines Potentials auszugleichen. Diese Methode wurde in einer Simulation getestet, die experimentelle Implementation steht noch aus. Um die Sichtbarkeit der Friedel Oszillationen zu beurteilen, wird eine detaillierte Analyse des Signal zu Rausch Verhältnisses durchgeführt. Unter Berücksichtigung all dieser Aspekte scheint es möglich, Friedel Oszillationen in unserem Experiment zu beobachten. Voraussichtlich wird eine solche Beobachtung eine experimentelle Herausforderung darstellen und eine Mittelwertbildung über mehrere Absorptionsabbildungen der Dichteverteilung erfordern. Darüber hinaus werden Experimente vorgestellt, bei denen der Kapitza-Dirac Effekt ausgenutzt wurde, um die Vergößerung unseres Abbildungssystems zu charakterisieren sowie ein optisches Gitter zu kalibrieren. Zuletzt werden Messungen von der Expansion eines zweidimensionalen, nicht-wechselwirkenden und homogenen Fermi Gases vorgestellt. Anhand eines Vergleiches von in-situ Bildern mit Flugzeit Bildern konnten der Fermi Vektor und eine obere Grenze für die Temperatur des Systems bestimmt werden.

Contents

1 Introduction

In the sixties Jacques Friedel intensively investigated the electronic structure of metals and alloys [1–3]. In particular he aimed to describe the mechanism of charge screening on a quantum mechanical level. A side product of his research was the theoretical prediction of an oscillatory behavior of the electronic density around an impurity potential, the so-called Friedel oscillation. Friedel himself did not pay much regard to this discovery because it did not provide net charge for the screening.

> "More generally, for any given perturbation V_p the oscillating term [...] will give rise to similar interference fringes, which should be computed in the same way. This has not been done so far, but the resulting effect should not be very important." (Friedel, 1954 [3])

Friedels rather skeptical stance appeared to be a considerable underestimation of his own findings. Today they are known to mediate long range interactions between individual impurities which are responsible for adsorbative phenomena and magnetic properties [4–6].

> "Their analysis provides a direct observation of screening and of electron-electron interaction. Moreover, these oscillations lie at the foundation of the description of the indirect coupling between magnetic moments via the conduction electrons in a metal with the famous Ruderman-Kittel-Kasuya-Yosida (RKKY) interaction potential, as well as of the long-range adsorbate interaction mediated by a two-dimensional electron gas." (Bena, 2016 [7])

Friedel oscillations have first been observed by Crommie et al. in 1993 on the surface of copper [8]. By means of scanning tunneling microscopy (STM) they uncovered standing wave patterns emerging from steps and point defects in the electronic local density of states $n(\mathbf{r}, E)$ as shown in Figure 1.1. By relating the wavelength of the

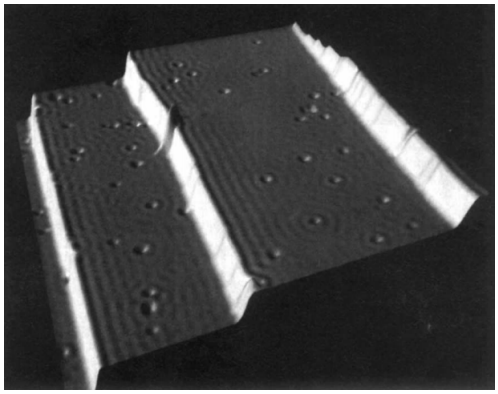

Figure 1.1: Direct observation of Friedel oscillations via scanning tunneling microscopy, reprinted from [8]. Friedel oscillations with a wavelength of $\sim 15\,\text{Å}$ emerge from steps or point defects in the surface of copper.

oscillation to the electron energy the analysis of Friedel oscillations became a powerful tool for the determination of electronic band structures [8–11]. As the research on Friedel oscillations proceeded anisotropic oscillations were reported [12] as well as inelastic Friedel oscillations [13], Friedel oscillations in one-dimensional electron gases [14] or oscillations whose giant amplitude is not captured by Friedels one-particle scattering picture, suggesting that more sophisticated many-body mechanisms are at work which enhance the oscillations [4]. Still, new applications and implications of Friedel oscillations are being discovered, clearly showing that their potential has not yet been exploited to its full extent. For example, Friedel oscillations may provide access to chiral properties of the Dirac electrons in graphene or to information about the underlying model describing high temperature superconductivity [7]. Further theoretical studies investigate the impact of Friedel oscillations on the critical properties and phase behaviors of 2D and 3D systems [15] or propose to focus Friedel oscillations by manipulating Fermi surfaces and thereby to tailor long range interactions [16].

In this thesis, I investigate whether Friedel oscillations can be observed in ultracold dilute atomic gases. Ultracold fermionic gases have been cooled to quantum degeneracy for the first time at the turn of the century [17] and since then have emerged as a novel platform to study fundamental concepts of many-body physics in highly controllable experimental model systems. Achievements include the observation of the superfluid to Mott insulator transition [18] and the realization of superfluids in the crossover from Bose-Einstein condensation (BEC) to Bardeen-Cooper Schrieffer (BCS) type superfluids [19–21]. However, Friedel oscillations have not been observed yet in ultracold atomic gases. Neither are we aware of a theoretical study investiga-

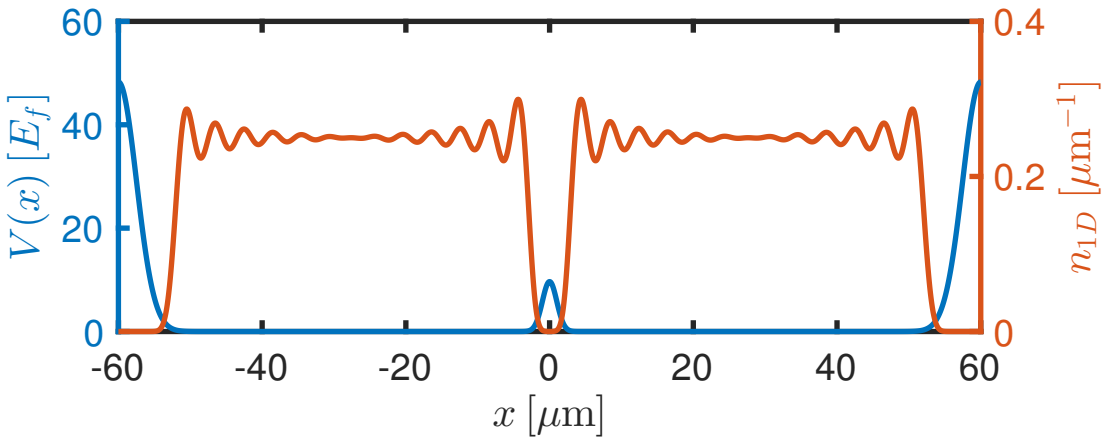

Figure 1.2: Numerically calculated density distribution of non-interacting fermions in a one-dimensional box-like test potential measured in units of the Fermi energy E_f. Friedel oscillations arise at the walls closing the box from both sides as well as at the barrier that is placed in the center of the box.

ting whether it is feasible to observe them in this framework. Here, I study the latter issue in the context of an experiment in the group of Prof. Moritz that seems particularly well suited to the task. The experiment has already allowed the determination of the critical velocity of a superfluid over the BEC-BCS crossover [17]. Within the time frame of this thesis we have been able to create homogeneous two-dimensional Fermi gases. The following route towards the observation of Friedel oscillations seems to be promising: First, the 2D cloud is separated into an array of one-dimensional gases, since in 1D Friedel oscillations should decay with with $1/r$ instead of $1/r^2$. Then, a thin barrier could be imprinted at the center of each tube, giving rise to Friedel oscillations in the density as shown in Figure 1.2. These would be observed with absorption imaging in real space with a spatial resolution of about 1 µm.

The approach outlined above has the potential to complement the STM method, which until today is the only method to observe Friedel oscillations. Whereas STM is limited to the observation of low dimensional surface states of materials, absorption imaging of ultracold gases could in principle resolve Friedel oscillations in the bulk. Besides, using STM the interactions are always determined by the properties of the sample. In experiments with a spin mixture of ultracold fermions, the interaction between the spins is tuneable via Feshbach resonances [22]. This would allow to investigate the dependence of the Friedel oscillations on the interactions systematically. Besides, the surfaces that can be examined with STM always couple to their carrier with a finite strength, hence it remains questionable how two-dimensional

(one-dimensional) these systems really are. Within the framework of ultracold atoms it is possible to generate low dimensional systems with a highly suppressed coupling to higher dimensions. Another striking difference is that absorption imaging may allow for the dynamical study of Friedel oscillations: impurities can be added and densities can be measured on microsecond timescales which is much faster than the millisecond timescales of the system dynamics associated with the Fermi energy. In contrast, dynamics in the solid state happen on femtosecond timescales exceeding the STM time resolution which is on the order of nanoseconds. Finally, whereas the STM measures the local density of states but not the electronic particle density as a whole, absorption imaging of ultracold gases does the opposite. Correspondingly, STM detects standing wave patterns in the density of electrons with a specific energy below or equal the Fermi energy. Ultracold atoms are not suitable for energy resolved imaging, but they could make Friedel oscillations in the strict sense amenable, i.e. the oscillations in the total electronic density.

Transferring the problem from solid state physics to an experiment with ultracold atoms may offer new and complimentary insights into Friedel oscillations but also raises other difficulties. A crucial factor for the distinctness of Friedel oscillations and therewith their visibility is the temperature in units of the Fermi temperature T/T_f and here values below 0.07 have not been reliably reached with weakly interacting Fermi gases, in contrast to solids. Regarding the temperature measured in units of the Fermi temperature, the signal to noise ratio and the resolution the performance of STM exceeds the one of an experiment with ultracold atoms significantly. However, if an observation of Friedel oscillations with ultracold atoms was possible, this would literally invite to experiment with different combinations of periodic potentials and interaction strengths as well as time dependent impurities. In particular this approach promises new insights into the role of interactions in 1D and 2D. Since in one-dimensional systems in the presence of interactions “no individual motion is possible [and] any individual excitation has to become a collective one” [23], they constitute a particularly interesting field of research. In this context predictions from Luttinger liquid theory could be reviewed experimentally [24]. Due to the high degree of control over system parameters Friedel oscillations in a gas of ultracold atoms would remove the restriction to the study of material specific quantities and open a straight access to the underlying fundamental physical relations. For these reasons we decided to investigate the feasibility of an observation of Friedel oscillations in an ultracold atomic Fermi gas.

I found that observing Friedel oscillation with sufficient statistical significance will be challenging in our experiment, despite the combination of high spatial resolution and long Fermi wavelengths achieved. The fact that the Friedel oscillations exhibit a wavelength proportional to $\lambda_f/2$, where λ_f denotes the Fermi wavelength of a system, demands a small particle density and a high resolution. In our case the resolution of $R \simeq 1\,\mu\text{m}$ forces us to work with very dilute samples with particle densities of $n_{2D} \simeq 1/4\,\mu\text{m}^{-2}$ resulting very low optical densities and hence in a small signal to noise ratio. Furthermore, very low temperatures and a high degree of homogeneity in the potential are required and it is questionable whether we can accomplish these demands. However, for researchers that work with heavier atoms than ^{6}Li and that can image the fermionic density with higher resolution the chance is higher to detect Friedel oscillations in a homogeneous cloud of ultracold fermions.

This thesis is structured as follows. I will briefly introduce our experiment, explain how we generate ultracold Fermi gases and sketch which types of potentials we can design by means of laser light and magnetic fields. In the third chapter I numerically simulate the expected density distribution of non-interacting fermions in a one-dimensional test potential that we should be able to create in the experiment using optical dipole traps. I will show how such a potential can be realized and investigate the visibility of the resulting Friedel oscillations by comparing their amplitude to the amplitude of noise that we expect for the measurement. For this purpose an analysis of the corresponding signal to noise ratio is carried out. In the following two chapters two further research endeavors are documented which are partially related to the topic of Friedel oscillations. In the fourth chapter the characterization of an optical lattice based on the Kapitza-Dirac effect is treated. The lattice could have been used for the generation of one-dimensional systems that are ideal for the study of Friedel oscillation. Unfortunately it had to be disassembled for technical reasons. Besides, the data was used to determine the magnification of our imaging system with high accuracy. In the fifth chapter I present a method for the determination of the Fermi vector in a two-dimensional non-interacting homogeneous Fermi gas that could be generated within this thesis for the first time. The same method allows to determine an upper limit on the temperature of the system.

2 Experiments with ultracold atoms - a description of our setup

In our experiment we cool gases of neutral atoms down to temperatures where their physics are governed by the laws of quantum mechanics. Once these temperatures are reached, the atomic samples are used to investigate fundamental issues in many-body physics as for example the critical velocity in the BEC-BCS crossover [25] or the Berezinskii-Kosterlitz-Thouless (BKT) transition in a two-dimensional Bose gas [26]. For their manipulation we utilize laser light and magnetic fields that interact with the atoms via the dipole force, the radiation pressure and the Zeeman effect [27]. Here, the principles of the experiment shall be briefly presented to give the reader an impression of how we actually study ultracold gases. For a more precise description of our machine the interested reader is referred to the PhD thesis by Wolf Weimer [28] and by Kai Morgener [29].

Technical progress in the cooling of neutral atoms and the ability of tuning their interactions via Feshbach resonances has allowed for the realization of specific model systems with ultracold atomic gases at the end of the last century. Due to the high degree of control over their parameters these systems can be used to simulate many-body Hamilton operators that originally describe phenomena in condensed matter physics and to examine dependencies between physical quantities in isolation [30]. Below a critical temperature bosonic atoms form a Bose-Einstein condensate (BEC), which was first observed in 1995 [31, 32]. In our experiment we work with fermionic ^{6}Li-atoms, which under normal circumstances cannot condense due to the Pauli exclusion principle but instead form a degenerate Fermi gas. The first realization of a degenerate Fermi gas of ultracold atoms was reported by DeMarco and Jin in 1999 [17]. ^{6}Li was chosen for our experiment on the one hand because it exhibits a simple level scheme associated with good cooling features. On the other hand because it provides a broad magnetic Feshbach resonance which offers the possibility to tune the interaction between atoms in different spin states across the BEC-BCS crossover

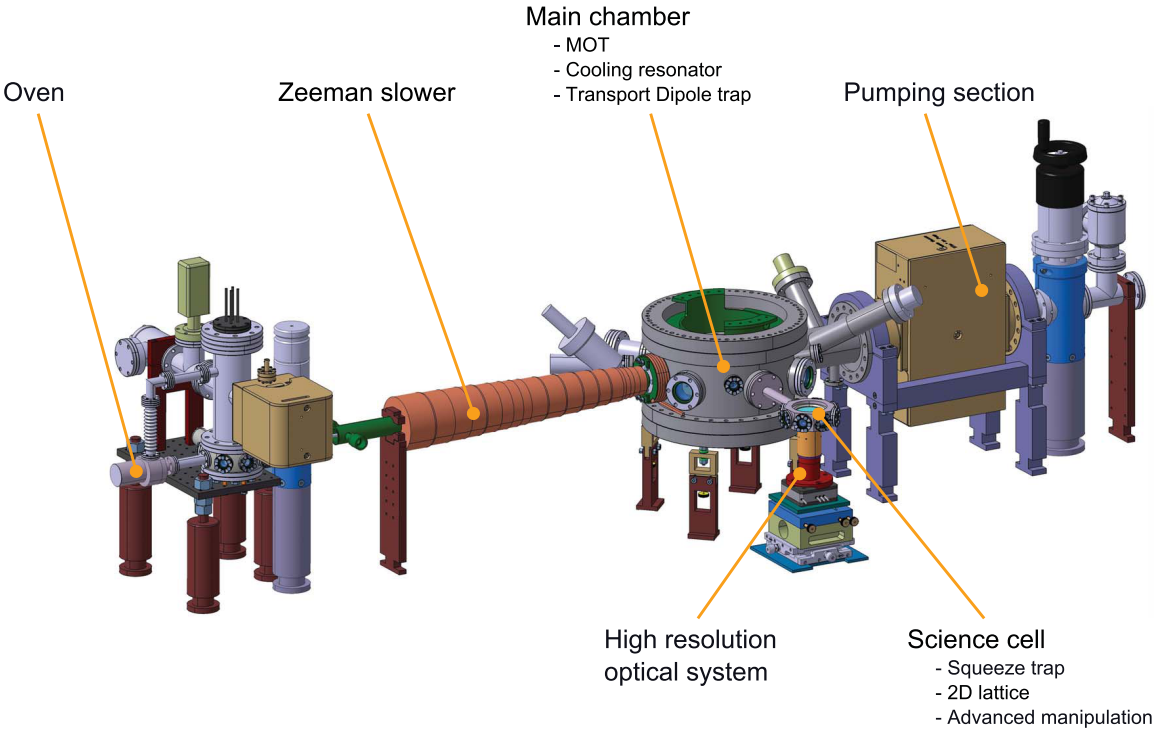

Figure 2.1: Overview of the vacuum system used for the preparation of degenerate Fermi gases with ^{6}Li. The high resolution optical system is referred to as microscope in the text. Reprinted from [28].

[28, 33].

The generation, the experimental manipulation and the observation of an ultracold Fermi gas, all takes place within about 15 seconds. The observation via absorption imaging destroys a sample at the end of each experimental cycle making it necessary to continuously generate new samples. Temperatures on the nanokelvin scale can only be achieved if the atomic gas is rigorously isolated from its environment, hence the whole procedure takes place inside a ultra-high vacuum system with a pressure of about $2 \cdot 10^{-11}$mbar which is shown in Figure 2.1.

Figure 2.2 gives an overview of all the steps that constitute one experimental cycle and that shall be individually explained in the following. A simple block of lithium heated in an oven to temperatures around 670 K provides a jet of atoms that we cool down to nanokelvins in a series of cooling steps. First, the collimated atomic jet passes through a Zeeman slower where the atoms are decelerated by a counterpropagating near resonant light beam. Each time an atom absorbs a photon its momentum

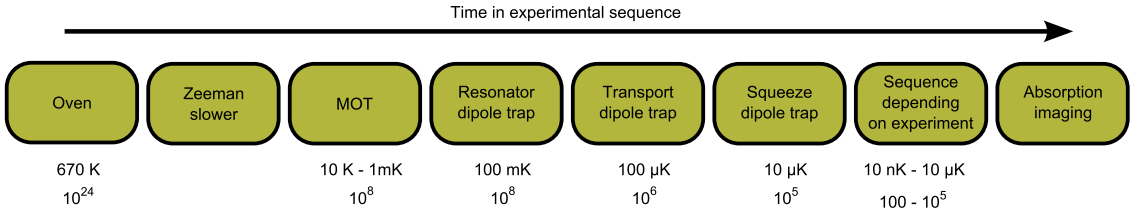

Figure 2.2: Schematic overview over the an experimental sequence. The numbers below the boxes indicate the approximate temperature scales which are relevant at the corresponding steps and the approximate number of particles. Reprinted from [28].

changes by $\Delta p = \hbar k$, where k denotes the wave vector of the photon pointing in the opposite direction as the atomic motion. In the cause of their deceleration the atoms are shifted out of resonance with the light due to the Doppler-shift. This effect is compensated by the application of a location-dependent magnetic field shifting the atomic energy levels, respectively. A detailed description of a Zeeman slower is given for example by Metcalf [27]. At the end of the Zeeman slowing stage the atoms are almost at rest and are captured in a magneto-optical trap (MOT) in the center of the main chamber. A MOT consists of a combination of a spatially varying magnetic field and six pairwise counterpropagating red-detuned laser beams whose common crossing point is located at the local minimum of the magnetic field. This setup induces an effective position and velocity dependent force on the atoms that results in further cooling as well as trapping of the atoms. MOT trapping has first been demonstrated in 1987 [34] and has continued to be the first major cooling step in a sequence for the preparation of ultracold atoms. However, its cooling capacity is ultimately limited by photon recoils. From the MOT the atoms are loaded into a red-detuned dipole trap consisting of two counterpropagating beams in an optical resonator that form a standing wave. This trap is used to perform a first evaporative cooling step and is correspondingly called cooling resonator.

Evaporative cooling is based on the loss of the hottest atoms of an ensemble [35]. By continuously reducing the trap depth atoms with highest energy are released from the trap. Efficient cooling requires that the remaining atoms rethermalize to a lower temperature equilibrium state. After the evaporation we transfer the atoms into a transport dipole trap which is a cigar shaped trap generated by a gaussian red-detuned laser beam. We call this trap the FORT trap, since the used laser light is **f**ar **o**ff-**r**esonan**t**. We shift the beam focus and thereby the center of the trap along the propagation direction of the beam by moving a corresponding lens which is mounted on an air bearing stage. This motion is slow enough for the atoms

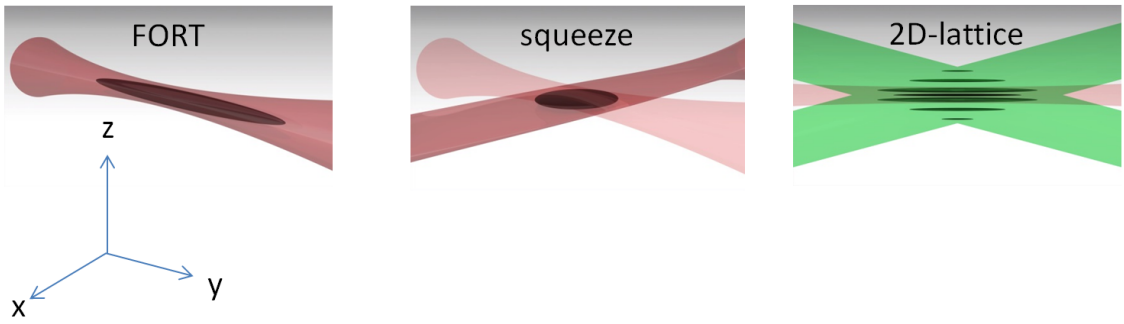

Figure 2.3: Schematic representation of the trap configuration in the science cell. From left to right: Cigar shaped red-detuned FORT trap (light red) with an cloud of trapped atoms (dark red). Pancake red-detuned shaped squeeze trap. 2D-lattice (dark green, except central ellipse), generated by the interference pattern of two crossed blue-detuned beams (light green) with atoms occupying a single layer (darkest and central ellipse). The figure is adapted from [36].

to follow the potential adiabatically. The final position is located in the so-called science cell, where we have good optical access and precise control over magnetic fields. There another evaporative cooling step is performed and subsequently the atoms are loaded into a pancake shaped optical trap that is provided by a highly elliptical beam characterized by its waists of $w_y = 370\,\mu\text{m}$ and $w_z = 10\,\mu\text{m}$. Since this trap squeezes the atomic cloud along the z-direction we call it the squeeze trap. The atomic pancake is orientated in the x-y-plane, i.e. parallel to the optical table and has only a small extent in the z-direction which is the imaging axis in our setup. Figure 2.3 schematically shows the configuration of the FORT, the squeeze and the 2D-lattice, which is introduced below.

From this point to the imaging process at the end of each cycle the sequence is determined by the individual experiment. After the manipulation of the atoms that constitutes the physical experiment we measure the two-dimensional column density via absorption imaging. For this purpose we apply a collimated resonant laser beam to the atoms that propagates along the z-axis. The atoms scatter photons from the beam and therefore cast a shadow. The imaging light propagates through a microscope resulting in 37.6 fold magnification. The resolution of the microscope is about $R = 1\,\mu\text{m}$. Finally the light is captured by a charge coupled device (CCD) camera. By comparing the recorded intensity from an image where atoms were present to an image where no atoms were present we can derive the two-dimensional column density, i.e. the three-dimensional density integrated along the propagation axis of the imaging beam.

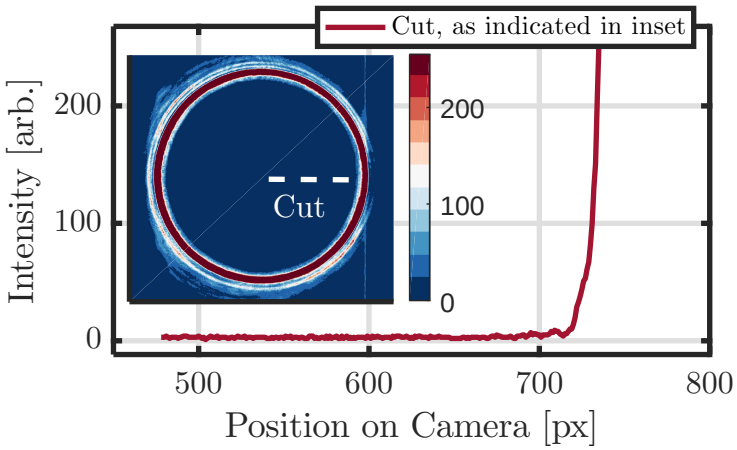

Figure 2.4: Intensity distribution of the ring beam along the section shown in the inset. The inset shows an image of the intensity distribution of the ring beam in the plane of the atoms. The camera was 200 times saturated at the position of maximum intensity. The effective pixel size is approximately 0.4 µm.

Regarding the part of the cycle which constitutes the actual experiment, our machine offers a broad range of tools. To give the reader an impression of the manifold options we have to manipulate the atoms we introduce the main features of our setup in the following. For example we can load the atomic gas into a single layer of a blue-detuned one-dimensional optical lattice. The energy spacing between the ground state and the first excited state exceeds all relevant energy scales making the sample quasi-2D. Since this lattice is used for the creation of a two-dimensional quantum system it is called 2D-lattice in our group. It is described in more detail in the master thesis by Klaus Hueck [36]. Two-dimensional systems have already been studied since 2001 [37–39], but still there remains a lot of physics to explore in two dimensions. The setup included a further red-detuned laser beam, the so called +x-y-lattice beam where +x-y indicates the direction of the beam propagation. It was retro reflected to create a second optical lattice perpendicular to the 2D-lattice. Combining the two lattices we can reduce dimensionality even further. The resulting potential consists of 1D tubes of low potential energy where the atoms accumulate. Also one-dimensional systems have been generated before for example by Goerlitz et al. and Moritz et al. [37, 40, 41]. Nonetheless, 1D systems offer a vast field of research possibilities.

The newest tools added to our experiment are a ring shaped trap and a digital micromirror device (DMD). The ring trap is realized by a blue-detuned laser beam propagating along the z-direction whose intensity profile has the shape of a ring in the

x-y-plane. This unique intensity distribution displayed in Figure 2.4 is achieved with the means of three axicons that split a gaussian beam in its center. The radius of the ring is adjustable from roughly $R \simeq 30\,\mu m$ to $R \simeq 250\,\mu m$ and its width is of the range of $20\,\mu m$ depending the radius and on the power of the ring beam. By loading the atoms into the combined potential provided by the ring trap and the 2D-lattice we can create a homogeneous Fermi gas, a system that had not been generated with ultracold atoms before. The DMD is a surface consisting of 1920×1080 mirrors. Each mirror has a linear size of $7.56\,\mu m$ and can individually be activated or deactivated. We illuminate the DMD with a gaussian beam of blue-detuned laser light and focus the reflected beam onto the position of the atoms. The beam enters the science cell from above, hence it propagates along the z-axis. This tool allows us to design arbitrary potential landscapes in the horizontal plane, limited only by the resolution of the DMD optics and the effective pixel size of a DMD pixel at the position of the atoms. No matter what optical trap configuration we chose for an experiment, we can always control the interactions between the ^{6}Li-atoms of different spin by applying suitable magnetic fields. This survey over our experimental toolkit is not complete and further tools will be added in the future.

During my time as a master student in the group the maintenance and the improvement of the machine required significant effort, which allowed us to generate homogeneous non-interacting Fermi gases for the first time. I investigated in the idea to disturb such a homogeneous Fermi gas by introducing an impurity potential with the DMD and thereby to observe the so-called Friedel oscillations. Furthermore, the Fermi vector of the homogeneous and non-interacting Fermi gas could be approximately determined and measurements with the +x-y-lattice based on the Kapitza-Dirac effect in order to calibrate the lattice and to characterize the magnification of the imaging system were performed.

3 Observation of Friedel oscillations in ultracold Fermi gases - a feasibility study

Consider a system with a homogeneous potential. The particle density in such a system must reflect the form of the potential and therefore be homogeneous as well. But what happens if an impurity is introduced into the system? For example think of a homogeneous electrolyte containing positive and negative ions, where the positive ions are assumed to be much heavier and almost immobile, such that the negative ions move in the present of an almost homogeneous background potential. Now a further ion - an impurity - carrying the positive charge $Q_{impurity}$ is added inducing a change δn in the density distribution of the negative ions with respect to the undisturbed density. Even though the coulomb interaction is long-ranged we expect the effect of the impurity to be of local character, hence its associated effective potential must be restricted to an area of finite size. This effect is called screening and originates from an accumulation of carriers of opposite charge with respect to the additional ion. It is treated in standard textbooks as the ones by Kittel [42] or Ashcroft and Mermin [43]. The change δn in the density corresponds to a change of the charge δQ which is located within a finite area around the impurity. To guarantee screening of the impurity the total charge inside this area must be close to zero, such that the net electric field outside this area is almost zero as well. Hence, the screening demands $\delta Q \simeq -Q_{impurity}$, i.e. the change of the local charge has to compensate the charge of the impurity. At large enough distance from an impurity the system obviously recovers its undisturbed density n_0. But what happens in the vicinity of the impurity and on which length scale is the perturbation of the system? In the framework of classical electrodynamics an answer to this question has been given by Debye and Hueckel for the case that the screening charges are carried by a classical fluid as in the case of the electrolyte [44]. Their findings revealed a decay of the

perturbation in the screening charge density of the form $\delta n \propto \exp(-\kappa r)/r$, where r is the distance to the impurity and $1/\kappa \propto \sqrt{T}$ defines a length scale for the damping of the perturbation depending on the temperature T.

However, for quantum mechanical systems this explanation fails and it was left to Friedel to give an appropriate explanation for the distribution of the electrons screening an impurity inside a metal [3]. Friedel's main concern was to find a mechanism that explained the existence of localized supplementary charge that was supposed to screen the impurity charge quantum mechanically. Friedel related the phase shifts between unperturbed waves and waves scattered from an attractive impurity potential to the number of bound states existing in the vicinity the impurity and providing the required screening charge [1]. His solution included quasi as a side product an oscillating term in the perturbation of the electronic density

$$\delta n \propto cos(2k_f r)/r^3, \tag{3.1}$$

where k_f denotes the Fermi vector of the system of electrons. We will call the wavelength of this oscillation the Friedel wavelength $\lambda_{FO} = \pi/k_f$.[1] As this oscillatory term is zero on average, it cannot account for a net screening charge but still this oscillations is part of the screening mechanism. In contrast to the classical theory of screening equation (3.1) constitutes a long-range oscillatory modification of the perturbed density. What Friedel predicted to be *not very important* is nowadays called Friedel oscillation and was the starting point for quite a number of both, theoretical and experimental investigations.

Friedel found the oscillations within a scattering approach. Usually, already basic courses on quantum mechanics equip their participants with the necessary tools to derive Friedel oscillations in the framework of scattering theory for one special example, namely the backscattering of a plane from a one dimensional potential barrier. Consider a barrier of the form

$$V(x) = \Theta(a - |x|), \tag{3.2}$$

Θ being the Heaviside function. An incoming plane wave $\exp(\pm ikx)$ from the left or the right is partially reflected and partially transmitted. The interference of the incoming wave with the reflected part of the wave forms a standing wave of which the

[1] Within this work the subscript $_f$ stands for Fermi, whereas a capitol $_{FO}$ represents Friedel.

modulus squared oscillates with a spatial frequency of $2k$ giving rise to a wavelength of $\lambda = \pi/k$. In a fermionic many-body system the particle density reads

$$\langle \hat{n}(x) \rangle = \sum_{j=1}^{N} |\phi_j(x)|^2, \tag{3.3}$$

as shown later, where ϕ_j denote one-particle orbitals. Hence, all the standing waves from different wave vectors up to the Fermi edge add up. Since they oscillate in phase close to the barrier they interfere constructively, but the farther away from the barrier the more the standing waves dephase leading to destructive interference. The result is an oscillation whose wave vectors equals the largest wave vector involved and which decays with $1/|x|$. Whereas we discussed the screening of an attractive potential above, we now argued with a barrier representing a repulsive impurity. This is not problematic as a potential $V(x) = -\Theta(a - |x|)$ would also partially backscatter incoming plane waves, thus Friedel oscillations arise no matter whether the impurity potential is attractive or repulsive.

Remarkably, Friedel derived his theory in the approximation of quasi free electrons, i.e. without taking into account the interelectronic repulsion, which is actually required for the screening mechanism. Essentially he computed the interference of incoming plane waves with the corresponding scattered wave emerging from the interaction with an impurity, which is nothing but the three dimensional analogue to the derivation carried out above for one-dimensional backscattering. Today plenty of theory on Friedel oscillations is available incorporating the lattice structure of the crystal hosting the electrons as well as Coulomb interactions between electrons which had both been ignored by Friedel. Villain et al. give an overview about the different theoretical approaches for the description of Friedel oscillations [45] of non-interacting electrons in periodic potentials which can be found in more detail for example in common textbooks [46, 47]. The original scattering approach has been replaced by a linear response framework. In the non-interacting case the oscillatory part of the density perturbation caused by any well-behaved impurity potential can be compactly formulated as

$$\delta n(r) = \frac{sin(2k_f r + \eta_d)}{r^d}, \tag{3.4}$$

where $d = 1, 2, 3$ is the dimensionality of the system, r the distance from the radially

symmetric impurity potential and η_d is a dimensionality-dependent phase shift [48].[2] Regarding the interactions between electrons more profound theory is presented by Simion et al. or Egger and Grabert [48, 49]. Interactions between the electrons can be taken into account by describing them as a Fermi liquid in two and three dimensions. However, fermions in one dimension can rather be treated as a Luttinger liquid leading to nontrivial modifications of the Friedel oscillations [48]. For this case Egger and Grabert report a slower decay of the Friedel oscillations proportional to r^{-g} where $g < 1$ represents the Luttinger liquid interaction constant [24].

Answering the initial question we summarize that the fermionic particle density in the vicinity of an impurity exhibits oscillations with a spatial frequency of $2k_f$ due to quantum mechanical scattering. The amplitude of this oscillation decays with $1/r^d$ where d is the dimensionality of the system. Hence, there is no characteristic length scale on which the system recovers its undisturbed density and the perturbation is long-ranged. The precise shape of Friedel oscillations is influenced by interactions as well as by the temperature, but the characteristic sinusoidal behavior remains.

The theoretical prediction of Friedel oscillations could be verified experimentally in 1993 by Crommie et al. [8] by the observation of standing waves in the electronic local density of states (LDOS) $n(E, r)$ emerging from steps and point defects in the surface of Cu via scanning tunneling microscopy (STM).[3] This publication was followed by a number of articles reporting on Friedel oscillations in different materials all using STM [4, 9, 10, 14]. In scanning tunneling microscopy a conducting tip is brought close to a surface of a probe and a bias voltage between the tip and the probe is applied [50]. Even though there is no direct contact electrons can tunnel from the probe into the tip or vice versa. By scanning the surface with the tip and measuring the tunnel current information about the topographic and electronic structure of the surface can be obtained. The quantity dI/dV has been shown to be closely related with the LDOS, such that standing waves in the electronic density can be observed in an energy resolved fashion [51]. Figure 3.1 shows concentric oscillations in the LDOS around a point scatterer on the surface of InAs constituting energy resolved Friedel oscillations. Relating the electron energy ϵ which is determined by the bias voltage to the wavelength of the LDOS standing waves $\lambda = \pi/k$, where k denotes

[2] This formula holds only asymptotically for the vicinity of the impurity. Very close to the impurity the actual screening charge is localized and the precise form of δn deviates from equation (3.4) for $r \to 0$.

[3] The local density of states is defined as $n(E, r) = \sum_k |\psi_k(r)|^2 \delta(\epsilon - \epsilon_k)$ [45].

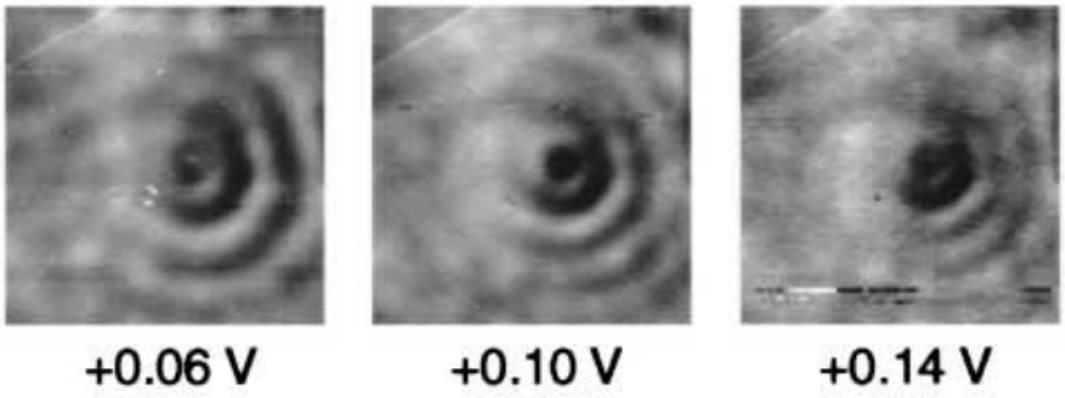

Figure 3.1: Oscillations of the LDOS in a 2D electron gas emerging from a point defect measured via scanning tunneling microscopy, reprinted from [10]. The three images correspond to three different bias voltages and therefore display $n(E, r)$ at three different energies E.

the wave vector of the scattered electronic wave function, opens up a straight access to the dispersion relation $\epsilon(k)$.[4] The experiments rely on the existence of so-called surface states, i.e. states which are localized at the surface of a probe [52]. Since these states constitute low dimensional systems the reported Friedel oscillations correspond mainly to 2D systems [4, 8–10]and rarely to 1D [14] systems. Three dimensional bulk states are not amenable with STM. The technique suffers from the fact that a finite interaction of the surface electrons with electrons in the bulk deforms the 2D band structure and therefore hinders the observation of effects caused by truly diminished dimensionality. Furthermore, the electronic density $n(r)$ remains undetectable for the scanning tunneling microscope and only the LDOS $n(E, r)$ can be measured in relative units.

This is where ultracold atoms come into play. Ultracold atomic gases nowadays offer the possibility to create generic fermionic systems with tunable interaction strengths, densities and dimensionalities [53]. New technologies provide options to design arbitrary potential landscapes with laser light [54]. An ultracold atom experiment is therefore the perfect instrument to extend the exploration of Friedel oscillations since the theory originally developed for electrons in metal applies as well for a homogeneous system of ultracold fermionic atoms disturbed by an impurity potential. Observations of Friedel oscillations in ultra cold atoms could provide a new access to the scattering properties of interacting fermionic system of desired dimensionality

[4]For the sake of clarity: the wavelength of the LDOS standing waves half the wavelength of the corresponding electronic wave function.

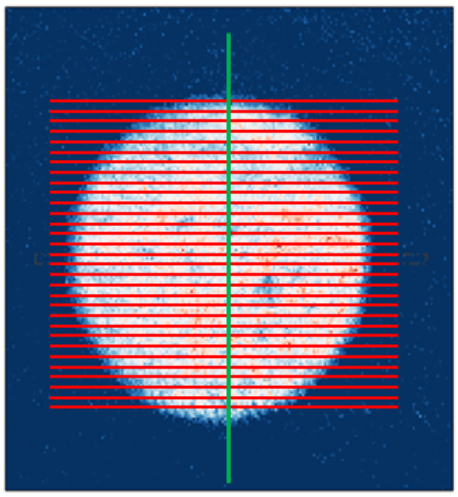

Figure 3.2: Preparation of 1D tubes. In the background the particle density of a homogeneous two- dimensional fermi gas is shown. The red lines schematically represent a red detuned optical lattice, that shall slice the atomic cloud into one-dimensional systems. The green line depicts a potential barrier created by blue detuned laser light.

and interaction strength. Furthermore, the emergence of Friedel oscillations could be studied in a time resolved manner in these systems. The effect of anisotropies on Friedel oscillations and regimes where wave vectors other than the Fermi vector contribute significantly to the Friedel oscillations [5] could be explored .

3.1 Experimental idea

Our experiment fulfills all the requirements to generate a homogeneous fermionic system either in one or two dimensions. With a DMD we can create small scale (few µm) disturbing repulsive potentials and we can tune the interactions between fermions of different spin over a broad range via a magnetic Feshbach resonance. It is tempting to try to observe Friedel oscillations that emerge from such an impurity. This work examines the feasibility of such an observation in one-dimensional systems. Since according to equation (3.4) the damping of the oscillations is the weakest in 1D, their visibility should enhanced compared to higher dimensional cases.

The basic idea is to slice a homogeneous 2D Fermi gas trapped in the ring trap and a single layer of the 2D-lattice into 1D tubes and then to create a sharp potential barrier in the center of the tubes (see Figure 3.2). An adequate tool to slice the 2D system into 1D tubes is an optical lattice. For the generation of such a lattice our

experiment provides various options. We can either retro-reflect the squeeze beam or the +x-y-lattice beam resulting in a red detuned lattice, or we can imprint a lattice with the DMD, which would deliver a blue detuned lattice. It remains to be tested in the experiment which of these possibilities is most suitable. For convenience we choose the direction of the tubes to be the x-direction and the direction perpendicular to it inside the 2D plane to be the y-direction in the following. Hence, the z-direction constituting the imaging axis of our experiment is perpendicular to the 2D plane of the atoms.[5] In the y-direction the lattice essentially creates a potential of the form $V(y) = V_l \cos^2(k_l y)$, concentrating the atoms in the individual lattice wells. For high enough lattice power tunneling of atoms between the wells is suppressed to negligible rates and in y direction only the ground state of a well is populated. In this case it is justified to speak of a 1D system. The potential we finally hope to generate with this setup along the x-axis is schematically shown in figure (3.3) together with the corresponding density distribution of non-interacting fermions that exhibits oscillations at the center and at the walls closing the boxlike potential. Why

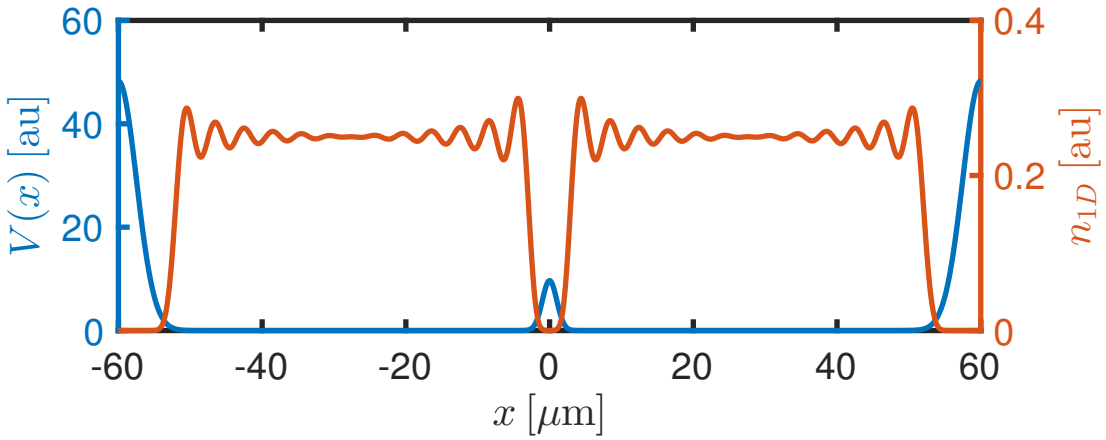

Figure 3.3: Qualitative plot of a one-dimensional potential proposed for the observation of Friedel oscillations together with the corresponding density distribution of non-interacting spinless fermions. Friedel oscillations emerge at the central barrier as well as at the walls closing the box from both sides.

is such a potential promising on the search for Friedel oscillations? Let us recall the eigenfunctions of a box with the radius a with infinitely high walls centered around

[5] The x and y direction might not coincide with the coordinate system of the laboratory introduced in Chapter 2 depending on the beam being used for the lattice.

the origin:

$$\phi_i(x) = \begin{cases} \sin(k_i[x+a]) & \text{for } |x| < a \\ 0 & \text{for } |x| > a \end{cases}, \tag{3.5}$$

where the k-vector is given by

$$k_i = i\frac{\pi}{L}, \text{ with } L = 2a \text{ and } i \in \mathbb{N}. \tag{3.6}$$

Obviously, inside the box each eigenfunction is characterised by a single momentum. For the infinitely high box the Fermi vector is simply given by

$$k_f = \frac{N}{L}\pi = n_{1D}\pi, \tag{3.7}$$

where N denotes the total number of particles in the box and n_{1D} is the one-dimensional particle density for a single spin component system. Inserting k_f into equation (3.4), we find for the wavelength of possible Friedel oscillations in such a 1D system:

$$\lambda_{FO} = \frac{2\pi}{2k_f} = \frac{1}{n_{1D}}. \tag{3.8}$$

As before, the Friedel wavelength originates from the shortest wavelength of the one-particle standing waves present in the system, namely $|\phi_f|^2$. It is logical to expect this wavelength to dominate the density profile close to an impurity potential, as it is the only characteristic wavelength in the system. This assumption is confirmed by the theory and by the experiment. Turning from a box potential with infinitely high walls towards our box-like potential the eigenfunctions maintain qualitatively their form, but the admixture of other momenta to the individual orbitals increases. Even though in the case of finite and smeared out walls the oscillation of $|\phi_f(x)|^2$ is not determined by a single wave vector anymore, its central wavelength remains to be $1/n_{1D}$. The contribution of higher momenta to the occupied eigenfunctions will probably alter the form of Friedel oscillations, but as long as the walls of the 1D tubes are of the height of several Fermi energies, the general structure of the wave functions as well as the Friedel oscillations remains the same as in the infinitely high box. Hence, it is reasonable to assume that Friedel oscillations with $\lambda_{FO} = 1/n_{1D}$ should be present in the potential introduced above.

These considerations show that our setup is in general suitable to provoke Friedel oscillations, yet nothing has been said so far regarding their visibility. Equation (3.8)

reveals two inherent opposing effects: On the one hand in order to image Friedel oscillations it is mandatory that the Friedel wavelength exceeds the resolution of our imaging system which makes a low density desirable. On the other hand a higher density leads to an improved signal to noise ratio in the absorption imaging required for a clear signal. As the resolution of our imaging system is given by $R \simeq 1\,\mu\text{m}$ the Friedel wavelength should at least be $\lambda_{Friedel} \simeq 4\,\mu\text{m}$, which requires a density of $\rho_{1D} \simeq 0.25\,\mu\text{m}^{-1}$. This guarantees that two zero-crossings of the Friedel oscillation are separated by about twice the resolution.

Let me now give a rough estimate on the signal to noise ratio that is achievable within this upper bound for the 1D density. A detailed discussion of the signal to noise ratio will be presented in Section 3.5. A calculation of the signal to noise ratio relies on a two-dimensional density, therefore it is required to relate the 2D density to the 1D density in the tubes. The lattice that shall slice the 2D system into 1D tubes would most likely be generated by retro-reflection of a laser with a wavelength of $\lambda = 1064\,\text{nm}$ resulting in a spacing between the tubes of 532 nm. Correspondingly, in the 2D treatment the particles from one tube are located within a stripe with a width of roughly $0.5\,\mu\text{m}$, such that the 2D density reads

$$n_{2D} \simeq n_{1D}/0.5\,\mu\text{m} = 0.5\,\mu\text{m}^{-2}. \tag{3.9}$$

In the simplest case ignoring saturation effects the absorption of photons is described by Beers law [55], giving rise to the following expression for the two-dimensional density:

$$n_{2D} = \frac{1}{\sigma_{abs}} \ln\left(\frac{N_{in}}{N_{out}}\right), \tag{3.10}$$

where $N_{in/out}$ is the number of incident/outcoming photons of an imaging beam that propagates through a cloud of atoms and $\sigma_{abs} = 3\lambda^2/2\pi$ is the absorption cross-section. Under the assumption that the only noise source is the photon shot noise on N_{in} and N_{out}, given by $\sigma_{N_{out}} \approx \sigma_{N_{in}} = \sqrt{N_{in}}$, due to error propagation the noise on n_{2D} then reads:

$$\sigma_{n_{2D}} = \sqrt{\frac{2}{\sigma_{abs}^2 N_{in}}}, \tag{3.11}$$

leading to a signal to noise ratio of

$$SNR = \frac{n_{2D}}{\sigma_{n_{2D}}} = n_{2D}\,\sigma_{abs}\sqrt{\frac{N_{in}}{2}}. \tag{3.12}$$

Typical for our setup are an imaging pulse of a duration of $\tau = 5\,\mu s$ and an intensity of $I = I_{sat} = \frac{\pi}{3}\frac{hc\Gamma}{\lambda^3}$ [55]. The number of photons hitting a single pixel is given by multiplying the intensity with the pulse duration and the effective pixel size $\Omega = 0.18\,\mu m^2$ and dividing by the energy of a single photon $E_{ph} = h\nu$.[6] For such an imaging pulse we find the number of incident photons to be $N_{in} \simeq 25$ per camera pixel. For a density of $n_{2D} = 0.5\,\mu m^{-2}$ the signal to noise ratio is $SNR = 0.38$. Averaging over k density images improves the SNR by a factor of $\sqrt{k}$. Hence, taking 1000 images would result in $SNR \simeq 12$. The word signal in this context refers to the entire particle density, but the signal we are really looking for is a density modulation. If the Friedel oscillations modulated the density by an amount of 10% of the average density which is shown to be realistic in Section 3.3 their amplitude would roughly equal the amplitude of the noise. Including technical noise and noise from leak light will affect the signal to noise ratio negatively, whereas on the positive side, our experimental setup allows for averaging the density distribution on the central tubes. If the density profile at the central barrier was exactly the same for each tube an average over 100 tubes would increase the signal to noise ratio by a factor of 10. However, in Section 3.4 we explain in detail how the homogeneous 1D tubes can be generated and show that fluctuations in the potential will differ from tube to tube. As a result the density profiles will slightly differ from one another as well and the enhancement of the signal to noise ratio by the average will be less efficient. Since this type of average is more sophisticated to quantify, the signal to noise ratio of 12 shall serve as an orientation for the moment. The tube average will be taken up again in Section 3.4.

From these considerations one can already conclude that a density of $n_{2D} = 0.5\,\mu m^{-2}$ is borderline regarding the signal to noise ratio. The density is not the only crucial parameter. We will show later that also the temperature and the quality of our potential have to fulfill very strict requirements for the observation of Friedel oscillations as well.

[6] The effective pixel size is the area in the plane of the atoms that corresponds to the area of a single pixel in the camera plane. Since the linear pixel size of the camera is $16\,\mu m$ and the magnification of the imaging system is 37.6 the effective linear pixel size is $0.43\,\mu m$ yielding an area of $\Omega = 0.18\,\mu m^2$.

3.2 Numerical simulation of Friedel oscillations in a 1D test potential

In the previous section very elementary considerations revealed that the 2D density in our setup must be around $n_{2D} \simeq 0.5\,\mu\text{m}^{-2}$ in order to observe Friedel oscillations in a one-dimensional potential. Besides, it became clear that the their visibility is not certain due to the corresponding signal to noise ratio. To understand this issue better before putting effort into the experimental realization, a simulation of the system was performed that predicted the amplitudes of the expected Friedel oscillations.

To attribute the density oscillations to the mechanism of Friedel oscillations we rely on the detection of at least two oscillations, since close to a potential barrier also other effects may cause an apparent density oscillation. For example, diffraction of the imaging light from sharp edges in the optical density can occur. As will be presented in Section 3.3 the simulation yielded Friedel oscillations emerging from a central barrier in 1D test potential with amplitudes of $\Theta_1 = 28\,\%$ and $\Theta_2 = 9\,\%$ for the first and second oscillation, respectively. Thereby, Θ_2 is comparable to the amplitude of the noise estimated for a 1000 image average disregarding a possible average over the 1D tubes.

From these findings I proceed with the analysis in Section 3.4 by incorporating imperfections in the potential and estimating the efficiency of averaging over tubes that provide each an individual density profile. Given that the deviations of the potentials are small compared to the Fermi energy the average significantly improves the signal to noise ratio yielding rather promising results. All together it can be stated that meaningful Friedel oscillations should be observable for the following parameters:

- density of around $0.25\,\mu\text{m}^{-1} \hat{=} 0.5\,\mu\text{m}^{-2}$
- temperature of less than $T = 0.1\,T_f$
- a flat potential with $\delta V << E_f$.

Since interactions are supposed to enhance Friedel oscillations, it might be easier to detect them in an interacting Fermi gas [4, 24].

In this section I present the numerical approach used to predict the density distribution in the 1D test potential introduced in Section 3.1. I will show that the many-body density of a system containing N non-interacting fermions at $T = 0$

reads

$$\langle \hat{n}(x) \rangle = \sum_{k=1}^{N} |\phi_k(x)|^2, \tag{3.13}$$

where the ϕ_k denote the eigenfunctions, also-called orbitals, of the one-particle Hamiltonian in ascending order in energy. For a finite temperature the sum has to be expanded over all eigenfunctions ϕ_k and weighted with the Fermi distribution $f(\epsilon_k)$, where ϵ_k denotes the corresponding energy of ϕ_k:

$$\langle \hat{n}(x, T, \mu) \rangle = \sum_{k=1}^{\infty} f(T, \mu, \epsilon_k) |\phi_k(x)|^2. \tag{3.14}$$

In both cases the one-particle densities add up independently. Subsequently the calculation of the one-particle orbitals is presented. For this intent I discretize the one-particle Schroedinger equation and solve it numerically for a finite grid on which we define a test potential. Once the eigenfunctions are known, the sums above can easily be carried out. Finally I will discuss the precise form of the test potential. The results of the simulations are presented in the subsequent section.

3.2.1 Derivation of the fermionic many-body density

Consider a one-dimensional system of N fermions without spin and without interparticle interactions. The theoretical description of such a system is straight forward, yet the derivation of the equations (3.13) and (3.14) require a lengthy calculation that is presented in detail here. We start with the Hamiltonian of the system given by

$$\hat{H}^N = \sum_{i=1}^{N} -\frac{\hbar^2}{2m} \frac{\partial^2}{\partial x_i^2} + V(x_i), \tag{3.15}$$

where x_i is the coordinate of the i-th particle and V is a one-particle potential, which is equal for all particles. Throughout this section the superscript N is used when it is necessary to stress that a quantity or an operator refers to an N-body-system for the sake of clarity. Let the set $\{\phi_i\}$ be the solutions of the eigenvalue problem given by the time independent Schroedinger equation for the one-particle problem:

$$\epsilon_i \phi_i(x) = \hat{H}^1(x) \phi_i(x) = \left(-\frac{\hbar^2}{2m} \frac{\partial^2}{\partial x^2} + V(x) \right) \phi_i(x). \tag{3.16}$$

Then the N-particle wave function of a pure quantum state to a given many-body energy E can be constructed via the Slater determinant:

$$\psi(x_1, x_2..., x_N) = \frac{1}{\sqrt{N!}} \begin{vmatrix} \phi_{W(1)}(x_1) & \phi_{W(2)}(x_1) & \dots & \phi_{W(N)}(x_1) \\ \phi_{W(1)}(x_2) & \phi_{W(2)}(x_2) & \dots & \phi_{W(N)}(x_2) \\ \vdots & \ddots & \ddots & \vdots \\ \phi_{W(1)}(x_N) & \phi_{W(2)}(x_N) & \dots & \phi_{W(N)}(x_N) \end{vmatrix} , \tag{3.17}$$

where W maps the set $\{1, 2, \dots, N\}$ onto a set of pairwise different integers determining the set of one-particle eigenfunctions being occupied in the many-body quantum state. The map W has to obey the condition

$$E = \sum_{i=1}^{N} \epsilon_{W(i)}. \tag{3.18}$$

Now that the many-body eigenstates are found one can evaluate the many-body particle density operator

$$\hat{n}(x) = \sum_{i}^{N} \delta(x - x_i). \tag{3.19}$$

First I will focus on the case $T = 0$ and later I will introduce a finite temperature. At zero temperature N fermions would simply occupy the N lowest energy eigenstates of the one-particle Hamiltonian. This configuration is the fermionic N-particle ground state $|\psi_N^0\rangle$. The expectation value of the density operator is given by:

$$\begin{aligned} \langle \hat{n}(x) \rangle = \langle \psi_N^0 | \hat{n}(x) | \psi_N^0 \rangle = \int_{-\infty}^{\infty} dx_1 \int_{-\infty}^{\infty} dx_2 \cdots \int_{-\infty}^{\infty} dx_N \\ \frac{1}{\sqrt{N!}} \sum_S \sigma(S) \prod_{i=1}^{N} \phi_{S(i)}^*(x_i) \sum_{k=1}^{N} \delta(x_k - x) \frac{1}{\sqrt{N!}} \sum_{S'} \sigma(S') \prod_{j=1}^{N} \phi_{S'(j)}(x_j). \end{aligned} \tag{3.20}$$

S denotes a permutation of the set $\{1, 2, ...N\}$ and $\sigma(S)$ is the corresponding parity of the permutation. The sum runs over all possible permutations of this kind. Here, the sums and the integrals interchange. Besides, in the product of wave functions the indices i and j both take all values from 1 to N, such that one of them can be eliminated. The equation can be rewritten as follows:

$$\langle \hat{n}(x) \rangle = \sum_{S,S'} \sum_{k=1}^{N} \int_{-\infty}^{\infty} \prod_{i=1}^{N} dx_i \frac{1}{N!} \sigma(S)\sigma(S') \phi_{S(i)}^*(x_i) \phi_{S'(i)}(x_i) \delta(x_k - x). \tag{3.21}$$

For any $S \neq S'$ the integral contains at least one dimension $x_p \neq x_k$ with $S(p) \neq S'(p)$, such that

$$\int_{-\infty}^{\infty} dx_p \phi^*_{S(p)}(x_p)\phi_{S'(p)}(x_p) = 0, \tag{3.22}$$

The integral vanishes due to the orthogonality of $\phi_{S(p)}(x_p)$ and $\phi_{S'(p)}(x_p)$. So, one finds for the density of the Fermi gas:

$$\langle \hat{n}(x) \rangle = \sum_S \sum_{k=1}^{N} \int_{-\infty}^{\infty} \prod_{i=1}^{N} dx_i \frac{1}{N!} \underbrace{\sigma(S)\sigma(S)}_{=1} \phi^*_{S(i)}(x_i)\phi_{S(i)}(x_i)\delta(x_k - x). \tag{3.23}$$

Integrating over all dimensions $dx_i \neq dx_k$ leads to

$$\langle \hat{n}(x) \rangle = \sum_S \sum_{k=1}^{N} \int_{-\infty}^{\infty} dx_k \frac{1}{N!} |\phi_{S(k)}(x_k)|^2 \delta(x_k - x). \tag{3.24}$$

The sum over k contains the same set of N orbitals independently from the permutation S. And as there exist precisely $N!$ permutations the particle density finally reads

$$\langle \hat{n}(x) \rangle = \sum_{k=1}^{N} |\phi_k(x)|^2. \tag{3.25}$$

Therefore the many-body density at position x equals the sum of the one-body densities of all occupied wave functions at position x. Giving up the restriction to the ground state and including higher energy but pure quantum states one finds:

$$\langle \hat{n}(x) \rangle = \sum_{k=1}^{N} |\phi_{W(k)}(x)|^2, \tag{3.26}$$

where again equation (3.18) holds.

In the experiment one deals with a grand canonical ensemble of atoms, so a finite temperature T has to be introduced as well as a finite chemical potential μ. Such a mixed state is appropriately described by the grand canonical density operator

$$\hat{\rho} = \frac{1}{Z} \exp(-\beta[\hat{H} - \mu\hat{N}]), \tag{3.27}$$

where $\beta = (k_B T)^{-1}$, k_B denoting the Boltzmann constant. $\hat{N}$ is the number operator that counts the number of particles in the system and Z is the grand canonical partition function

$$Z = \mathrm{Tr}\{\exp(-\beta[\hat{H} - \mu\hat{N}])\}. \tag{3.28}$$

The density profile of such a system with a given temperature and a given chemical potential has to be calculated by taking the trace over the product of the statistical density operator $\hat{\rho}$ times the real space particle density operator $\hat{n}(x)$.[7]

$$\langle \hat{n}(x) \rangle = \mathrm{Tr}\{\hat{\rho}\,\hat{n}(x)\} = \sum_{r,N=1}^{\infty} \langle \psi_r^N | \frac{1}{Z} \exp(-\beta[\hat{H}^N - \mu\hat{N}]) \hat{n}^N(x) | \psi_r^N \rangle \tag{3.29}$$

In this notion I made an implicit choice for the basis of the Hilbert space. Namely, the set of basis vectors contains all $|\psi_r^N\rangle$, which denote the N-particle eigenfunctions to the N-particle Hamiltonian with the energy $E_r^N|\psi_r^N\rangle = \hat{H}^N|\psi_r^N\rangle$. They are of the form described by equation (3.17). As the $|\psi_r^N\rangle$ are eigenfunctions of the number operator $\hat{N}$ as well one finds:

$$\langle \hat{n}(x) \rangle = \sum_{r,N=1}^{\infty} \frac{1}{Z} \exp(-\beta[E_r^N - \mu N]) \langle \psi_r^N | \hat{n}^N(x) | \psi_r^N \rangle, \tag{3.30}$$

such that equation (3.26) can be inserted for each N:

$$\langle \hat{n}(x) \rangle = \sum_{r,N=1}^{\infty} \frac{1}{Z} \exp(-\beta[E_r^N - \mu N]) \sum_{j=1}^{N} |\phi_{W_r(j)}(x)|^2. \tag{3.31}$$

Instead of summing over the index of the N-particle eigenenergies r one can equivalently sum over all possible sets of occupation numbers $\{n_j\}^N$ with $\sum_i n_i = N$ that denote which orbitals are occupied in the N-particle state.

$$\langle \hat{n}(x) \rangle = \sum_{N=1}^{\infty} \sum_{\{n_i\}^N} \left\{ \frac{1}{Z} \exp(-\beta \sum_i n_i[\epsilon_i - \mu]) \sum_j n_j |\phi_j(x)|^2 \right\} \tag{3.32}$$

The sum in the exponent can be transformed into a product of exponential functions:

$$\langle \hat{n}(x) \rangle = \sum_{N=1}^{\infty} \sum_{\{n_i\}^N} \left\{ \frac{1}{Z} \prod_{i=1}^{\infty} \exp(-\beta n_i[\epsilon_i - \mu]) \sum_j n_j |\phi_j(x)|^2 \right\}. \tag{3.33}$$

[7] Do not be confused by the names of the operators. The statistical density operator describes the probability to find the whole system in a certain pure quantum state, whereas the particle density operator evaluates the particle density of such a pure state in real space.

Rewriting the sum $\sum_{N=1}^{\infty}\sum_{\{n_i\}^N} \hat{=} \sum_{n_1=0}^{1}\sum_{n_2=0}^{1}\dots$ leads to the form:

$$\begin{aligned}\langle\hat{n}(x)\rangle =&\frac{1}{Z}\sum_{n_1=0}^{1} e^{-\beta n_1(\epsilon_1-\mu)}\sum_{n_2=0}^{1} e^{-\beta n_2(\epsilon_2-\mu)}\dots\left(n_1|\phi_1(x)|^2+n_2|\phi_2(x)|^2\dots\right)\\ =&\frac{1}{Z}\sum_{n_1=0}^{1} e^{-\beta n_1(\epsilon_1-\mu)}n_1|\phi_1(x)|^2\prod_{j\neq 1}\sum_{n_j=0}^{1} e^{-\beta n_j(\epsilon_j-\mu)}\\ &+\frac{1}{Z}\sum_{n_2=0}^{1} e^{-\beta n_2(\epsilon_2-\mu)}n_2|\phi_2(x)|^2\prod_{j\neq 2}\sum_{n_j=0}^{1} e^{-\beta n_j(\epsilon_j-\mu)}\dots\\ =&\frac{1}{Z}\sum_{k=1}^{\infty}\sum_{n_k=0}^{1} e^{-\beta n_k(\epsilon_k-\mu)}n_k|\phi_k(x)|^2\prod_{j\neq k}\sum_{n_j=0}^{1} e^{-\beta n_j(\epsilon_j-\mu)}\end{aligned} \tag{3.34}$$

executing the sum $\sum_{n_j=0}^{1} e^{-\beta n_j(\epsilon_j-\mu)} = 1+e^{-\beta(\epsilon_j-\mu)}$ and using the expression for the grand canonical partition function $Z=\prod_l\left(1+e^{-\beta(\epsilon_l-\mu)}\right)$ the density reads

$$\begin{aligned}\langle\hat{n}(x)\rangle &= \sum_{k=1}^{\infty} e^{-\beta(\epsilon_k-\mu)}|\phi_k(x)|^2\frac{\prod_{j\neq k}\left(1+e^{-\beta(\epsilon_j-\mu)}\right)}{\prod_l\left(1+e^{-\beta(\epsilon_l-\mu)}\right)}\\ &= \sum_{k=1}^{\infty}\frac{e^{-\beta(\epsilon_k-\mu)}}{1+e^{-\beta(\epsilon_k-\mu)}}|\phi_k(x)|^2\\ &= \sum_{k=1}^{\infty} f(\epsilon_k)|\phi_k(x)|^2\end{aligned} \tag{3.35}$$

where $f(\epsilon_k)$ denotes the Fermi distribution function.

3.2.2 Numerical method for the calculation of the fermionic density in a 1D potential

The results from the previous section show that knowing the one-particle wave functions and its energies for a given 1D potential enables to calculate many-particle density profiles for zero or finite temperature. Still, the orbitals ϕ_i and their corresponding energies ϵ_i need to be found. Here, I present how the orbitals can be calculated numerically. The starting point is the one-particle stationary Schroedinger equation:

$$\epsilon_i\phi_i = \hat{H}\phi_i = \left(-\frac{\hbar^2}{2m}\frac{\partial^2}{\partial x^2}+V(x)\right)\phi_i. \tag{3.36}$$

The index i denotes the index of the different solutions to this equation in ascending order in energy. In order to solve the eigenvalueproblem of the stationary Schroedinger equation numerically, one has to discretize the system. I restrict the system size to the finite length L and introduce a finite grid with a grid point spacing of Δx. Hence the number of grid points is given by $l = L/\Delta x$. Any continuous function $f(x)$ can be converted into its discrete counterpart $f(k) := f(k\Delta x)|k \in \mathbb{Z}$.[8] The derivative is then expressed by

$$\frac{\partial f(x)}{\partial x} \to \frac{f(k+1) - f(k)}{\Delta x}. \tag{3.37}$$

The second derivative has to be performed symmetrically around the point of interest.

$$\frac{\partial^2 f(x)}{\partial x^2} \to \frac{f(k+1) - 2f(k) + f(k-1)}{(\Delta x)^2} \tag{3.38}$$

Correspondingly, the discretized Schroedinger equation reads

$$\epsilon_i \phi_i(k) = -\frac{\hbar^2}{2m} \frac{\phi_i(k+1) - 2\phi_i(k) + \phi_i(k-1)}{\Delta x^2} + V(k)\phi_i(k). \tag{3.39}$$

To write this in a more compact form I introduce the constant $\alpha = \hbar^2/(2m \cdot \Delta x^2)$, such that the Schroedinger equation can be written as

$$\bar{\epsilon}_i \phi_i(k) = -\phi_i(k+1) + 2\phi_i(k) - \phi_i(k-1) + \bar{V}(k)\phi_i(k), \tag{3.40}$$

where $\bar{\epsilon}_i = \frac{\epsilon_i}{\alpha}$ and $\bar{V}(k) = \frac{V(k)}{\alpha}$. Correspondingly, the normalized Hamilton operator is defined as:

$$\bar{H} = \frac{\hat{H}}{\alpha}. \tag{3.41}$$

As a basis of the Hilbert space a set of step functions $\{\varphi_i(k)\}$ is chosen being equal to 1 at precisely one gridpoint and zero everywhere else:

$$\varphi_i(k) = \begin{cases} 1 \text{ for } k = i \\ 0 \text{ else} \end{cases}. \tag{3.42}$$

The finite number of grid points therefore truncates the Hilbert space which is actually of infinite dimensionality, as at least the unbound spectrum of the Hamilton operator

[8] Commonly the argument of a discrete function is written as an index f_k, but as the index is needed to indicate the energy level, I put the argument in brackets $f(k)$. Just keep in mind, that k is not a continuous variable.

contains an infinite number of eigenfunctions. As only the low energy bound sates are of interest this truncation is reasonable. The general formula for the matrix formulation of the Hamilton operator

$$\bar{H}_{ij} = \langle \varphi_i | \bar{H} | \varphi_j \rangle \tag{3.43}$$

leads to the following Hamilton matrix:

$$\bar{H} = \begin{bmatrix} 2+\bar{V}(1) & -1 & 0 & & \dots & 0 \\ -1 & 2+\bar{V}(2) & -1 & 0 & & \\ 0 & -1 & 2+\bar{V}(3) & -1 & & \vdots \\ \vdots & & \ddots & \ddots & \ddots & 0 \\ & & & & & -1 \\ 0 & \dots & & 0 & -1 & 2+\bar{V}(l) \end{bmatrix}. \tag{3.44}$$

The eigenvectors of this matrix are the discretized eigenfunctions $\phi_j(k)$ of the Hamilton operator and the eigenvalues are the corresponding eigenenergies ϵ_j. Due to the choice of the basis, the k-th entry in the j-th eigenvector equals the value of the j-th orbital at the grid point k. There are many ways to diagonalize a matrix numerically. I used the program Matlab that provides the command `[phi,e]=eig(H)` for this purpose. `e` returns the diagonalized matrix and `phi` is a matrix whose i-th column contains the normalized eigenvector to the i-th eigenvalue of $\bar{H}$, that is, to the entry `e(i,i)`. Hence, the energies and their corresponding wave functions are given by

$$\epsilon_i = \alpha \texttt{e(i,i)} \tag{3.45}$$

$$\phi_i = \texttt{phi(:,i)}. \tag{3.46}$$

Once the eigenfunctions ϕ_i are found, one can directly evaluate the expression for the density of the N particle fermionic system either for zero or for finite temperature.

$$\langle \hat{n}(k) \rangle = \begin{cases} \sum_{i=1}^{N} |\phi_i(k)|^2 & \text{for } T = 0 \\ \sum_{i=1}^{\infty} f(\epsilon_i) |\phi_i(k)|^2 & \text{for } T \neq 0 \end{cases} \tag{3.47}$$

For the finite temperature case the chemical potential μ still needs to be quantified. In the experiment the total number of atoms in the grand canonical ensemble can be

controlled which is determined by the chemical potential via the following equation:

$$\langle \hat{N} \rangle = Tr\{\hat{\rho}\hat{N}\} = \sum_{i=1}^{\infty} \frac{1}{\exp(\beta[\epsilon_i - \mu]) + 1} \rightarrow \int_0^{\infty} f(\epsilon) g(\epsilon) d\epsilon \tag{3.48}$$

Here $g(\epsilon)$ denotes the density of states. For zero temperature the number of atoms defines the Fermi energy which is at the same time the chemical potential. For low temperatures the equation

$$\langle N \rangle \simeq N \tag{3.49}$$

holds, as one uses the Fermi energy of a corresponding N particle system at $T = 0$ for the chemical potential of the thermal system:

$$\mu = \epsilon_N. \tag{3.50}$$

Since only small temperatures shall be investigated, this is an adequate choice for the chemical potential.

3.2.3 Specification of the 1D test potential

For the numerical treatment of the system an adequate description of the potential is required. In this section I quantify the test potential with respect to the conditions in our experimental setup. Experimentally the generation of homogeneous 1D tubes is challenging because a red detuned optical lattice as proposed for this purpose in Section 3.1 exhibits a confining potential along the tube axis due to the intensity distribution of the gaussian beam. Regarding our setup effects like the anti-confinement of the blue detuned 2D-lattice or a magnetic field gradient in the plane of the atoms could also affect the precise shape of the density profile. Yet, to get a first impression of how Friedel oscillations could look like in our setup, I neglect these experimental difficulties in a first step and assume that we can create a perfectly flat potential in each tube. In Section 3.4 I will incorporate the confining effect of a red lattice and present a method to recover a homogeneous potential. Starting from the 2D homogeneous Fermi gas in the ring trap it is clear that the tubes generated by a lattice will be of different size. I will concentrate on the central tubes with roughly the same lengths because the density in shorter tubes is more sensitive to fluctuations of the particle number. Consider a tube of the length $L = 120\,\mu\text{m}$, which corresponds to a possible diameter of the ring D_0. It is reasonable to model the walls limiting the

tube from the left and from the right with two gaussian functions,

$$V_{ring}(x) = V_0 \left[\exp\left(-\frac{2(x-R_0)^2}{s^2} \right) + \exp\left(-\frac{2(x+R_0)^2}{s^2} \right) \right]. \tag{3.51}$$

V_0 defines the height of the walls and s determines their width. $R_0 = 60\,\mu\text{m}$ is the radius of the ring trap and therefore half the length of the tube. From images we estimate the width of the ring beam to be $s \simeq 5\,\mu\text{m}$. In the experiment the walls surrounding the tubes are of course of finite width. However, a short estimate shows that tunneling out of the tubes is suppressed to a negligible rate and hence we can restrict the test system to the finite size of $120\,\mu\text{m}$ between the maxima of the left and the right wall. For a laser power of $P_0 = 200\,\text{mW}$ one finds a tunneling rate through a wall for a plane wave at Fermi energy to be

$$T = \exp\left(i \int_{x_1}^{x_2} dx \sqrt{\frac{2m(E_f - V(x))}{\hbar^2}} \right) = \exp(-125.8) \simeq 0. \tag{3.52}$$

In this calculation x_1 and x_2 were chosen to be the borders of the interval I on which $E_f < V(x)$ because this is the region where the wave function gets heavily suppressed in amplitude. The Fermi energy of $E_f = \hbar^2 k_f^2/2m = \hbar^2 (n_{1D}\pi)^2/2m = 518\,\text{Hz}$ follows from the assumed 1D density $n_{1D} = 1/4\,\mu\text{m}^{-1}$. [9]

The potential barrier $V_{barrier}$ that shall be imprinted at the center of the tubes is modeled by a gaussian potential barrier:

$$V_{barrier}(x) = A \exp\left(-\frac{2x^2}{\sigma^2} \right). \tag{3.53}$$

A describes the amplitude of the barrier and its width is given by σ. I estimated that we are able to create barriers with an amplitude of $A \simeq 5\,\text{kHz}$ and a width of $\sigma \simeq 2\,\mu\text{m}$.[10] These numbers shall only serve as an orientation. By adjusting the laser power and the pixel pattern on the DMD we can tune the shape of the barrier. For convenience I will call the potential in the center of the tube *barrier* and the potentials closing the tube from the left and the right will be referred to as *walls* in

[9] equation (3.52) was solved in a numerical calculation where the potential of the ring was calculated for the whole 2D plane of the atoms.

[10] These numbers come from a simulation where the DMD is modeled to be illuminated by a gaussian beam with a power of 0.1 W and a waist of 75 µm in the plane of the atoms. The barrier is created by a line with a width of 10 DMD pixels. The image of the DMD is smoothed with a gaussian filter with a waist of 1 µm to incorporate the finite resolution of the DMD optics.

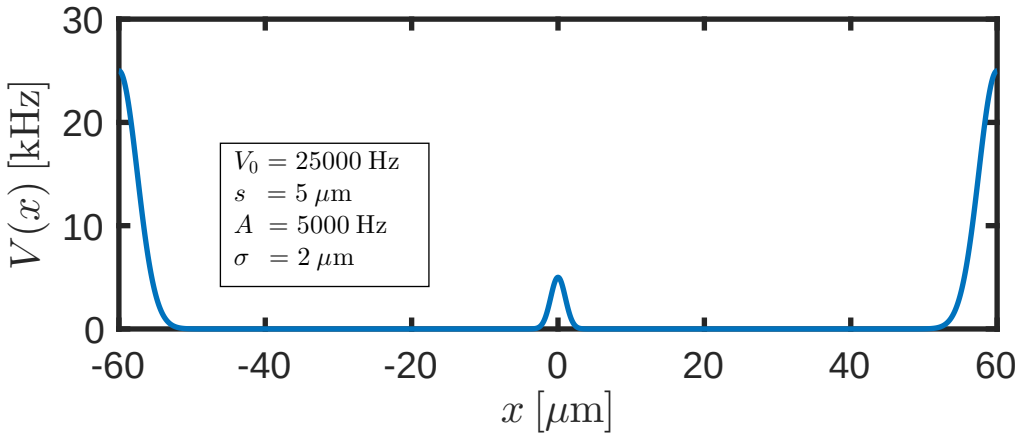

Figure 3.4: One-dimensional test potential $V_{ring} + V_{barrier}$ for the parameter listed in the box.

the following. The sum of the two potential V_{ring} and $V_{barrier}$ constitutes the test potential shown in Figure 3.4 which was used for the simulation:

$$V(x) = V_0 \left[\exp\left(-\frac{2(x - R_0)^2}{s^2} \right) + \exp\left(-\frac{2(x + R_0)^2}{s^2} \right) \right] + A \exp\left(-\frac{2x^2}{\sigma^2} \right). \quad (3.54)$$

This test potential provides smoothness and flatness that can certainly not be achieved in the experiment. Nevertheless it can be explored to gain some principle understanding of how its precise form influences the Friedel oscillations. The results of the simulation based on this test potential are presented in the following section.

3.3 Results

What has been achieved so far is a method to numerically calculate the density distribution of a (thermal) non-interacting many-body fermionic system in a one-dimensional test potential. First the one-particle orbitals and their corresponding energies are obtained from solving the discretized Schroedinger equation by the diagonalization of the corresponding Hamilton matrix. The chemical potential is set to $\mu = \epsilon_N$ defining the Fermi distribution function together with the temperature T. Finally the density can be found by executing the sum in either equation (3.13) or equation (3.14). I realized this simulation in Matlab and varied the system parameters to study their impact on the Friedel oscillations. In this section the results of theses calculations shall be discussed in detail. For reasonable parameters and zero temperature we can report Friedel oscillations with amplitudes of $\Theta_1 = 32\,\%$

parameter	variable
steepness of the walls	s
height of the walls	V_0
amplitude of the barrier	A
width of the barrier	σ
number of particles	N
temperature	T

Table 3.1: Tunable parameters in the study of Friedel oscillations in a flat box. For $T \neq 0$ the average number of particles almost equals N.

and $\Theta_2 = 15\,\%$ for the first and the oscillation, respectively. At a temperature of $T/T_f = 0.1$ the amplitudes reduce to $\Theta_1 = 28\,\%$ and $\Theta_2 = 9\,\%$. The central finding from the evaluation of this chapter is that the more abrupt and the more pronounced the change in the potential, the larger will be the amplitudes of the Friedel oscillations. However, under realistic assumption the simulation predicts that the second oscillation will not stand out from the noise.

3.3.1 Friedel oscillations in a 1D test potential at zero temperature

In order to get an insight into the characteristics of Friedel oscillation, as a first step the simulation was performed using the test potential defined in equation (3.54). The system is determined by various tunable parameters which are shown in table 3.1. The simplest case is to assume zero temperature $T = 0$. Figure 3.5 shows the density distribution for this case with $N = 25$ atoms. Friedel oscillations at the central barrier and at the walls of the 1D system are clearly visible. As mentioned previously, in our experimental setup all tubes will be of different length and thus the density modulations at the walls in different tubes will be displaced along the x-axis with respect to each other, such that averaging over many tubes will cancel their signal. Hence, we concentrate on the oscillations at the central barrier, because their position on the x-axis is the same for all tubes and an average over the y-dimension can be carried out. The Friedel wavelength of these oscillations is found to be $\lambda_{FO} = 4\,\mu\text{m}$, as expected. The relative amplitude of the first oscillation is $\Theta_1 = 32\,\%$ with respect to an average density of $\overline{n}_{1D} \simeq 0.25\,\mu\text{m}^{-1}$ as shown in Figure 3.6. For the second oscillation the amplitude has dropped down to $\Theta_2 = 15\,\%$. The average density is

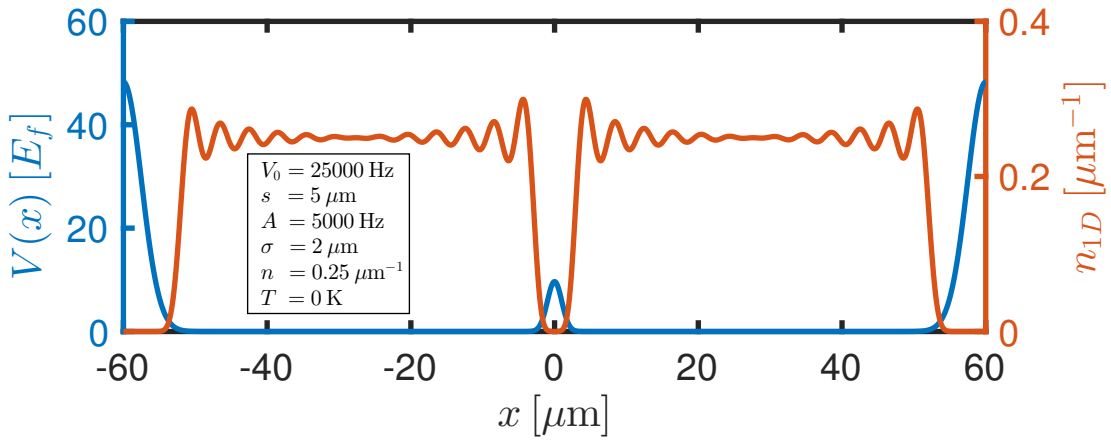

Figure 3.5: Resulting density distribution for 25 fermions in the test potential, yielding a Friedel wavelength of $\lambda_{FO} = 4\,\mu\mathrm{m}$ and relative amplitudes of $\Theta_1 = 32\,\%$ and $\Theta_2 = 15\,\%$ for the first and second oscillation respectively.

defined as

$$\overline{n}_{1D} = \frac{N}{\Omega}; \qquad \Omega = \{x | V(x) < E_f\}, \tag{3.55}$$

since Ω approximately constitutes the area where the particles are located. In order to examine the influence of the potential on the form of the Friedel oscillations, we kept the temperature $T = 0\,\mathrm{K}$ as well as the particle number $N = 25$ constant and varied all the parameters defining the potential. For each point in the parameter space the Friedel wavelength λ_{FO} and the amplitudes of the first two oscillations have been analyzed according to the way shown in Figure 3.6. All results refer to the Friedel oscillations that appear at the central barrier for the reason given above. We found the parameters of the walls V_0 and s to be basically of no relevance, as long as they do not significantly influence the local density in the vicinity of the barrier. Given that the tubes are long compared to the width of the walls, this condition can easily be fulfilled in the experiment. Hence, the discussion focuses on the parameters A and σ. Figure (3.7) displays the behavior of the first two amplitudes and the wavelength of the Friedel oscillations within the parameter space spanned by σ and A. For these calculations the wall parameters were set to $V_0 = 25\,\mathrm{kHz}$ and $s = 5\,\mu\mathrm{m}$. The Friedel wavelength remains almost constant with changing the barrier height, whereas it is affected in an apparent linear fashion by a variation of σ. This behavior can be attributed to the change in the average density provoked by the broadening of the barrier. The area Ω which defines roughly the spatial extend of all occupied one-particle orbitals can be shown to decrease approximately linearly with an increase

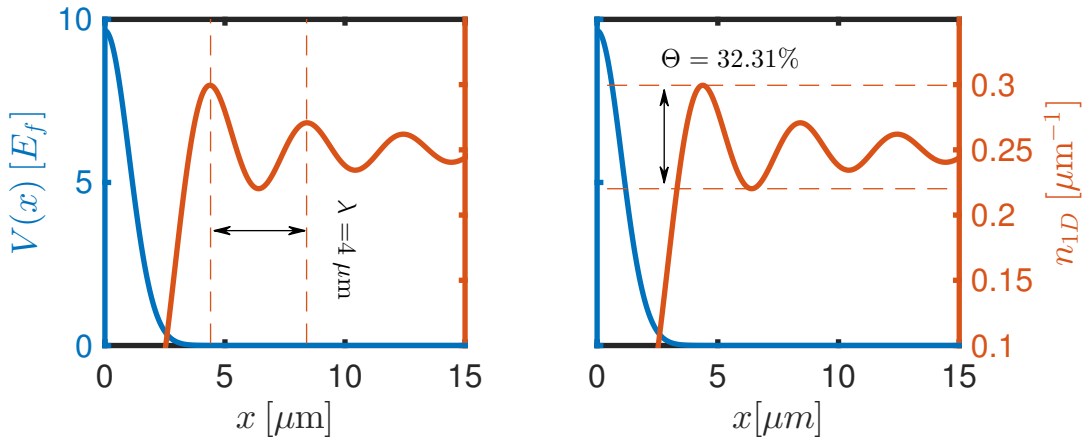

Figure 3.6: A zoom to the vicinity of the central barrier, where Friedel oscillations are located. The red dashed lines mark the beginning and the end of the first oscillation in the left plot and its amplitude in the right plot.

of σ. For the average density this implies a $-1/\sigma$ dependence which results in the relation

$$\lambda_{FO} \propto -\sigma. \tag{3.56}$$

The same effect exists as well for the height of the barrier, but it is much less pronounced.

The amplitudes are significantly affected by the two parameters. The results reach from $[\Theta_1 = 34\,\%, \Theta_2 = 15\,\%]$ for $\sigma = 1\mu m$ and $A = 6000Hz$ to the absence of significant Friedel oscillations for $A \lesssim 800\,\mathrm{Hz}$ and $\sigma \gtrsim 3\,\mu\mathrm{m}$. This can be explained by the fact that the lower and the broader the barrier the more displaced are the points p_i where $V(p_i) = \epsilon_i$ with respect to each other. These points roughly define where the one-particle orbital $\phi_i(x)$ *begins* since $|\phi_i(x)|$ is close to zero for $V(x) > \epsilon_i$. If the starting points of the one-particle orbitals are displaced with respect to each other, their oscillations are out of phase and therefore rather destructive than constructive interference occurs and the amplitude of the Friedel oscillation are small. If the barrier was infinitely steep, all orbitals would have the same starting point and therefore their oscillations would be in phase in the vicinity of the barrier and thus, they would constructively interfere resulting in very distinct Friedel oscillations. It can be stated that the more abrupt and the more pronounced the change in the potential, the more distinct Friedel oscillations are. The most relevant feature of the barrier is the distance on which the potential drops from a value $V \gtrsim E_f$ to $V \simeq 0$, because the starting points of all orbitals lie within this area. By enhancing the barrier height

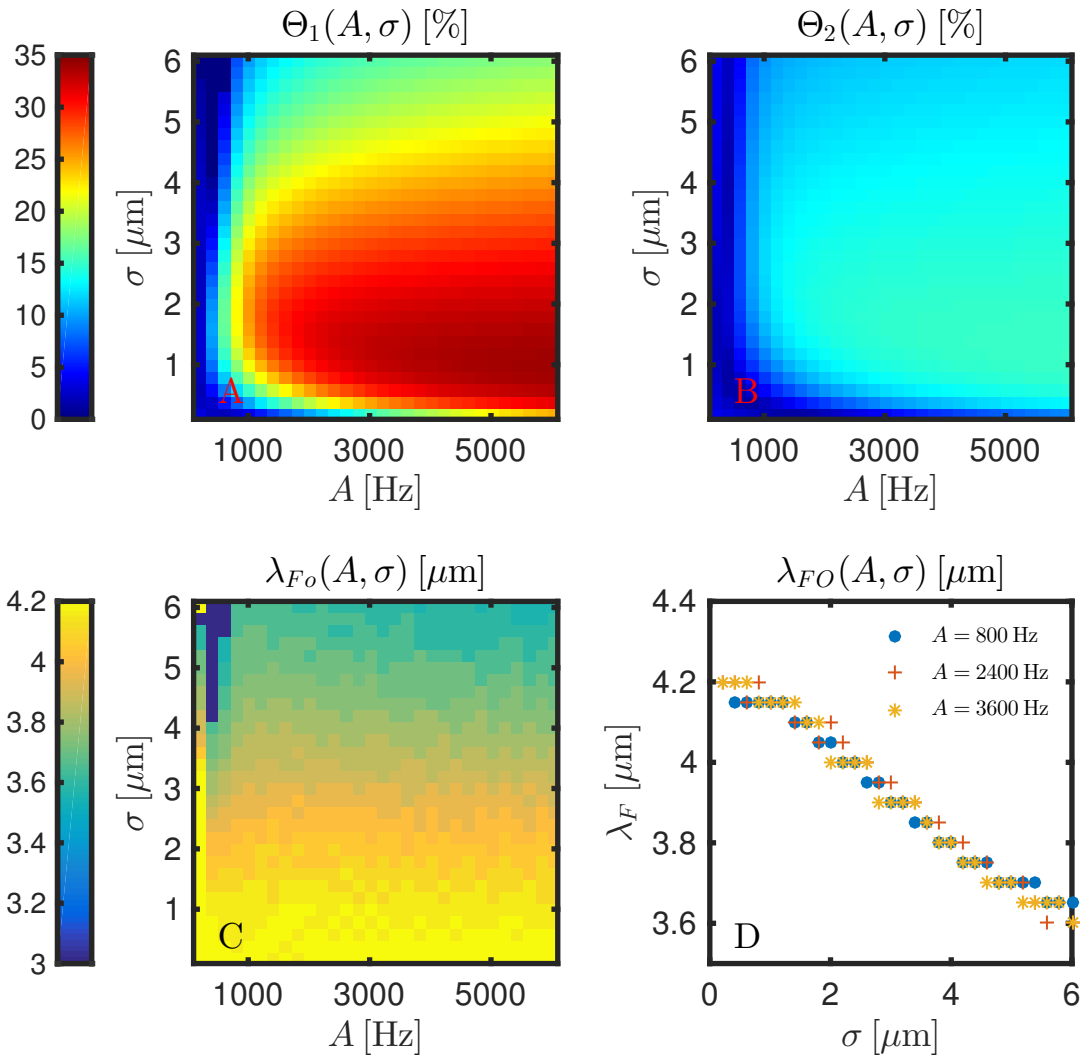

Figure 3.7: Friedel oscillations emerge from a central Barrier in a one-dimensional test potential. A) and B) show the dependence of the relative amplitudes of the first and second oscillation Θ_1 and Θ_2 on the parameters A and σ defining the height and the width of the barrier, respectively. The larger σ and the smaller A the smaller the amplitudes of the oscillation, except for $\sigma < 1$. C) displays the Friedel wavelength plotted against the same parameters. Wheres λ_{FO} is robust against a change of A it is inversely proportional to σ. For $A \lesssim 800\,\text{Hz}$ and $\sigma \gtrsim 3\,\mu\text{m}$ there are points for which the oscillation was too weak to be detected by the evaluation code resulting in $\lambda_{FO} = 0\,\mu\text{m}$. D) shows profiles of λ_{FO} along three different vertical sections through plot C) that confirm the described behavior. The other system parameters have been set to $V_0 = 25\,\text{kHz}$ and $s = 5\,\mu\text{m}$ for these calculations.

parameter	variable	value
steepness of the walls	s	$5\,\mu m$
height of the walls	V_0	$25\,kHz$
amplitude of the barrier	A	$5\,kHz$
width of the barrier	σ	$2\,\mu m$
number of particles	N	25

Table 3.2: System parameters chosen for further investigations at finite temperature.

we reduce this distance and effectively steepen the barrier. As already mentioned the effect on the average density is small, thus a maximal height of the barrier is desirable.

3.3.2 Friedel oscillations in a 1D test potential at finite temperature

From the study at zero temperature first quantitative results for the Friedel oscillations have been achieved. Now the finite temperature shall be incorporated. Since the whole procedure from the zero temperature study shall not be repeated here, I restricted the investigation of the influence of the temperature to the parameters listed in table 3.2 since they fulfill two criteria:

1. The simulation provides promising results for these values at $T = 0\,K$, namely $\lambda_{FO} = 4\,\mu m$ and $\Theta_1 = 32\,\%$ and $\Theta_2 = 15\,\%$. Recalling the signal to noise ratio of 12 for $\overline{n}_{1D} \simeq 0.25\,\mu m^{-2}$ for a 1000 image average one finds Θ_2 to be twice the amplitude of the noise which is $8\,\%$. It is reasonable to expect that the second oscillation could be detected.

2. Estimations confirm that we can realize a 1D potential in the experiment that corresponds to these parameters.

A finite temperature implies a loss of coherence. The less coherent the system is, the less pronounced its quantum features are and accordingly one would expect Friedel oscillations to be less visible at higher temperatures. Let me recall the example of the box with infinitely high walls from Section 3.1, whose eigenfunctions are characterized by single individual momenta. At $T = 0$ the occupation of momenta is given by a Heaviside function, but for any finite temperature the sharp edge at the Fermi energy washes out and higher momenta enter the system. It seems reasonable that

this causes the spatial frequency given by k_f to be less pronounced, i.e. one would expect smaller amplitudes for Friedel oscillations. For low temperatures the Friedel wavelength should not be altered significantly since the occupation of higher momenta is weak and k_f remains to be the characteristic length scale in the system. As our test potential provides high similarity to the infinite potential box we expect the given arguments to hold for our case as well. The temperature is measured in units of the Fermi temperature $T_f = E_f/k_B$. Indeed, the results of the simulation confirm these considerations. Figure 3.8 displays how the amplitudes of the Friedel oscillations decrease with increasing temperature. It can be reported that even for low temperatures the oscillations vanish completely for far enough distances from the barrier. However, the Friedel wavelength of $\lambda_{FO} = 4\,\mu\text{m}$ remains almost unchanged. At a temperature of $T/T_f = 0.1$ the simulation yields amplitudes of $\Theta_1 = 28\,\%$ and $\Theta_2 = 9\,\%$. For $T > 0.11\ T_f$ we find the second amplitude to be smaller than the noise floor of $8\,\%$ corresponding to a signal to noise ratio of 12 that was introduced in Section 3.1. Even for more favorable barrier parameters, namely $A = 10\,\text{kHz}$ and $\sigma = 2\,\mu\text{m}$ Θ_2 is still only $9\,\%$ for $T/T_f = 0.1$. Apparently, we cannot compensate for high temperature by optimizing the barrier, hence the temperature depicts a crucial parameter for the experiment. From these numbers we can conclude that temperatures below $0.1\ T_f$ are mandatory for the observation of Friedel oscillations. However, at present we do not have a quantitative measure on the temperature but it is highly questionable whether we can create sample significantly cooler than $T/T_f = 0.1$.

3.4 1D Friedel oscillations in homogeneous potentials generated with the makeflat-algorithm

Analyzing the many-body density distribution in a smooth and homogeneous 1D test potential revealed Friedel oscillations emerging from a central barrier. Even at low temperatures of $T/T_f < 0.1$ the second oscillation tends to be obscured by noise. However, nor the fact that the experimental setup proposed in Section 3.1 creates a confinement along the 1D tubes has been considered, neither the possibility to average the density distribution along the y-axis, i.e. to average over the tubes, has been taken into account. In this section I will show that such a confinement makes an observation of Friedel oscillations impossible and therefore present method based

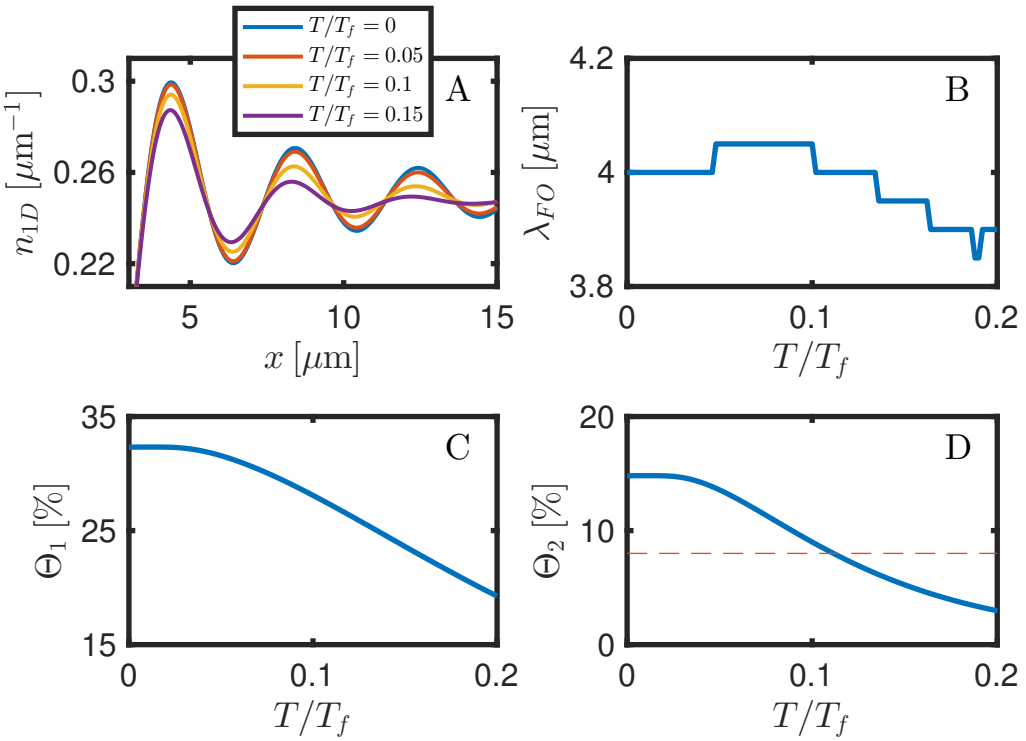

Figure 3.8: A) Friedel oscillations at the vicinity of a barrier in a one-dimensional homogeneous potential for different temperatures. B) The wavelength of the Friedel oscillations in dependence on the temperature. C) Amplitude of the first oscillation in dependence on the temperature. D) Amplitude of the second oscillation in dependence on the temperature. The red dashed line indicates the noise level. Whereas λ_{FO} is not affected significantly by the temperature in the displayed range, the amplitudes of the Friedel oscillations strongly decrease with an increase of the the temperature. This makes low temperatures necessary for the second oscillation to stand out from noise.

on the DMD to recover a homogeneous potential, that is called makeflat-algorithm. Also, the creation of the barrier by means of the DMD is modeled realistically. Within a simulation I was able to compensate the confinement of an optical lattice and to imprint a barrier of sufficient height and steepness to induce Friedel oscillations of almost the same strength as in the test potential, showing that it is in general possible to design a suitable potential for our intent.

As mentioned previously, we are planning to realize the 1D tubes via a red detuned lattice. The simulation with the test potential defined by the parameters listed in table 3.2 yielded a Fermi energy of $E_f = 518\,\mathrm{Hz}$. Since this determines the shortest time scale on which the system evolves, it is mandatory that the tunneling rate J of the lattice is even smaller to ensure that tunneling events between the tubes play a minor role in the dynamics of the system. Additionally one has to guarantee that

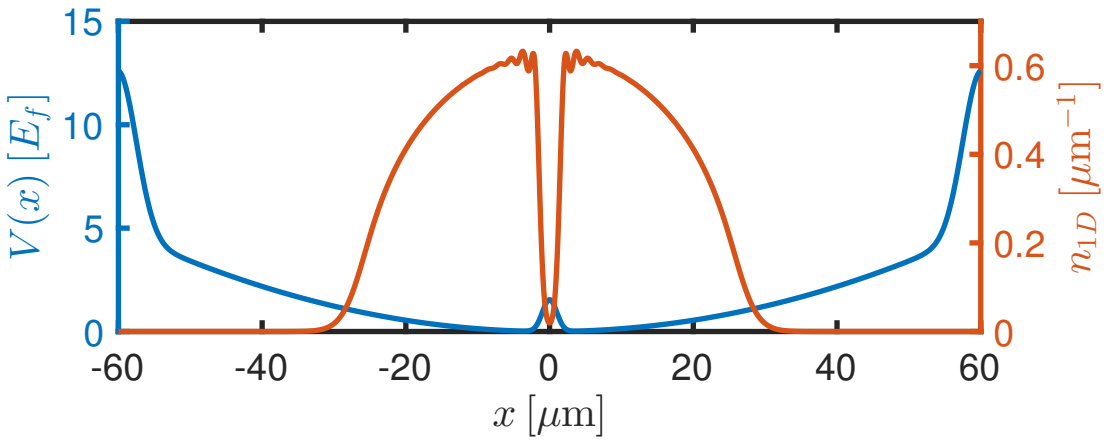

Figure 3.9: Density distribution in the test potential with parameters listed in table 3.2 and an additional confinement of 122 Hz. The wavelength of the resulting Friedel oscillations is clearly below our resolution.

in each lattice well only the ground state is occupied along the confined direction in order to truly reduce the dynamics to one dimension. This is achieved as soon as the spacing between ground state and first excited state of the lattice well exceeds the Fermi energy in x-direction significantly. Thus, regarding the lattice we can formulate two conditions:

$$J < E_f \qquad \text{and} \qquad \hbar\omega_{lattice} > E_f \tag{3.57}$$

For a retro-reflected gaussian beam with characterized by the waists $w_x = 370\,\mu\mathrm{m}$ and $w_z = 10\,\mu\mathrm{m}$ and a wavelength of $\lambda = 1064\,\mathrm{nm}$ we find the above condition to be fulfilled for a laser power of $P_{squeeze} \gtrsim 350\,\mathrm{mW}$ giving rise to a harmonic confinement along the tube of $\omega_{tube} = 122\,\mathrm{Hz}$. The parameters coincide with the parameters of the squeeze beam. Figure 3.9 shows how such a confinement leads to an accumulation of the atoms in the center of the tube such that the wavelength as well as the amplitudes of the oscillations become far too small for an observation. Obviously the approach of slicing the gas into tubes with a red lattice is not applicable without further effort. We hope that we can recover a homogeneous potential by the means of our DMD. The idea is to increase potential energy with the blue detuned DMD beam until the bottom of the potential is flat again. By activating pixels on the DMD we can locally add potential energy in the plane of the atoms. In order to find an appropriate pattern for the DMD pixels the makeflat-algorithm was developed. It is supposed to work similar to a controll-loop. A recorded atomic density distribution serves as an error signal. Regions with above-average density are regions of low potential

energy and vice versa. Hence, for the next experimental cycle corresponding pixels are turned on or off respectively resulting in a new potential. The next recorded density distribution provides a new error signal, the DMD pixels are adjusted and so on and so forth. To achieve a meaningful error signal an average over several density images has to be taken before the density distribution can be processed. To really flatten the potential at any point x a specific amount of potential energy has to be added.

How can one smoothly control the intensity of the DMD beam at the position of the atoms, when an individual pixel can only be turned on or off? The key point is, that because of the finite resolution of the DMD imaging, the laser intensity $I(x)$ at a certain position in the plane of the atoms is not determined by a single pixel, but by several pixels of the DMD whose precise number depends on the width of the point spread function. The point spread function describes how the image of an idealized point source is broadened due to diffraction and aberrations of the imaging system. If only diffraction is taken into account the point spread function has the form of a Bessel function and the distance from its central maximum to the first zero-crossing defines the resolution [56]. For a resolution $R \simeq 1\,\mu\text{m}$ the number of contributing pixels is at least 25 since the effective pixel size, i.e. the physical pixel size of the DMD divided by the magnification of the imaging system, is approximately $0.2 \times 0.2\,\mu\text{m}^2$ in our setup. By activating only a certain fraction of them the power can be controlled in approximately 25 steps. In order to simulate the process of flattening the tubes we wrote a model based on the makeflat-algorithm. The Figure 3.10 visualizes the functioning of the model that shall be explained in the following.

To understand the model it is convenient to distinguish three different planes, namely the DMD plane, the camera plane and the plane of the atoms. The plane of the atoms is the plane where the atoms are trapped and where the precise form of the potential is of importance. This plane is modeled by a grid with a size of $218 \times 218\,\mu\text{m}^2$ and a grid point spacing of $\Delta = 0.05\,\mu\text{m}$. The potentials delivered by the three involved laser beams, V_{ring}, $V_{squeeze}$ and V_{DMD}, are calculated for this plane with respect to their beam parameters. The DMD beam has a waist of $w_x = w_y = 75\,\mu\text{m}$ and the ring beam is modeled by the radial symmetric intensity distribution $I(r, \phi) \propto \exp(-2[r - R_0]^2/s^2)$ where $R_0 = 60\,\mu\text{m}$ defines the ring radius and $s = 5\,\mu\text{m}$ the width of the ring wall. The intensity distribution in a retro reflected beam equals four times the intensity of the forward propagating beam modulated with $\cos^2(ky)$ for y being the propagation direction. The lattice characteristics of the beam was

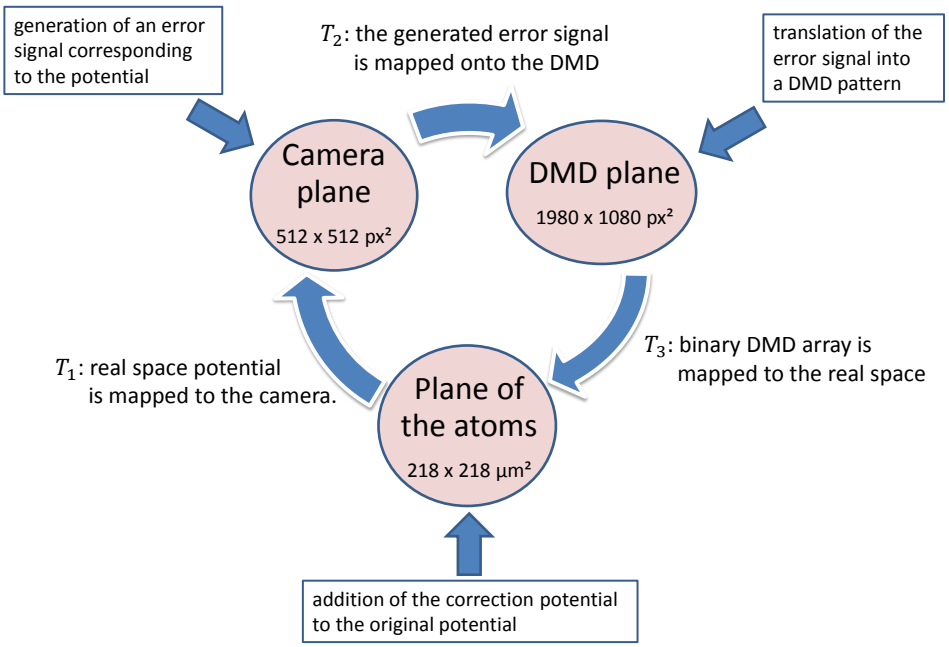

Figure 3.10: Schematic representation of the functioning of the model used to simulate a flattening of a potential by means of the makeflat-algorith.

unimportant for the test of the makeflat-algorithm, hence we ignored the periodic modulation in the calculation of the squeeze potential. The waists of the squeeze beam are $w_x = 370\,\mu\text{m}$ and $w_y = 10\,\mu\text{m}$. The powers were set to $P_{squeeze} = 350\,\text{mW}$, $P_{DMD} = 70\,\text{mW}$ and $P_{ring} = 100\,\text{mW}$. The combined potential of the ring beam and the squeeze beam is the starting point for the model. The imaging process in the experiment is replaced in this simulation by simply applying a transformation matrix T_1 to the plane of the atoms that maps the potential onto the camera plane which is represented by a $512\,\text{px} \times 512\,\text{px}$ array. To incorporate the finite resolution of the imaging microscope we apply a gaussian filter with a waist of $\sigma_{camera} = 1\,\mu\text{m}$ to the image in the camera plane. This filtered image of the potential is translated into an error signal. Hence, in this simulation the error signal is not based on an atomic density but on the potential itself. A second transformation matrix T_2 maps this error signal to the DMD plane that is given by a $1920\,\text{px} \times 1080\,\text{px}$ array. Corresponding to the error signal DMD pixels are activated or deactivated until finally a binary array of DMD pixels is mapped back onto the plane of the atoms by a third transformation matrix T_3. The DMD image is subsequently multiplied with the potential that was calculated for the DMD beam in the plane of the atoms resulting in a correction

potential. Again, in order to respect the finite resolution of the DMD imaging, a gaussian filter is applied to the correction potential whose waist σ_{DMD} was varied for different runs of the program. The filtered correction potential is added to the original potential resulting in a new potential which is then closer to homogeneity. This new potential is the starting point for the next iteration. Figure 3.11 shows the starting potential, the DMD potential that is used for the correction and the resulting potential.

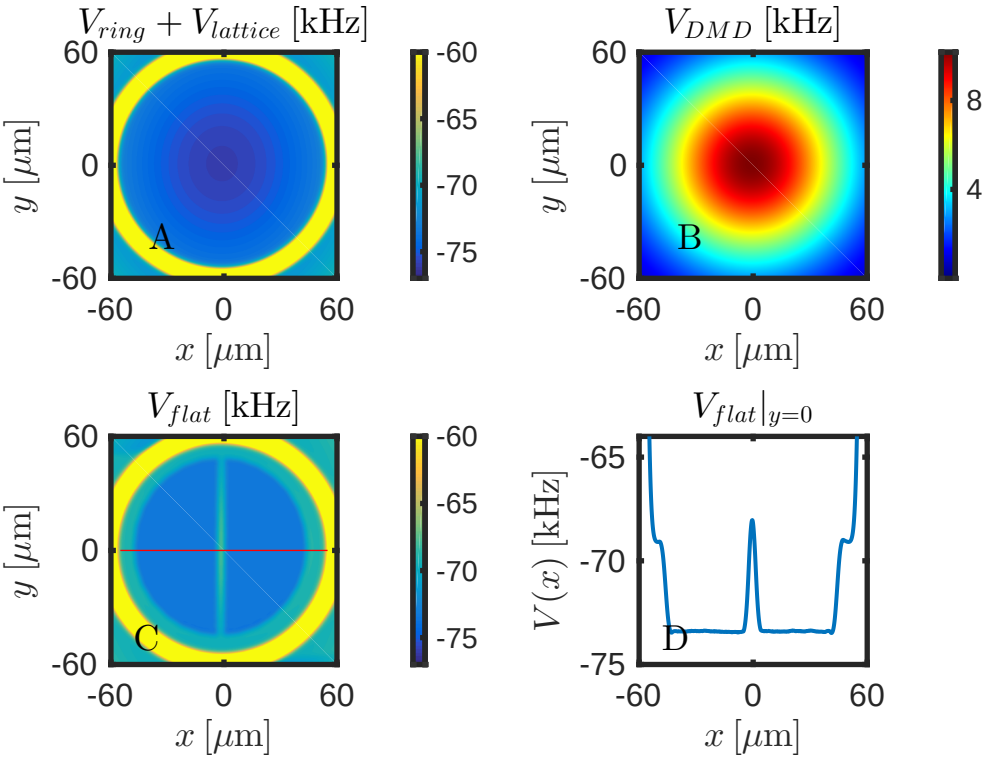

Figure 3.11: A) The combined potential provided by the squeeze beam and the ring beam in the plane of the atoms. The color scale does not cover the whole range of the potential. B) Potential provided by the DMD beam in the plane of the atoms. C) Resulting potential from the flattening process with $\sigma_{DMD} = 3\,\mu$m. D) Profile of the potential in C) along a horizontal section at $y = 0$ (red line in C).

In the following the generation and the processing of the error signal shall be explained a bit more detailed. Of course the starting potential $V_{ring} + V_{squeeze}$ is not supposed to be flattened in the whole plane of the atoms, but only on a circular area Π inside the ring. In the first iteration the algorithm defines a normalization constant

$$C = \max\{\,|V_{i,j} - \overline{V}_{\Pi}|\,\}|i,j \in \Pi \tag{3.58}$$

for the error signal, where $\overline{V}_\Pi$ denotes the average of V on the area Π.[11] Afterwards the program calculates an error signal on each camera pixel within Π:

$$error_{i,j} = \frac{V_{i,j} - \overline{V}_\Pi}{C}, \tag{3.59}$$

allowing for positive and negative values. This error matrix is weighted with the inverse potential delivered by the DMD beam in the plane of the atoms to ensure a constant gain over the whole region of interest. Subsequently the error matrix is mapped onto the DMD plane and multiplied with a gain factor $G \leq 1$ such that all its values lie within the range $[-G; G]$. In a randomized process pixels of the DMD are turned on or off, where the probability of a pixel to be turned on or off is simply given by its absolute error value. A positive sign indicates that a pixel shall be turned on whereas a negative sign leads to turning it off, where of course only a pixel that was off before can be turned on and vice versa. This process results in the binary DMD array that is processed as described above. The program memorizes the DMD array until in the next iteration step it will be modified by activating and deactivating pixels with respect to the new error signal. The maximum deviation of $V_{i,j}|i,j \in \Pi$ from its mean value is assumed to decrease for each iteration resulting in a damping of the response of the DMD due to the normalization by C, i.e. the number of pixels whose status changes in one iteration is supposed to decrease from iteration to iteration. Otherwise the DMD array would not converge and the potential would not become homogeneous.

Even within the framework of this simulation, where perfect beam profiles are available, it was challenging to really flatten the potential. On the attempt to suppress the fluctuations of the potential to $\delta V \lesssim 0.1 E_f$ we encountered various difficulties. If the area Π was chosen too large it included parts of the ring potential which implied a huge normalization constant C. As a result the error signal was too small in the center to appropriately flatten the potential. Furthermore, the power of the DMD beam was crucial for the quality of the resulting potential. If the power of the DMD beam is too high, active pixels can cause local deviations in the potential on the order of magnitude of the Fermi energy, meanwhile if it is too low it cannot compensate the squeeze potential especially at larger distances from the center of the beam. An adequate power of the DMD was found to be $P_{DMD} = 70\,\mathrm{mW}$. Next, I had to reduce

[11] Since the plane is discretized we use the indices i, j to address a certain grid point replacing the continuous variables (x, y).

the gain factor to $G = 0.2$ to prevent the DMD array from swinging. Swinging in this case means an alternating on- and off-switching of a great number of pixels in each iteration. In this case the error signal does not decrease and the the DMD pattern does not converge. Finally, it turned out that the final potential heavily depends on the width of the gaussian filter that smooths the correction potential. In the experiment one should try to improve the homogeneity of the resulting potential by defocusing the DMD image. As already mentioned the number of DMD pixels contributing to the intensity at one point in the plane of the atoms increases for a broader point spread function resulting in a smoother correction potential and respectively a smoother final potential. The applicability of the makeflat-algorithm remains to be tested in the experiment when the signal is not the potential itself any longer, but rather the atomic density with noise on it. It is certainly recommendable to use atomic clouds of high density as a signal for the algorithm in order to achieve a high signal to noise ratio.

In Figure 3.12 the resulting potential along a single tube, i.e. a section in x-direction at $y = 0$ through the potential in the plane of the atoms, is shown together with the resulting density distribution for $T/T_f = 0.1$. Each plot corresponds to a different waist σ_{DMD} for the filter. Obviously the potential corresponding to $\sigma_{Filter} = 1\,\mu\text{m}$ exhibits strong fluctuations up to half of the Fermi energy. The profile of the potential significantly influences the profile of the density distribution in a reverse proportional manner. Thus, the density wildly fluctuates and Friedel oscillations are not visible. For $\sigma_{Filter} = 3\,\mu\text{m}$ the fluctuation of the potential has significantly decreased in magnitude. Accordingly the density profile looks smoother as well and on a first sight the oscillations close to the barrier and close to the walls look familiar to the Friedel oscillations that emerged in the test potential in the previous sections. The Friedel oscillations close to the potential barrier stand out from the fluctuations of the density caused by the fluctuations of the potential. This is a necessary requirement for their observation. Further increase of σ_{DMD} leads to further improvement of the homogeneity. However, the Friedel oscillations decrease in amplitude because the potential barrier is more smeared out. The results for $\sigma_{DMD} = 3\,\mu\text{m}$ and $\sigma_{DMD} = 5\,\mu\text{m}$ are the most promising.

The resulting 1D tubes after the flattening process all differ from one another not only in their length but also in the way how they deviate from the perfect form. Respectively, also the density profiles exhibit individual fluctuations but in an average over several tubes the fluctuations in the potential cancel (not shown) and so do the

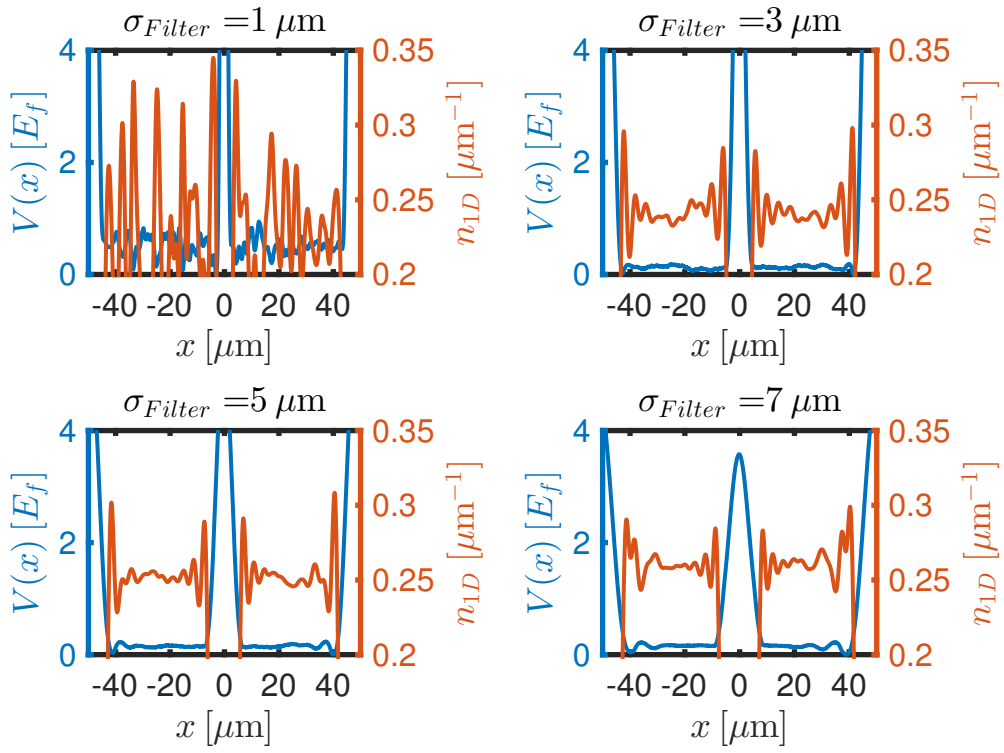

Figure 3.12: Flattened potentials and the corresponding density distribution. The filter used for the imitation of the point spread function of the DMD imaging is varied between the four images.

fluctuations in the density (see Figure 3.13). Taking the average over the density distributions of the 101 central tubes essentially cancels most of the density fluctuations provoked by fluctuations of the potential and a clear signal of Friedel oscillations is left (see Figure 3.13). Only for the case $\sigma_{Filter} = 1\,\mu$m we cannot report any meaningful result. Obviously the imperfections of the potential are too distinct to allow for the occurrence of visible Friedel oscillations. $\sigma_{Filter} = 3\,\mu$m provides the best results in the simulation. The first oscillation is well pronounced with an amplitude of $\Theta_1 = 29\,\%$, but the second oscillation $\Theta_2 = 7\,\%$ is smaller than the noise level of $8\,\%$ quantified in Section 3.1. For larger σ_{Filter} we still find clear Friedel oscillations but with smaller amplitudes due to the broadened barrier. These numbers are in agreement with the results we found for the test potential, where the simulation yielded an amplitude of $\Theta_2 = 9\,\%$ for $T/T_f = 0.1$.

I conclude that the procedure of flattening the potential leads to Friedel oscillations of almost the same quality as reported for the test potential. Of course this procedure still has to be established experimentally, but at least the simulation suggests that

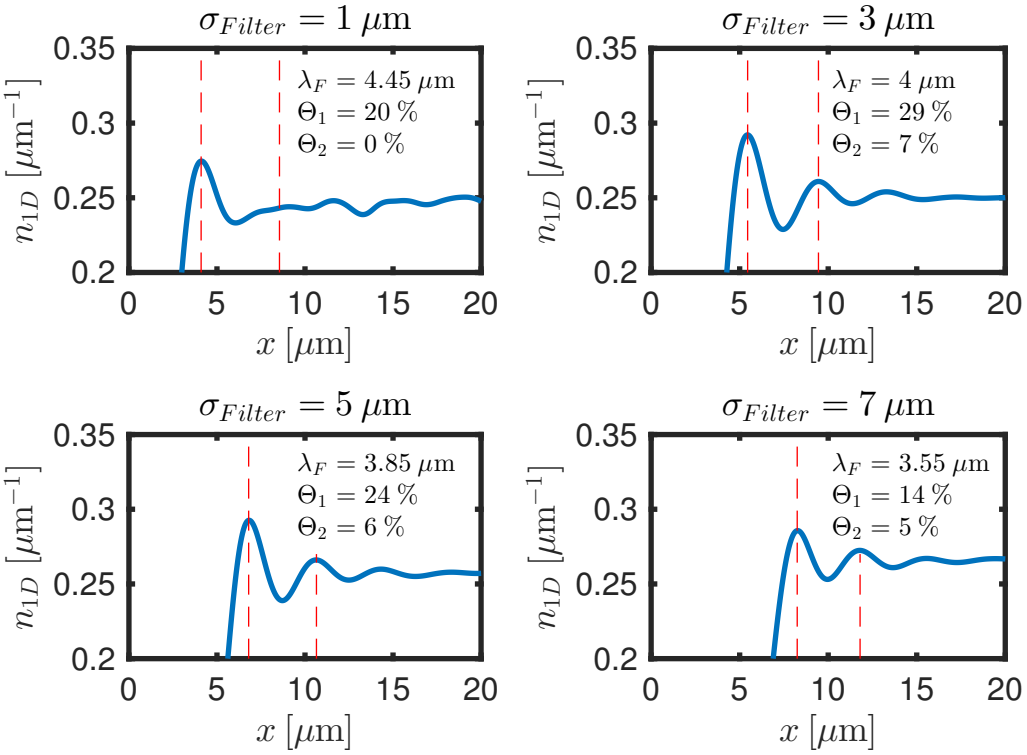

Figure 3.13: Averaged density distribution in the flattened potential. The average was performed over the density distributions of 101 one dimensional potentials given by parallel slices along the x direction with a distance of 0.5 µm. The slices were taken symmetrically around $y = 0$. The four images correspond to four different filters used to imitate the point spread function of the DMD imaging.

creating a suitable potential for the observation of Friedel oscillation is in general possible. It was observed how distinct imperfections in the potential drastically alter the particle density distribution, leading to the demand $\delta V << E_f$. The makeflat-algorithm was tested successfully with idealized input data and it turned out that the power of the DMD beam, the sharpness of the DMD imaging and the gain of the algorithm are crucial for its performance. In the average over the tubes the reduction of noise originating from the imaging process was not incorporated so far. The considerations only confirmed, that fluctuations of the potential can be eliminated in such an average. It will now depend on a detailed analysis of the signal to noise ratio whether or not the observation of Friedel oscillations in our experiment seems feasible.

3.5 Signal to noise ratio

The most realistic simulation of Friedel oscillations revealed a Friedel wavelength of $\lambda_{FO} = 4\,\mu\text{m}$ and relative amplitudes of $\Theta_1 = 29\,\%$ and $\Theta_2 = 7\,\%$ for the first and the second oscillation respectively. For these calculations the density and the temperature were set to $n_{1D} \simeq 0.25\,\mu\text{m}^{-1}$ corresponding to $n_{2D} \simeq 0.5\,\mu\text{m}^{-2}$ and $T/T_f = 0.1$. I recall, that the estimate from Section 3.1 yielded a signal to noise ratio of $SNR \simeq 12$ for an average over 1000 images. Even then the second oscillation would be obscured by noise, as the noise level after averaging remains to be about 8% of the signal.

In this section the signal to noise ratio is treated in more detail and I include technical noise as well as the quantum efficiency of the camera. Also, higher imaging intensities will be regarded that require a modification of the Beers law to account for saturation effects. The goal of these considerations is to determine a realistic estimate on the number of images that have to be averaged in order to make the second amplitude visible. As already mentioned, we rely on the detection of at least two oscillations to attribute the modulation of the density to the mechanism of Friedel oscillations, since close to the potential barrier also other effects can cause an apparent density modulation. For example, diffraction of the imaging light from sharp edges in the optical density can occur. I expect the second oscillation to be visible when its amplitude is at least twice the amplitude of the noise. Regarding the numbers from above this implies that a way has to be found to suppress the noise to a maximum of $4\,\%$ of the signal expected from a 2D density of $n_{2D} \simeq 0.5\,\mu\text{m}^{-2}$. In other words, the signal to noise ratio has to exceed a value of $SNR \simeq 25$. I find that for optimal imaging parameters an average over 2300 images is required to meet these conditions. It is not realistic that such an average can be performed since long term drifts, for example in the alignment of the laser beams, ultimately limit the achievable enhancement of the signal to noise ratio by averaging.

However, our setup allows for an averaging along the y-axis, i.e. over the different one-dimensional tubes. The noise suppression caused by this average has not been taken into account so far. Since the density distribution slightly differs from tube to tube it is not as efficient as it would be if the density profile was precisely the same in all the tubes. Yet, a first estimate predicts this effect to be small, such that incorporating an average over 100 tubes still improves the signal to noise ratio by a factor of almost ten. In this framework the number of images that have to averaged to make the Friedel oscillations visible reduces to 25. Even though it is

likely that the calculation underestimates the impact of the density fluctuations this result suggest that Friedel oscillations might be observable within an average over a reasonable number of images in our experiment. In an ultracold atom experiment working with a heavier atomic species than ^{6}Li the required signal to noise ratio of $SNR = 25$ might be achievable more easily. The higher mass for example of fermionic ^{40}K allows for longer imaging times and thus an enhanced signal to noise ratio of an individual image. Fermionic ^{173}Yb again is even heavier than ^{40}K. If the imaging time τ was expanded to 100 µs an average over only 100 images provided a $SNR > 25$ even without the tube average.[12] For this reason it certainly should be easier to perform the presented experiment with heavy fermionic atoms rather than with ^{6}Li.

In order to discuss the signal to noise ratio of our experiment the principles of our absorption imaging shall be briefly presented. We apply an imaging pulse of resonant laser light to the atoms, i.e. $\omega_{laser} = \omega_0$, where ω_0 is the frequency of the D2 transition of ^{6}Li.[13] The atoms scatter the photons and therefore cast a shadow onto the charge-coupled device (CCD) camera. Under the assumptions that

- only single scattering events occur,
- the laser light remains resonant to the D2 transition throughout the duration of the imaging pulse and
- that the laser pulse itself does not change the density distribution

one finds the decrease of the probe intensity $I(x, y, z)$ to be described by the Beer-Lambert law

$$\frac{d}{dz} I(x, y, z) = -n_{3D}(x, y, z) \frac{\sigma_{abs}}{1 + I(x, y, z)/I_{sat}} I(x, y, z), \tag{3.60}$$

where z is the propagation direction of the beam. n_{3D} denotes the atomic density, $\sigma_{abs} = 3\lambda^2/2\pi$ the scattering cross-section and $I_{sat} = \frac{\pi}{3} \frac{hc\Gamma}{\lambda^3}$ is the saturation intensity [55, 58]. $\lambda = \frac{2\pi c}{\omega_0}$ is the corresponding wavelength to the atomic transition and $\Gamma = 5.87\,\mathrm{MHz}$ is the corresponding line width [57]. The Beer-Lambert law accounts for saturation effects and it is derived in full detail for example by Foot [55]. equation

[12] These numbers still refer to ^{6}Li. For a precise result the absorption cross-section and the saturation intensity have to be replaced according to the atomic species.
[13] For detailed information on the transitions in ^{6}Li see Gehm [57].

(3.60) is an ordinary differential equation that can be solved by separation of variables resulting in an expression for the two-dimensional density:

$$n_{2D}\sigma_{abs} = -ln(T(x,y)) + s(x,y)(1 - T(x,y)), \tag{3.61}$$

where $n_{2D} = \int_{-\infty}^{\infty} dz\ n_{3D}(x,y,z)$ was used for the two-dimensional density and $T(x,y) = I_{out}(x,y)/I_{in}(x,y)$ for the transmission coefficient of the atomic cloud. The saturation $s(x,y) = I_{in}(x,y)/I_{sat}$ is the imaging intensity relative to the saturation intensity. I refer to $I(x,y,-\infty)$ as I_{in} and to $I(x,y,-\infty)$ as I_{out}, which are both measurable quantities. If I_{sat} is known, the density n_{2D} can be deduced from a measurement of I_{in} and I_{out}.

The number of photons $N_{ph} \propto I$ hitting a pixel during the imaging process is transferred into counts $C \propto N_{ph}$ by the CCD camera, i.e. a digital signal consisting of a single integer number. Expressed in counts equation (3.61) reads

$$n_{2D}\sigma_{abs} = -ln\left(\frac{C_{out}(x,y)}{C_{in}(x,y)}\right) + \frac{C_{in}(x,y) - C_{out}(x,y)}{C_{sat}}, \tag{3.62}$$

where $C_{in} \propto I_{in}$, $C_{out} \propto I_{out}$ and $C_{sat} \propto I_{sat}$. The product $n_{2D}\sigma_{abs} = OD$ is called the optical density. In order to determine the signal to noise ratio

$$SNR = \frac{n_{2D}}{\sqrt{\sigma^2_{n_{2D}}}} = \frac{OD}{\sqrt{\sigma^2_{OD}}} \tag{3.63}$$

we need to quantify the error on the optical density σ_{OD}. From error propagation it follows that

$$\sigma^2_{OD} = (1+s)^2\left(\frac{\sigma_{C_{in}}}{\overline{C}_{in}}\right)^2 + (1+sT)^2\left(\frac{\sigma_{C_{out}}}{\overline{C}_{out}}\right)^2, \tag{3.64}$$

where the overbars indicate expectation values. This notation is used for all expectation values in the following. This equation actually assumes only C_{in} and C_{out} to be defective and C_{sat} to be precise. In order to evaluate this expression I will derive an expression for the error on C_{in} and C_{out}. Doing so, we have to take into account two aspects: namely the noise on a single density image and the fact that two images are taken to measure each of the two quantities. We will show that the variance[14] of

[14]We use the words error and variance equivalently. The variance is the squared standard deviation.

counts on a single pixel for an individual image is given by

$$\sigma_C^2 = \kappa^2 Q_e \overline{N}_{ph} + \sigma_{tech}^2, \tag{3.65}$$

where σ_{tech} denotes a technical noise that will be quantified later on, Q_e is the quantum efficiency of the camera and $\overline{N}_{ph}$ is the expectation value of photons hitting the camera pixel during the imaging process. κ is a transformation coefficient that indicates the number of counts per photo electron accounting for the gain G and the sensitivity S of the camera. The technical error simply adds to the intrinsic photon shot noise multiplied with quantum efficiency and the squared transformation coefficient. Taking into account the two-image measurement scheme we find the quantities entering equation (3.64):

$$\overline{C}_{in} = \overbrace{\kappa Q_e \left(\overline{N}_{in}^{probe} + \overline{N}_{in}^{leak}\right)}^{\text{image I}} - \overbrace{\kappa Q_e \overline{N}_{in}^{leak}}^{\text{image II}} = \kappa Q_e \overline{N}_{in}^{probe} \tag{3.66}$$

$$\overline{C}_{out} = \kappa Q_e T \left(\overline{N}_{in}^{probe} + \overline{N}_{in}^{leak}\right) - \kappa Q_e T \overline{N}_{in}^{leak} = \kappa Q_e T \overline{N}_{in}^{probe} \tag{3.67}$$

$$\sigma_{C_{in}}^2 = \kappa^2 Q_e (\overline{N}_{in}^{probe} + 2\overline{N}_{in}^{leak}) + 2\sigma_{tech}^2 \tag{3.68}$$

$$\sigma_{C_{out}}^2 = \kappa^2 Q_e (T^2 \overline{N}_{in}^{probe} + 2\overline{N}_{in}^{leak}) + 2\sigma_{tech}^2 \quad . \tag{3.69}$$

N_{in}^{probe} is the incident number of photons from the probe beam and N_{in}^{leak} is the number of photons from so-called leak light. For a given optical density OD and saturation s the transmittance T is determined by equation (3.60) and according to equation (3.63) the signal to noise ratio reads

$$SNR(s, OD) = \frac{OD}{\sqrt{(1+s)^2 \left(\frac{\sqrt{\kappa^2 Q_e (\overline{N}_{in}^{probe} + 2\overline{N}_{in}^{leak}) + 2\sigma_{tech}^2}}{\kappa Q_e \overline{N}_{in}^{probe}}\right)^2 + (1+sT)^2 \left(\frac{\sqrt{\kappa^2 Q_e (T^2 \overline{N}_{in}^{probe} + 2\overline{N}_{in}^{leak}) + 2\sigma_{tech}^2}}{\kappa Q_e T \overline{N}_{in}^{probe}}\right)^2}}. \tag{3.70}$$

First, the error on the counts of an individual pixel shall be derived for a single image. Figure 3.14 gives an overview on the processing of the photons that are captured by the camera and the noise that enters the process. The main sources of noise that will be considered in this derivation are the photon shot noise, that noise that arises from the translation of photons into photo electron due to a quantum

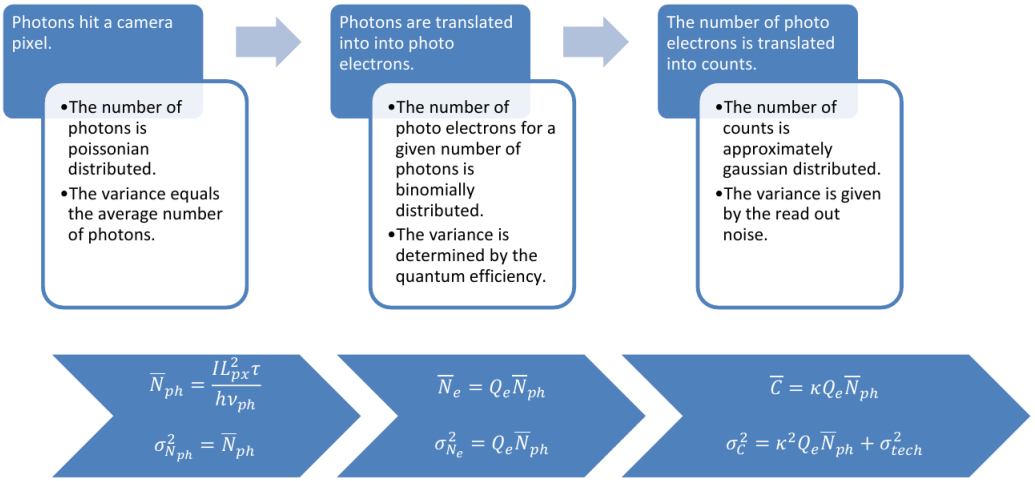

Figure 3.14: Schematic representation of the imaging process. The main noise sources entering the imaging process are the photon shot noise, the noise that arises from the translation of the photons into photo electrons and the technical read-out noise.

efficiency $Q_e < 1$ and the technical noise that enters during the processing of the photo electrons. For a given intensity I the number of incident photons on one pixel during an imaging pulse is given by:

$$\overline{N}_{ph} = \frac{IL_{px}^2\tau}{h\nu_{ph}}, \tag{3.71}$$

where L_{px} is the linear pixel size. τ is the duration of the imaging pulse and $h\nu_{ph}$ is the energy of a single photon from the imaging light. The number of photons in a coherent light beam is poissonian distributed [59].

$$P_{ph}(N_{ph} = k, \overline{N}_{ph}) = \frac{\overline{N}_{ph}^{\,k}}{k!} e^{-\overline{N}_{ph}} \tag{3.72}$$

If the expectation value is given by $\overline{N}_{ph}$, then the variance of the photon number is $\sigma^2_{ph} = \overline{N}_{ph}$ as well. This is the first source of noise entering our measurement and at the same time it is the noise with the most intrinsic character, that is, it cannot be suppressed by technical improvement. Each photon that hits a CCD pixel creates a photo electron with the probability given by the quantum efficiency $Q_e = 0.93$. Effectively a Bernoulli experiment is performed for every photon hitting the pixel,

such that the number of photo electrons created by a fixed number of incident photons N_{ph} is binomially distributed:

$$P_e(N_e, N_{ph}) = \binom{N_{ph}}{N_e} Q_e^{N_e} (1 - Q_e)^{N_{ph} - N_e}. \tag{3.73}$$

Combining these two stochastic processes one ends up with an expectation value of $\overline{N}_e = Q_e \overline{N}_{ph}$ and a variance of $\sigma^2_{N_e} = Q_e \overline{N}_{ph}$ as well. The probability for N_e photo electrons to be generated reads

$$\begin{aligned} P(N_e, \overline{N}_{ph}) &= \sum_{N_{ph}=N_e}^{\infty} P_{ph}(N_{ph}, \overline{N}_{ph}) P_e(N_e, N_{ph}) \\ &= \sum_{N_{ph}=N_e}^{\infty} \frac{\overline{N}_{ph}^{N_{ph}}}{N_{ph}!} e^{-\overline{N}_{ph}} \binom{N_{ph}}{N_e} Q_e^{N_e} (1 - Q_e)^{N_{ph} - N_e}. \end{aligned} \tag{3.74}$$

The photo electrons load a capacitor and therefore create a voltage proportional to the number of electrons. This voltage is amplified with a gain of G and subsequently transferred into counts by dividing it by the sensitivity factor S. Noise disturbing this read-out process causes the number of counts to be gaussian distributed around their real value with a width given by the so-called read-out noise σ_{RON}. The origin of the read-out noise lies mainly within fluctuations of the capacitor voltage caused for example by thermal voltage, but it accounts also for further technical noise sources [60]. In general the read-out noise can be reduced by operating at smaller read-out rates. Usually this noise is specified in [electrons], i.e. the output signal given in counts is afflicted with a noise that corresponds to a noise of σ^2_{RON} [electrons] on the capacitor. As the amplification and the division are both linear processes the read-out noise in counts is given by $\sigma^2_{RON}\,[\text{counts}] = \sigma^2_{RON}\,[\text{electrons}]\,(G/S)^2$. In the following we will call the read-out noise in counts σ^2_{tech} and denote the quotient G/S by κ. Our CCD camera is operated with a gain of $G = 2.4$ and a sensitivity of $S = 3.83 \frac{\text{electrons}}{\text{counts}}$. The read-out noise is specified to be $\sigma^2_{RON} = 9.27\,\text{electrons} \hat{=} 5.81\,\text{counts} = \sigma^2_{tech}$. The number of counts resulting from a given number of photo electrons N_e is therefore given by

$$P(C, N_e) = \frac{1}{\sigma_{tech}\sqrt{2\pi}} \exp\left(-\frac{1}{2} \frac{(C - \overline{C}_{N_e})^2}{\sigma^2_{tech}}\right), \tag{3.75}$$

where the expectation value of the counts for a given N_e is determined by $\overline{C}_{N_e} = \kappa N_e$. To account for the probability distribution of photo electrons the probability $P(C, N_e)$

has to be summed over all values for N_e weighted with the corresponding probability $P(N_e, \overline{N}_{ph})$:

$$\begin{aligned} P(C, \overline{N}_{ph}) &= \sum_{N_e=0}^{\infty} P(N_e, \overline{N}_{ph}) P(C, N_e) \\ &= \sum_{N_e=0}^{\infty} \sum_{N_{ph}=N_e}^{\infty} \frac{\overline{N}_{ph}^{N_{ph}}}{N_{ph}!} e^{-\overline{N}_{ph}} \binom{N_{ph}}{N_e} Q_e^{N_e} (1-Q_e)^{N_{ph}-N_e} \\ &\qquad \frac{1}{\sigma_{tech}\sqrt{2\pi}} \exp\left(-\frac{1}{2}\frac{(C-\overline{C}_{N_e})^2}{\sigma_{tech}^2}\right) \end{aligned} \tag{3.76}$$

This distribution describes the probability to measure a certain number of counts. It is determined by the quantities σ_{tech}, Q_e and $\overline{N}$, where the average number of photons is again determined by the imaging intensity, duration and the effective pixel size of the camera.[15] The expectation value for the number of counts for this final distribution simply reads

$$\overline{C} = \kappa Q_e \overline{N}_{ph} \tag{3.77}$$

and the variance of the distribution is given by

$$\sigma_C^2 = \kappa^2 Q_e \overline{N}_{ph} + \sigma_{tech}^2. \tag{3.78}$$

The factor κ only scales the distribution but does not alter the signal to noise ratio since it also incorporated in σ_{tech}. This result displays the variance of the total number of counts on each pixel of the CCD camera for a single image accounting for photon shot noise, the quantum efficiency and the read-out noise. In the derivation I neglected two further noise sources, namely spurious noise that is caused by clock induced charge and dark current, i.e. noise that arises from thermal generation of electrons in the silicon [60]. Both sorts of noise are heavily suppressed in our experimental setup because we operate with short exposure times and small read-out rates. Additionally the CCD-chip is cooled to $-40°C$ preventing the generation of thermal electrons. The last source of noise that shall be considered in this work is the leak light or background light which is the reason why two images are taken for the measurement of C_{in} and C_{out} respectively. During the exposure time ϑ light from a different source than the imaging laser illuminates the chip. In order to prevent

[15] As mentioned previously, the number of counts is an integer. The rounding that arises from the conversion process from an analogue voltage to a digital integer number is not captured by the given distribution.

systematical errors due to the leak light we take in total four images (as described in [61]) for the measurement of the optical density:

1. atoms_bright. The imaging pulse is applied to the atoms and the transmitted intensity is captured by the camera.

2. atoms_dark. After the atoms have left the illumination area we take a second image using the same exposure time as for the atoms_bright image, but we do not apply any laser light. This image is supposed to capture the same leak light as the atoms_bright image, such that subtracting atoms_dark from atoms_bright removes leak light signal from the atoms_bright image.

3. no_atoms_bright. For the third image again a laser pulse is shone onto the camera but without any atoms available to scatter photons.

4. no_atoms_dark. As before, this image shall capture the same leak light as the no_atoms_bright in order to subtract it. Actually this image should equal the atoms_dark image, but for technical reasons we have to take it again.

The quantity $C_{out} \propto I_{out}$ is thus given by the difference of the two images atoms_bright and atoms_dark, whereas $C_{in} \propto I_{in}$ is determined by the difference between no_atoms _bright and no_atoms_dark. There are three quantities that actually contribute to the measurement of C_{in}. There is light of the probe laser and further there is the leak light, which is first added to the probe light and subsequently subtracted. The errors from every single light source can simply be added up and so do the variances from the individual images due to error propagation. Hence, the error of C_{in} reads

$$\begin{aligned}\sigma^2_{C_{in}} &= \sigma^2_{C_{atmos\_bright}} + \sigma^2_{C_{atoms\_dark}} \\ &= (\overline{N}^{probe}_{in} + \overline{N}^{leak}_{in})\kappa^2 Q_e + \sigma^2_C + \overline{N}^{leak}_{in}\kappa^2 Q_e + \sigma^2_C \\ &= \kappa^2 Q_e(\overline{N}^{probe}_{in} + 2\overline{N}^{leak}_{in}) + 2\sigma_C.\end{aligned} \tag{3.79}$$

For C_{out} the same arguments hold and it is

$$\sigma^2_{C_{out}} = \kappa^2 Q_e(T^2\overline{N}^{probe}_{in} + 2\overline{N}^{leak}_{in}) + 2\sigma_C. \tag{3.80}$$

Together with the equations (3.63),(3.64) and (3.77) these results yield the signal to

noise ratio as already presented in equation (3.70):

$$SNR(s, OD) = \frac{OD}{\sqrt{(1+s)^2 \left(\frac{\sqrt{\kappa^2 Q_e (\overline{N}_{in}^{probe} + 2\overline{N}_{in}^{leak}) + 2\sigma_{tech}^2}}{\kappa Q_e \overline{N}_{in}^{probe}} \right)^2 + (1+sT)^2 \left(\frac{\sqrt{\kappa^2 Q_e (T^2 \overline{N}_{in}^{probe} + 2\overline{N}_{in}^{leak}) + 2\sigma_{tech}^2}}{\kappa Q_e T \overline{N}_{in}^{probe}} \right)^2}}. \tag{3.81}$$

For a given optical density and saturation the transmittance T is determined by equation (3.61) which can be rewritten as follows:

$$T = \frac{W\left[\exp(s - OD)s\right]}{s}, \tag{3.82}$$

where W denotes the Lambert's W function [61].

Figure (3.15) displays the signal to noise ratio on a parameter space spanned by OD and s. Since the quantity $\overline{N}_{in}^{probe}$ depends linearly on the imaging time τ, the longer the imaging time is, the smaller the denominator and thus, the better the signal to noise ratio will be. Therefore the imaging time was chosen to be $\tau = 5\,\mu s$, which is the maximal time we can image without significantly altering the density distribution. We are limited by the fact that the atoms get pushed out of the focus of the microscope along the imaging axis because of the acceleration an atom experiences when it absorbs a photon. Additionally the atoms perform a random walk due to the recoils accumulated from spontaneous re-emission, such that the spatial density distribution broadens along all directions during the imaging process. These problems occur particularly for ^{6}Li because its small mass corresponds to high recoil velocities, such that the atoms travel fairly high distances during the imaging time τ. Regarding the exposure time ϑ one finds an improved signal to noise ratio for shorter exposure times as ϑ affects only the number of the leak light photons. In the experiment we operate with an optimized exposure time giving rise to approximately $\overline{N}_{in}^{leak} \simeq 25 \frac{\text{counts}}{\text{pixel}}$.[16] This number was extracted from an analysis of a set of 50 atoms_dark images. For $n_{2D} = 0.5\,\mu m^{-2}$ the maximal signal to noise of $SNR = 0.52$ is found for a saturation of $s = 1.5$. Improvement of the signal to noise ratio can be achieved by

[16] To be precise, we interrupt the keep clean cycle of the camera instead of using a shutter. But this goes to much into detail at this point. It is important to know the counts from the leak light and that their number can hardly be reduced any further.

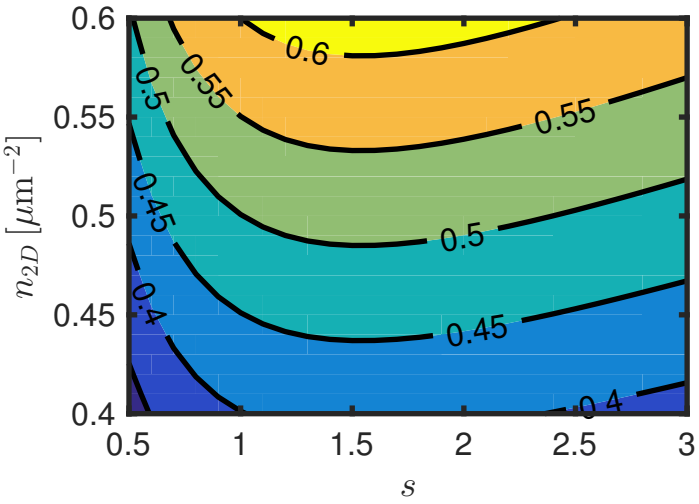

Figure 3.15: Signal to noise ration dependent on the two-dimensional density ρ_{2D} and the saturation parameter $s = I/I_{sat}$.

repetition of the same measurement. Averaging over k images reduces the error by a factor of $1/\sqrt{k}$. Satisfying the conditions that the noise amplitude is smaller than half of Θ_2 therefore requires a signal to noise ratio $SNR = 25$ which corresponds to an average over 2311 images. It is not realistic that such an average could actually make Friedel oscillations visible. There are too many components in the experiment whose stability is insufficient for such an approach. For example the alignment of the involved laser beams drifts over longer times. Furthermore, there is a fluctuation in the number of atoms loaded into the trap as well as in the temperature of the samples.

As mentioned previously, the average over the tubes, i.e. an average along the y-axis, does not only compensate the fluctuations that occur in the precise form of the potential between individual tubes, but at the same time it improves the signal to noise ratio of a single image. A rough estimate sketched in the following shows that this average is promising to significantly enhance the signal to noise ratio. Again, for perfect tubes the 1D density at the position x would be equal for all the 1D systems. Instead, the individual shape of the potential in each tube gives rise to fluctuations in the density $n_{1D}(x)$ between different tubes that we call $\delta n_{1D,y}$. How do the errors $\delta n_{1D,y}$ from the density itself and σ_{OD} from its measurement combine? Considering each tube as an individual measurement of the density distribution, it is convenient to incorporate the fluctuation of the density $\delta n_{1D,y}$ by introducing an error on the transmittance T. Dividing the one-dimensional fluctuation by the tube

spacing and multiplying it with the absorption cross-section gives a corresponding fluctuation in the optical density $\delta_{OD} = \delta n_{1D,y}/0.5\,\mu\text{m}\ \sigma_{abs}$. Since T is given by equation (3.82) a fluctuation on the optical density manifests itself as a fluctuation on the transmittance given by

$$\sigma_T^2 = \left(\frac{W[\exp(s - OD)s]}{1 + W[\exp(s - OD)s]} \exp(s - OD) \right)^2 \delta_{OD}^2. \tag{3.83}$$

Since we did not investigate the precise distribution of the density fluctuations $P(n_{1D,y})$ the distribution of the transmittance $P(T)$ is unknown. For simplicity, let us assume a gaussian distribution for T, which is likely to be wrong but nonetheless may serve to derive a first estimate on the impact of σ_T. The error σ_T will only contribute to the distribution of C_{out} in the way, that the number of transmitted photons $N_{out} = N_{in}T$ hitting a pixel is now given by the usual poissonian distribution multiplied with the gaussian distribution for T. As a result, the error $\sigma_{C_{out}}$ changes to

$$\sigma_{C_{out}}^2 = \kappa^2 Q_e (\overline{T}^2 \overline{N}_{in}^{probe} + \sigma_T^2 \overline{N}_{in}^{probe^2} + \sigma_T^2 \overline{N}_{in}^{probe} + 2\overline{N}_{in}^{leak}) + 2\sigma_{tech}^2. \tag{3.84}$$

Apart from that the formula for the signal to noise ratio remains the same. The study of the density distribution in different tubes of a flattened potential yielded a standard deviation of $\delta n_{1D,y} \simeq 0.01\,\mu\text{m}^{-1}$ leading to a fluctuation in the transmittance of $\sigma_T \simeq 0.01$. From these numbers it follows that the signal to noise ratio for a saturation of $s = 1.5$ and an average 2D density of $\overline{n}_{2D} = 0.5\,\mu\text{m}^{-2}$ decreases from 0.52 to 0.51. Even though this result is far from being precise it indicates, that the fluctuations in the density will not drastically worsen the signal to noise ratio. Now that we introduced a signal to noise ratio that takes into account a fluctuation of the optical density itself, it is meaningful to regard each tube as an individual measurement. Thus an average over 100 tubes leads to an increase in the signal to noise ratio by a factor of ten. In this framework we find a signal to noise ratio of $SNR = \mathcal{O}(5)$ in a single image. Correspondingly, to accomplish the condition that Θ_2 exceeds twice the amplitude of the noise an average over only 25 images is required. Most probably, the impact of $\delta n_{1D,y}$ is underestimated in these considerations and thus more than 25 images are needed to make Friedel oscillations visible, but still the result suggests that a detection of Friedel oscillation might be possible within an average over a reasonable number of images.

3.6 Conclusion and outlook

After all, we have to state that it still remains questionable whether or not Friedel oscillations can be successfully observed in our experimental setup. Our main concern was that we might not be able to create barriers of sufficient steepness. However, the calculation revealed that the quality of experimental measurements will most likely not be limited by the steepness of the barrier. Rather the combination of the limited resolution of our imaging system and the $1/n_{1D}$ dependence of the Friedel wavelength forces us to work with very dilute samples resulting in a low signal to noise ratio. Furthermore, it is uncertain whether we will be able to accomplish the requirements regarding the temperature $T/T_f < 0.1$ and the homogeneity of the potential $\delta V \ll E_f$. Even though the simulation in Section 3.4 showed that the generation of a suitable potential for the observation of Friedel oscillations by means of a DMD is in general possible, the proposed method remains to be tested in the experiment.

However, other experiments work with higher resolutions allowing for higher densities or with heavier atoms as for example ^{40}K or ^{173}Yb. Due to the higher atomic masses much longer imaging pulses can be applied yielding higher signal to noise ratios. For example for a density of $n_{2D} = 1\,\mu\text{m}^{-2}$ and an imaging time of $\tau = 50\,\mu\text{s}$ a signal to noise ratio of about 3.7 can be reported for optimal saturation.[17] An average over only 100 images would thus suppress the noise to below 3% even without the tube average.

Besides, there exist further methods to possibly improve the signal to noise ratio that could also be implemented in our experiment. If for example a blue detuned laser beam was used for the creation of the 1D tubes the distance between the tubes could be diminished leading to an increase of the two-dimensional density without changing the one-dimensional density. Loading two or more layers of the 2D-lattice results in an enhanced 2D density as well, without affecting the 1D density of the individual 1D systems. This approach would require a high degree of similarity between the loaded layers regarding their precise potential shape, their density and their temperature. Next, imaging the densities of the different spin components at the same time is comparable to taking an average over two density images corresponding to an improvement of the signal to noise ratio by a factor of $\sqrt{2}$. Additionally, it has the advantage that the technical noise enters the process only once thus the total

[17] This exemplary signal to noise ratio was calculated with parameters referring to ^{6}Li.

improvement of the signal to noise would exceed $\sqrt{2}$. A further possibility for noise reduction lies within the fact that our camera supports binning of camera pixels. In order to resolve an oscillation with a wavelength of 4 µm it does not seem reasonable to bin pixels along the x-axis, but in y-direction the binning could be particularly useful. The last option that shall be mentioned here is to Fourier transform the density image in order to detect the oscillations. It could still be tested from the simulated data whether k_f is more pronounced in Fourier space, than it is in real space.

Given that in a experiment with ultracold atoms a potential of the form of the test potential as shown in Figure 3.3 can be generated, in order to answer the question whether it is suitable to observe one-dimensional Friedel oscillations, the following considerations should be taken into account. Can temperatures of $T/T_f \lesssim 0.1$ be achieved? Higher temperatures strongly reduce the visibility of Friedel oscillations. What is the resolution R of the used imaging system? This introduces a minimal Friedel wavelength $\lambda_{FO} > 2R$ and therefore a maximal one-dimensional density $n_{1D} = 1/\lambda_{FO}$. What is then the maximal signal to noise ratio for the corresponding density? Assuming that the second amplitude of the Friedel oscillations ranges between 5 % and 10 % which is reasonable for realistic impurity potentials the noise should be below 5 % which holds for signal to noise ratios greater than 20. If these general requirements are accomplished the experiment is in general suitable for the observation of Friedel oscillations. In general it should be possible to observe Friedel oscillations in one-dimensional systems of ultracold atoms with evidence.

4 Calibration of an optical lattice and the imaging magnification based on the Kapitza-Dirac effect

The associated potential of a one-dimensional optical lattice is described by $V(y) = V_0 \cos^2(ky)$, where the amplitude V_0 is referred to as the lattice depth.[1] Such a potential can be used to restrict the dynamics of an atomic sample to the dimensions perpendicular to the lattice direction. For this purpose the lattice has to fulfill two criteria. First, the spacing between the ground state and the first excited state in an individual lattice well has to exceed the Fermi energy significantly in order to guarantee that the occupation of states in the lattice well is restricted to the ground state. Secondly, the atomic tunneling rate between lattice wells has to be smaller than the characteristic time scale of the dynamics of the system which is determined by the Fermi energy. For large enough lattice depths both criteria are fulfilled. Hence, the dimensionality of the system is reduced by one.

Since one-dimensional systems offer a vast field of research, we aim to slice a 2D system into one-dimensional tubes by means of an optical lattice. These tubes could serve for example for the study of Friedel oscillations as explained in Section 3.1. Regarding the lattice, a verification of the above criteria is required to guarantee that the tubes constitute truly independent one-dimensional systems. To measure the depth of an optical lattice the Kapitza-Dirac effect is a suitable an well established tool. We performed corresponding measurements in order to calibrate the +x-y-lattice that is provided to create the 1D tubes. The results will be presented in this chapter.

The Kapitza-Dirac effect describes the diffraction of matter from a standing light wave - the optical lattice. When an atomic ensemble that is essentially at rest is

[1] In accordance with the previous chapter I maintain the convention that the lattice is aligned along the y-axis.

exposed to a short pulse of a standing light wave a fraction of the atoms receives a momentum of $\Delta p = 2n\hbar k_{ph}$, where $\hbar k$ is the wave vector of the standing light wave and n denotes the diffraction order. For a lattice created by two laser beams this momentum transfer originates from n two-photon processes in which an individual atom first absorbs a photon from the one beam and secondly re-emits it into the other. After a certain time of flight τ the separation of the diffraction orders in momentum space manifests itself as a spatial separation given by $\Delta x = 2\hbar k\tau/m$. From absorption images one can extract the relative populations of the diffraction orders which are related to the lattice depth V_0. By comparing the separation of the diffraction orders in real space Δ_{real} with the equivalent distance in the camera plane Δ_{image} the magnification of the imaging system can easily be derived from these images as well. This method provides a higher accuracy than former methods used for the determination of our magnification.

The evaluation of the data yielded a lattice depth of

$$V_0(P_l) = 6.14(22)\ \frac{E_r}{\mathrm{W}}\ P_l, \tag{4.1}$$

where P_l denotes the power of the +x-y-lattice beam in Watt. $E_r = \hbar^2 k_{ph}^2/2m$ is the recoil energy, that is transferred in any absorption or emission process, m being the mass of the particle. The measured value is only a tenth of the value predicted by a calculation taking into account the lattice beam parameters. This discrepancy is attributed to difficulties in the evaluation scheme and a misalignment of the laser beam in Section 4.4.2.

For the magnification I found

$$M = 37.2(2). \tag{4.2}$$

This value for the magnification deviates from values determined in former measurements. Nevertheless, considering the high precision of this method a high level of validity can be ascribed to this result. Since long term drifts in the experiment alter the position of traps, a refocusing of the imaging microscope is required in certain temporal intervals accompanied by a change of microscope position along the z-axis. We took the opportunity to investigate the dependence of the magnification on the position of the microscope along the z-axis Z_m. The results suggest a linear

dependence of the form

$$\partial M/\partial Z_m = 0.048(20)\,\mu\mathrm{m}^{-1}. \tag{4.3}$$

The magnification M reported above refers to a value of $Z_m = 45\,\mu\mathrm{m}$. At this position the microscope was focused to the squeeze position at that time.

In the following I introduce the Kapitza-Dirac effect before I proceed to a detailed discussion on the evaluation of the recorded data.

4.1 The Kapitza-Dirac effect

The diffraction of light by a matter grating is a well studied phenomenon in physics. If both light and matter exhibit wave and particle characteristics, should the reverse process, i.e. the diffraction of a matter wave by light, not work as well? The answer is yes. In what is known as the Kapitza-Dirac effect, a matter beam is diffracted by a standing wave of light, acting as a grating.

Already in 1933 Kapitza and Dirac proposed to reflect a beam of electrons from a standing wave of light [62], aiming to observe stimulated scattered radiation. If one thinks of the standing wave as of two counterpropagating plane waves, then both waves can individually interact with the electrons. An electron passing through such a light field would first absorb a photon from one of the plane waves and subsequently re-emit it into the counterpropagating plane wave in a process of stimulated emission. The total momentum transfer necessarily is

$$\Delta p = 2\hbar k_{ph} = 2\frac{h\nu}{c}. \tag{4.4}$$

Here, ν is the frequency of the standing wave light and c is the speed of light. Kapitza and Dirac predicted the fraction of electrons in the beam undergoing such a two photon process to be on the order of 10^{-14} considering the strongest light sources available at that time. Hence, before the invention of the laser no attempts were made to observe the Kapiza-Dirac-effect. It was only in 2001 that a successful diffraction of an electronic beam by a standing light wave could be reported by Freimund et al. [63], whereas already in 1986 Gould et al. exploited the effect to diffract neutral atoms from an optical lattice [64]. The reason why the Kapitza-Dirac effect was first observed with neutral atoms is their enhanced interaction with light compared to bare electrons.

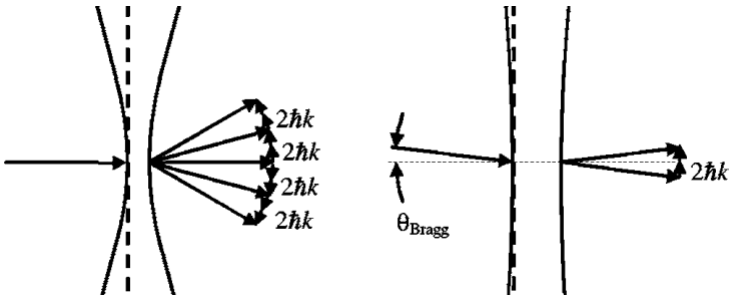

Figure 4.1: Schematic representation of the Kapitza-Dirac effect. For a narrow standing light wave diffraction occurs due to the short interaction time (left). For the wide standing light wave Bragg scattering takes place (right). Reprinted from [65].

The particle picture introduced by Kapitza and Dirac is based on the second quantization of the light field. A photon of momentum $\hbar k$ is annihilated while one of the momentum $-\hbar k$ is created. Correspondingly, an electron (or a neutral atom) of an momentum p_{in} is annihilated and one carrying the momentum $p_{in} + 2\hbar k$ is created. However, a rigorous formalization of this process has not been carried out yet within the framework of quantum electrodynamics [65] . Kapitza and Dirac only considered the case where momentum and energy conservation hold, leading to a Bragg condition for the reflection of the electron beam [62]

$$\lambda_{e^-} = \lambda_{ph} \cos(\Theta), \tag{4.5}$$

where Θ is the angle between the incident beam and the plane perpendicular to the propagation direction of the light. Here, the lattice spacing D from the common Bragg condition $\lambda = 2D \sin(\Theta)$ is replaced by half the wavelength of the light $\lambda_{ph}/2$. λ_{e^-} is the de Broglie wavelength of a single electron. Apart from Bragg scattering, diffraction of electrons from a standing light wave can also be observed, seemingly breaking the law of energy conservation. This contradiction can be dissolved by arguments based on the Heisenberg uncertainty law [65]. In principle the finite interaction time between light and electrons is related to an uncertainty of the photon energy ΔE_{ph} allowing for an energy mismatch between the absorbed and the emitted photon. This explains why diffraction occurs for short interaction times whereas Bragg scattering dominates for longer interaction times when ΔE_{ph} decreases.

As an alternative to the particle picture employed by Kapitza and Dirac, the problem can also be addressed theoretically in semiclassical wave picture which is more practical for calculations. This approach, which is discussed detail by Gadway et al.

[66], treats the light as a classical electromagnetic standing wave and incorporates the interaction via an effective potential. It is particularly useful, since it leads to the equations (4.12) and (4.13) that relate the population of diffraction orders to the lattice depth. In a classical standing wave of light, an electron would experience a so-called ponderomotive potential with a periodicity of $\lambda/2$. In the case of the neutral atom, the intensity dependent energy shift of the ground state manifests in the form of the dipole potential, which is proportional to the intensity of the light field and hence exhibits the same periodicity of $\lambda/2$ [67]. Whereas the original proposal assumed the electrons to travel through a light field, in our experiment a light pulse of the duration τ is applied to the atoms, which are essentially at rest. These cases can be transformed into one another by the interchange of one spatial coordinate with the time coordinate and hence they can be treated analogously.

During the time of interaction between light and matter the dynamics of a single particle are determined by the Hamilton operator

$$\hat{H} = -\frac{\hbar^2}{2m}\frac{\partial^2}{\partial y^2} + V_0 \cos^2(ky), \tag{4.6}$$

where m is the atomic mass, $k = 2\pi/\lambda_{ph}$ is the wave vector of the light and V_0 is the amplitude of the dipole potential given by

$$V_0 = \frac{3\pi c^2}{2\omega_0^3}\frac{\Gamma}{\Delta} I_0, \tag{4.7}$$

if the light predominantly couples to a single transition. For a coupling to multiple atomic transition, a weighted sum over all of them has to be taken [67]. For the description of the atomic wave function a basis of plane waves $\{e^{in2kz} | n \in \mathbb{Z}\}$ is considered. Any wave function can be expanded as

$$\psi(t) = \sum_{n=-\infty}^{\infty} c_n(t) e^{in2kz}. \tag{4.8}$$

Inserting this expression into the one particle Schroedinger equation leads to a set of

coupled differential equations[2]:

$$i\frac{dc_n}{dt} = \left(\epsilon n^2 + \frac{V_0}{2\hbar}\right) c_n + \frac{V_0}{4\hbar}(c_{n+1} + c_{n-1}). \tag{4.9}$$

$\epsilon = \hbar k^2/2m$ depicts the kinetic energy of the n-th mode in units of $\hbar$. Neglecting the kinetic energy gives rise to the straightforward analytical solution

$$c_n(t) = (i)^n e^{-(i/\hbar)V_0 t} J_n(V_0 t/\hbar), \tag{4.10}$$

where the J_n denote the Bessel functions of the first kind. The regime where the atomic kinetic energy remains small in comparison to the lattice depth is called either Raman-Nath regime [66], diffractive regime [65] or thin grating limit [68]. This is where diffraction dominantly occurs. The condition

$$\tau\omega_{ho} \ll 1 \tag{4.11}$$

is claimed to justify the negligence of the kinetic energy term in equation (4.10) and thereby to guarantee the Raman-Nath regime to apply [66, 68]. The frequency $\omega_{ho} = \sqrt{2V_0k^2/m}$ results from a harmonic approximation of a minimum of the lattice potential and τ denotes the total duration of the interaction. This condition ensures, that an atom does not oscillate in a lattice well. After the interaction time τ the probability P_n of having received the momentum $p_z = n2\hbar k$ for an individual atom is given by the modulus squared of the corresponding expansion coefficient $c_n(\tau)$

$$\begin{aligned} P_n &= |c_n(\tau)|^2 \\ &= J_n^2(V_0\tau/\hbar). \end{aligned} \tag{4.12}$$

If the criteria for the Raman-Nath regime is not fulfilled, the evolution of the coefficients $c_n(t)$ demands a more complex treatment. Gadway et al. discuss an analytical solution for another regime, namely the weak pulse regime defined by the condition $V_0 < 4E_r = 4(\hbar k)^2/2m$ [66]. For the occupation of the first diffraction order they

[2] An implicit assumption of this approach is, that the interaction energy between the light and a single atom is orders of magnitude stronger than the interatomic interaction, which is correspondingly neglected.

find the equation

$$P_{\pm 1} = \frac{1}{1 + 2\frac{(4E_r)^2}{V_0^2}} \sin^2\left(\frac{\tau}{2\hbar}\sqrt{\frac{V_0}{2} + (4E_r)^2}\right). \tag{4.13}$$

While it took decades from the prediction to the experimental observation of the Kapitza-Dirac effect, it then rapidly established as a common tool to calibrate optical lattices for ultracold atoms. The relative population of the diffraction orders can easily be extracted from absorption images. A comparison with the theory yields the lattice depth.

4.2 Description of the experiment

Aiming for a precise lattice calibration and a characterization of the magnification of the imaging system we performed the following experiment yielding Kapitza-Dirac diffraction of atoms from an optical lattice: We trapped ^{6}Li-atoms in the FORT trap[3] and cooled the ensemble evaporatively in order to achieve high densities and therewith a high signal to noise ratio. Subsequently, the sample was released from the FORT and immediately exposed to a short pulse of the +x-y-lattice of the duration $\tau = \mathcal{O}(\mu s)$. After the application of the standing wave light pulse the system was given the time $\Theta = \mathcal{O}(\text{ms})$ to evolve, before an absorption image of the atomic density was taken.

The small waist of $w_x = 25\,\mu m$ makes the FORT particular suitable for this experiment, since it ensures that already after a short time of flight a spatial separation of the diffraction orders is achieved. For the observation of the Kapitza-Dirac effect the precise temperature is irrelevant as long as the spatial separation of the diffraction orders significantly exceeds their thermal broadening after the time of flight. For an efficient cooling of the atoms the experiments were performed in the regime of attractive interactions inducing the formations of loosely bound ^{6}Li-dimers. [4] The power of the +x-y-lattice beam was adjusted manually. It was monitored with an oscilloscope displaying the signal of a photodiode that measured a small outcoupled intensity fraction. Since the light pulse was not power controlled for the lack of an

[3] For a description of the optical dipole traps see Chapter 2.

[4] In the evaluation the changed particle properties have to be taken into account. The dimers are twice as heavy as atoms and also their polarizability is doubled. As a result they experience four times the lattice depth as atomic ^{6}Li measured in units of the corresponding recoil energy.

appropriate controller, we verified that the fluctuations of the power were below 5% of the applied power during a single light pulse as well as between different pulses. In this setup the following parameters were modified depending on the purpose of the individual series of measurement:

- $\tau :=$ pulse duration
- $\Theta :=$ time of flight
- $P_l :=$ laser power
- $Z_m :=$ position of the lower microscope along the z-axis.

For $Z_m = 45\,\mu\text{m}$ the microscope was roughly focused to the position of the FORT. In order to determine the magnification for this position we recorded a data set where Θ was varied expecting M to be robust against any change of Θ. To calculate the lattice depth V_0 for a given laser power it is mandatory to vary the pulse duration τ such that the equation (4.12) or (4.13) can be fitted to the data points. Repeating this procedure for various laser powers allows to relate the lattice depth $V_0(P_l)$ to the laser power. A corresponding second data set was recorded. Finally, in order to characterize the dependence of the magnification on the position of the microscope in z-direction, we performed a series of measurements only varying Z_m and keeping all the other parameters constant.

4.3 Method of the data evaluation

I analyzed the recorded data with the program Matlab. The essence of the evaluation code can be compactly summarized: The diffraction orders that are visible in the two dimensional density images are fitted with elliptical gaussian distributions which are all of the same widths and only differ in amplitude. This is reasonable, because all diffraction orders maintain the shape of the original cloud.[5] Since we never populated any higher diffraction orders than the first one, the fits must provide three gaussian peaks. Figure (4.2) exemplary shows a fit to the density distribution that results from the Kapitza-Dirac effect. Once the density is captured in the fits one can extract the

[5]Strong interatomic interactions can alter the form of the diffraction orders. As the clouds literally move through one another many scattering events can significantly reshape the density distribution. We also observed first diffraction orders looking rather lunate than gaussian. By adjusting the interaction strength we solved this problem.

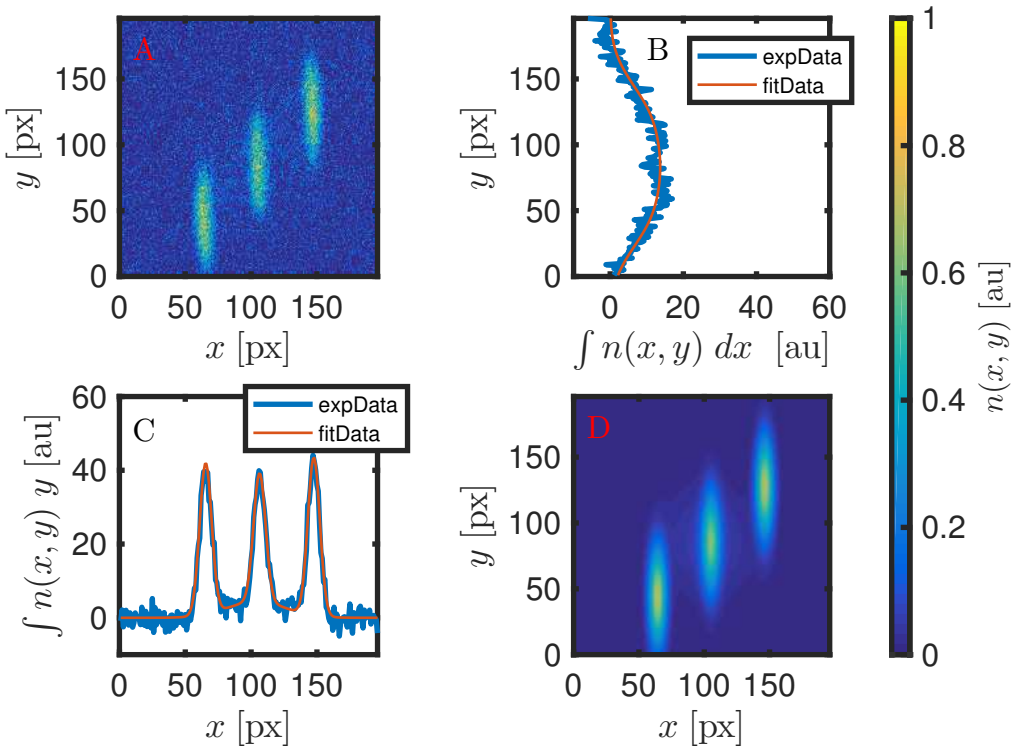

Figure 4.2: A) Density distribution of an atomic ensemble after application of a $\tau = 5\,\mu s$ light pulse and $\Theta = 800\,\mu s$ time of flight. B) A summation along the x axis of the experimental data and the fitted data. C) Summation along the y axis of the experimental data and the fitted data. D) Fitted data to A). The color bar refers to the plots A) and D).

fraction of atoms that has been transferred to the first diffraction order. This equals the probability for an individual atom of having received the momentum $p_z = \pm 2\hbar k$ given by $P_{\pm 1}$. Plotting $P_{+1} + P_{-1}$ against τ and fitting equation (4.12) or equation (4.13) to the data yields the lattice depth, as shown in Figure 4.3. The magnification of the imaging system is derived from the data by a comparison of the distance between the diffraction orders in the density image Δ_{image} and the corresponding distance in the plane of the atoms Δ_{real}. The latter is given by

$$\Delta_{real} = \frac{2\hbar k}{m}\Theta \tag{4.14}$$

and Δ_{image} is the distance in pixel in the image times the physical linear pixel size of the camera. Hence, the magnification reads

$$M = \frac{\Delta_{image}}{\Delta_{real}} = \frac{\Delta_{image} m \lambda}{4\pi\hbar\Theta}. \tag{4.15}$$

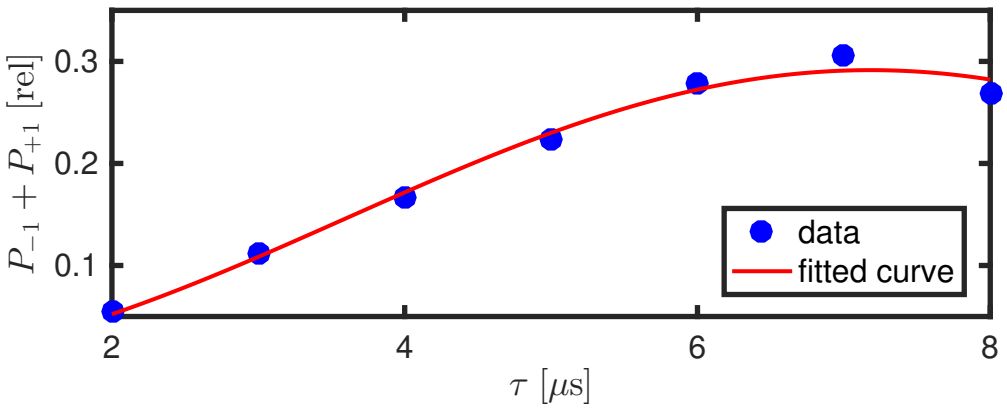

Figure 4.3: Fit of equation 4.13 to experimental populations $P_{+1} + P_{-1}$ of the first diffraction order for different pulse durations τ for a fixed laser power of $P = 0.58W$.

4.4 Results

Here, I report on the results from experiments based on the Kapitza-Dirac effect. First, the characterization of the Magnification is presented, followed by the calibration of the +x-y-lattice. I discuss certain difficulties that occurred in the analysis of the data. The results rely on the evaluation scheme presented in the former section.

4.4.1 Magnification

From measurements based on the Kapitza-Dirac effect I determined the magnification of our imaging system to be $M = 37.6(2)$ for $Z_m = 45\,\mu\text{m}$. Furthermore, the evaluation yields a linear dependence of the magnification on the position of the microscope along the z-axis of $\partial M(Z_m)/\partial Z_m = 0.048(20)\,\mu\text{m}^{-1}$. First, the measurement regarding $M(Z_m = 45\,\mu\text{m})$ is discussed and subsequently the measurement for the determination of $\partial M(Z_m)/\partial Z_m$ is addressed.

In order to precisely measure the magnification of our imaging system a set of data was taken, where the time of flight Θ was varied from 0.5 ms to 1 ms in steps of 0.1 ms. For each value of Θ an average on 50 images has been taken. All other system parameters were kept constant at $\tau = 5\,\mu\text{s}$ and $P_l = 1.3\,\text{W}$. In the analysis of the data I encountered one major issue that is described in the following, namely a fluctuation of the position of the zeroth diffraction order along the connection line between the two first diffraction orders. The data actually provides three distances that can all be evaluated individually to calculate a magnification. They are given

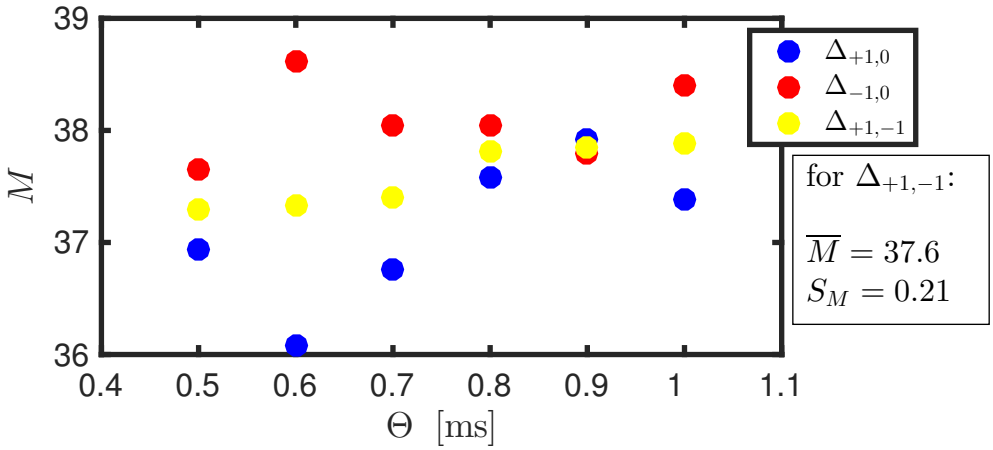

Figure 4.4: Magnification evaluated for the three types of distance for different times of flight Θ. $\overline{M}$ is the average over all $M(\Theta, \Delta_{+1,-1})$ and S_M is the corresponding error.

by the distance between

1. the $+1$ diffraction order and the zeroth order $:= \Delta_{+1,0}$,
2. the -1 diffraction order and the zeroth order $:= \Delta_{-1,0}$ and
3. the $+1$ diffraction order and the -1 diffraction order $:= \Delta_{+1,-1}$.

It turned out that these values significantly differ from one another for a given Θ. Figure 4.4 shows the results for the magnification in dependence on the time of flight for the three different distances. The magnification from $\Delta_{+1,-1}$ is the most robust against the variable Θ. However, I found

$$\frac{\Delta_{+1,0} + \Delta_{-1,0}}{2} \simeq \Delta_{+1,-1} \tag{4.16}$$

for any Θ. This behavior also occurs when all system parameters are kept constant and magnifications between individual images of the same kind are compared (not shown). These observations suggest, that the zeroth diffraction order is shifted along the connecting line between the two first diffraction orders in a seemingly random fashion. It is unlikely that the issue is caused by the fit, because it works with a higher precision. I could not find any plausible physical explanation for this behavior and therefore decided to rely on the numbers delivered by the evaluation of $\Delta_{+1,-1}$. The magnification of $M = 37.6$ was calculated by averaging over the six different values for the different times of flight. The given error of $S_M = 0.21$ is the standard deviation of the six magnifications. The derivation of a precise error would require

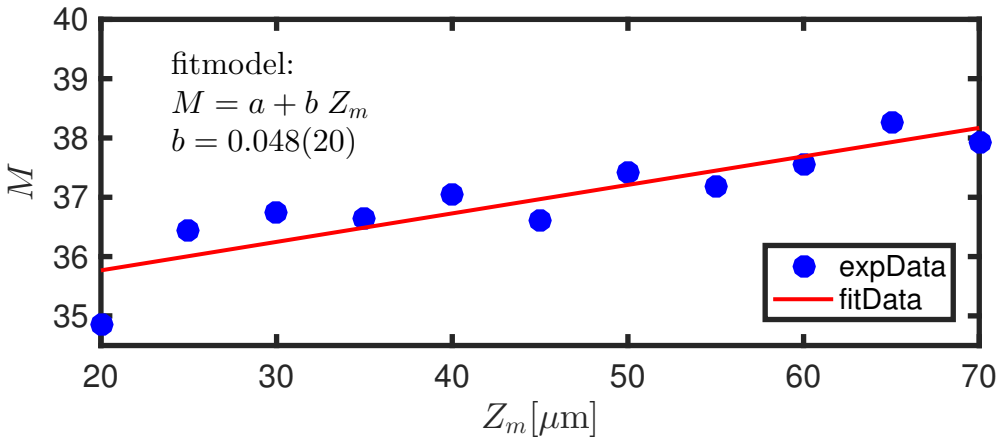

Figure 4.5: Linear fit to the magnification in dependence on the position of the lower microscope Z_m.

a more sophisticated treatment including an error propagation through all the steps of the analysis beginning with the error on the density images. However, since the standard deviation serves as a good estimate on the error I renounced the costly calculation of a precise error.

I proceed with the measurement that was carried out to characterize the linear dependence of the magnification on the microscope position. Addressing this topic we varied the variable Z_m from 20 µm to 70 µm with a step size of 5 µm. For each value of Z_m an average on 10 images has been taken. The time of flight was chosen to be $\Theta = 0.5\,\mathrm{ms}$ and the pulse duration was set to $\tau = 5\,\mu\mathrm{s}$. The laser power was $P = 1.3\,\mathrm{W}$. Since evaluating this data set I encountered the same issue as described above, I focused again on the evaluation of $\Delta_{+1,-1}$. A linear fit to the magnification yields the relation $\partial M(Z_m)/\partial Z_m = 0.048(20)\,\mu\mathrm{m}^{-1}$ as shown in Figure 4.5. For the errors on $\partial M(Z_m)/\partial Z_m$ the same arguments as for the error on the magnification hold. The given error results only from the last step of the evaluation, namely the linear fit. The influence of Z_m on the magnification is significant and has to be considered in the experiment when changing the position of the microscope.

4.4.2 Lattice calibration

Calibrating the +x-y-lattice by making use of the Kapitza-Dirac effect the lattice depth was found to be $V_0(P_l) = 6.14(22)\ \frac{E_r}{\mathrm{W}}\ P_l$. The result is based on the analysis of data for the following four laser powers: $P_l = \{0.4\,\mathrm{W},\ 0.58\,\mathrm{W},\ 0.76\,\mathrm{W},\ 1.3\,\mathrm{W}\}$. For each laser power the pulse duration τ was varied from 2 µs to 8 µs in steps of 1 µs

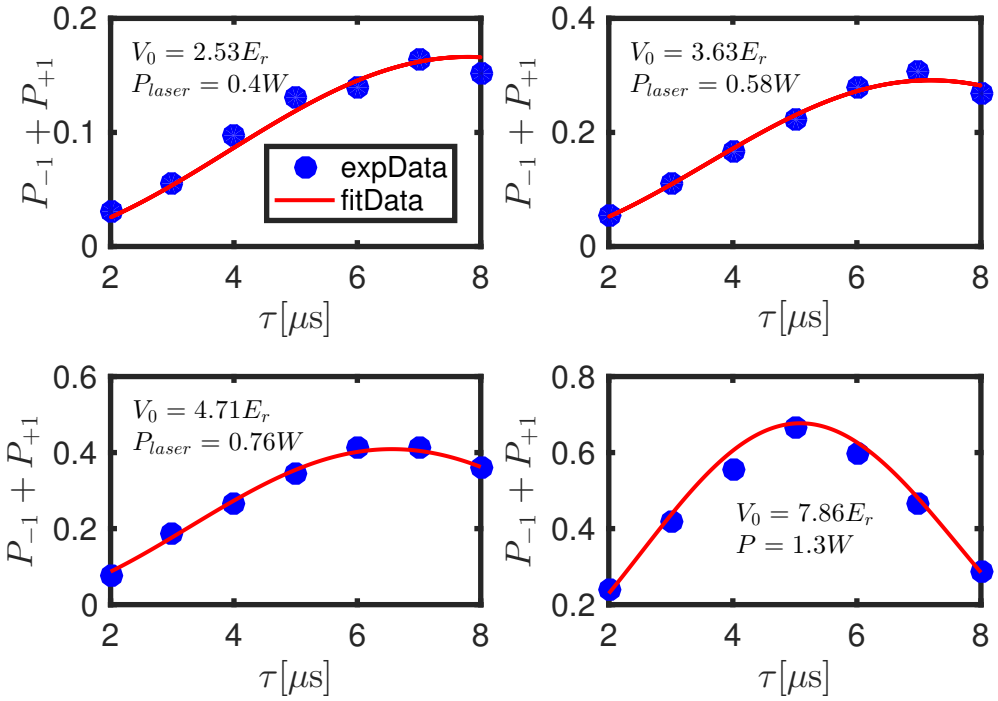

[t]

Figure 4.6: Relative occupation of the first diffraction orders P_{+1} and P_{-1} in dependence on the pulse durations τ for different laser powers P_l. The fit parameter V_0 is the lattice depth in units of the recoil energy.

and for each data point an average over 10 images was taken. As explained above, for a given laser power equation (4.13) or respectively equation (4.12) was fitted to the determined populations of the first diffraction orders as shown in Figure 4.6. The lattice depth V_0 was the only free fitting parameter. Finally the resulting lattice depths were related to the laser powers within a linear fit as done in Figure 4.7. The given error is the error resulting from the linear fit.

A further comment shall be made on the robustness of the presented results. I used the equation (4.13), that is valid in the weak pulse regime, to fit the data for $P_l = \{0.4\,\mathrm{W},\ 0.58\,\mathrm{W},\ 0.76\,\mathrm{W}\}$. According to Gadway et al. this regime is specified by the condition $V_0 \lesssim 4\,E_r$. For $P_l = 0.76\,\mathrm{W}$ this requirement is indeed not fulfilled, but it turned out equation (4.12) fitted the data worse. However, the fact that the calculated value of $V_0(P_l = 0.76\,\mathrm{W}) = 4.71\ E_r$ is not far from the weak pulse regime and additionally is well reproduced by the linear fit for $V_0(P_l)$ justifies the use of equation (4.13). For $P_l = 1.3\,\mathrm{W}$ equation (4.12) was fitted to the data, but also in this case the requirements discussed by Gadway et al. for the application of this

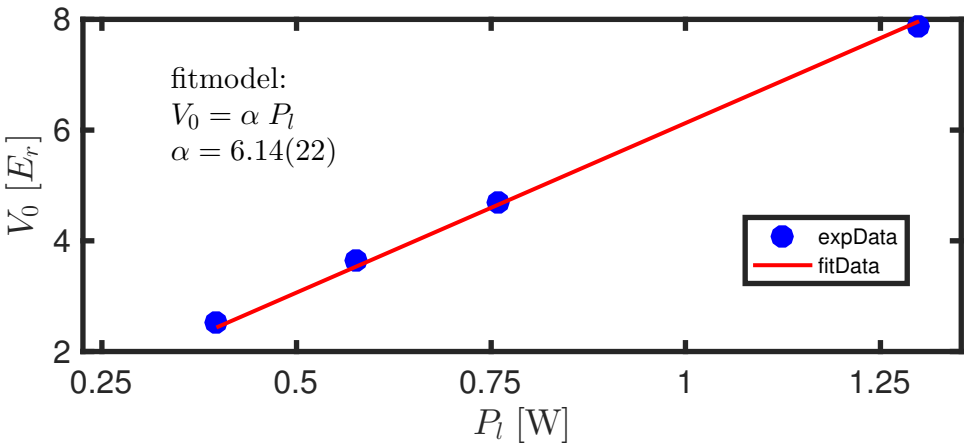

Figure 4.7: Linear fit to the determined lattice depths in dependence on the laser power.

formula are not accomplished. Whereas $\tau\omega_{ho} \ll 1$ is demanded, one finds $\tau\omega_{ho} \in [2; 8]$ for the different values of τ. Even though the data for $P_l = 1.3\,\mathrm{W}$ is reproduced quite accurately by equation (4.12) as can be seen in Figure 4.6 and the data point $V_0(P_l = 1.3\,\mathrm{W}) = 7.86\,\mathrm{E_r}$ is in agreement with the linear fit for $V_0(P_l)$, the violation of the presuppositions reduces the reliability of the results. In order to calibrate a lattice with high accuracy it is recommendable to record data under conditions that ensure the application of the Raman-Nath regime which was introduced in Section 4.1, i.e. $\tau\omega_{ho} \ll 1$. Figure 4.8 shows the value of $\tau\omega_{ho} = 2\tau E_r\sqrt{V_0/E_r}/\hbar$ for a parameter space spanned by τ and V_0. The Raman-Nath regime is limited to quite a small area where both, τ and V_0 take small values. This is due to the small mass of ^{6}Li corresponding to a high recoil energy.

Finally, the discrepancy between the measured and the theoretical lattice depth shall be discussed. Taking into account the waists of $w_x = 400\,\mu\mathrm{m}$ and $w_y = 15\,\mu\mathrm{m}$ a calculation shows, that for $P_l = 1\,\mathrm{W}$ one would expect a lattice with a depth of $V_0 = 73\ E_r$. Our experimental result reproduce only a tenth of this value. Possible explanations for this discrepancy are:

- Further investigation revealed, that power is lost at optical elements on the pathway from the fibre to the position of the atoms due to clipping.
- The retro reflecting mirror itself has a reflectivity below $R < 70\%$.
- The retro reflected beam is divergent - a cat-eye construction is suitable to remedy this problem.

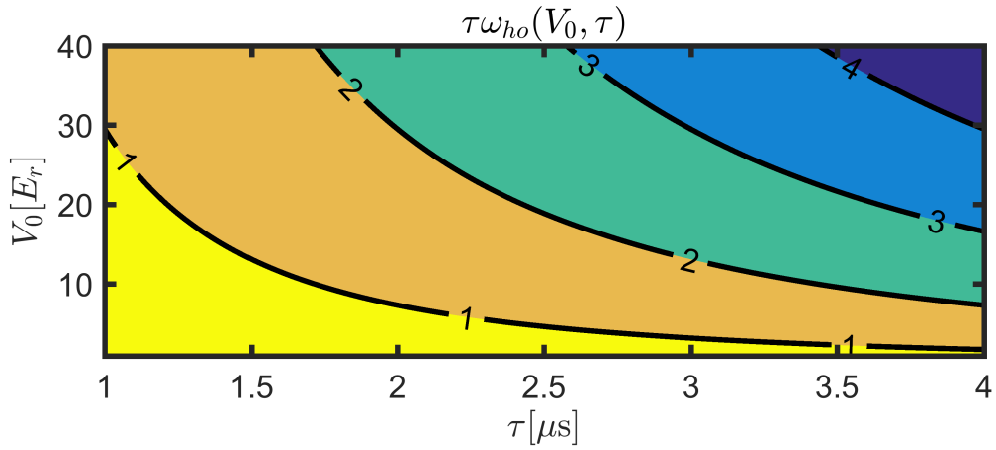

Figure 4.8: The parameter $\tau\omega_{ho}$ determining the Raman-Nath regime in dependence on τ and V_0. The Raman-Nath regime requires $\tau\omega_{ho} << 1$.

- The discussed issues in the evaluation scheme.

Unfortunately the +x-y-lattice had to be disassembled for technical reasons. When the +x-y-lattice is rebuild the above points should be considered.

4.4.3 Conclusion and outlook

We exploited the Kapitza-Dirac effect for the calibration of an optical lattice and to characterize the magnification of our imaging system. In both cases the method provided reasonable results. Regarding the magnification the measurement is ascribed a high value of validity. The calibrated lattice had to be disassembled, hence the calibration is obsolete. The lattice depth was found to be only a tenth of the expected value indicating a misalignment of the lattice beam. The evaluation code was added to the group repository and is available for the evaluation of future measurements based on the Kapitza-Dirac effect.

5 Determination of the Fermi wavevector in a 2D non-interacting homogeneous Fermi gas

In the course of this work the relation between the Fermi wavevector and the Friedel wavelength

$$\lambda_F = \pi/k_f \tag{5.1}$$

appeared several times. First measurements have been performed to determine the Fermi wavevector of an ultracold two-dimensional non-interacting Fermi gas trapped in a homogeneous potential provided by our ring trap and the 2D lattice. The method is based on the observation of the fermionic density via absorption imaging after the system was released from the ring trap and expanded freely in two dimension for the time τ. An evaluation of these time of flight images yielded a Fermi wavevector of $k_f \simeq 2.864(4)\,\mu\text{m}^{-1}$, corresponding to a wavelength for possible Friedel oscillations of $\lambda_F \simeq \mathcal{O}(1\,\mu\text{m})$ which is not resolvable in our experiment[1]. Furthermore the temperature could be determined to be smaller than $T/T_f = 0.4$ with high confidence. Even though the observation of Friedel oscillations is planned to be performed in 1D this measurement provides useful information on the 2D sample. The tools for the creation of homogeneous two-dimensional Fermi gases have only recently been implemented in our experiment such that any measurements that increase our knowledge about theses gases are helpful. Furthermore, the results confirm our expectation that in 2D the Fermi wavevector is too large for the observation of Friedel oscillations. At least one can derive a 2D density from k_f to cross check our density calibration.

[1] Note that these numbers refer to the 2D system. If this system was sliced into 1D tubes, the Fermi wavevector was smaller

5.1 Experimental setup

We prepared a two-dimensional non-interacting and homogeneous Fermi gas by loading the atoms in a single layer of the 2D-lattice. Their extent in plane was limited by the ring trap and an adequate magnetic field was applied to make the gas non-interacting. In a first step in-situ images of the sample were taken. Secondly, we released the sample from the ring trap allowing for an expansion inside the lattice layer for the time of flight $\tau = 2\,\mathrm{ms}$ before taking an image.

5.2 Evaluation

Our evaluation scheme is based on the crude approximation that the temperature of the system is given by $T = 0\,\mathrm{K}$. Further, I assume the potential to be of the form

$$V(r\varphi) = \begin{cases} 0 & \text{for} \quad r < R \\ \infty & \text{for} \quad r > R \end{cases}, \tag{5.2}$$

where r and φ are polar coordinates and R is the radius of the ring trap. For this case the phase space density in a Fermi gas trap in the potential reads

$$n(\mathbf{k}, \mathbf{r}) = n_0\,\Theta(|\mathbf{r}| - R)\Theta(|\mathbf{k}| - k_f). \tag{5.3}$$

Hence, the density is homogeneous is both, in real space and in momentum space. Θ denotes the Heaviside function and limits the density to circle around the origin in real and momentum space. From this distribution one can now calculate the total particle density at the position $\mathbf{r_0}$ after the time of flight τ.

$$\begin{aligned} n_\tau(\mathbf{r_0}) &= \int d\mathbf{r} \int d\mathbf{k}\, n(\mathbf{k}, \mathbf{r}) \delta\left(\mathbf{r_0} - \mathbf{r} - \frac{\hbar \mathbf{k} \tau}{m}\right) \\ &= \int dx \int dy \left(\frac{m}{\hbar\tau}\right)^2 n_0\,\Theta\left(\sqrt{x^2+y^2} - R\right)\,\Theta\left(\sqrt{(x-x_0)^2 + (y-y_0)^2} - \frac{\hbar\tau}{m} k_f\right) \end{aligned} \tag{5.4}$$

This integral has a simple interpretation. The question is, which particles will have traveled to the point $\mathbf{r_0}$ after the time of flight? The maximum distance a particle can travel in the time τ is $\tau\hbar k_f/m$, where m denotes the atomic mass. The assumption of zero temperature implies that all the momenta below k_f are surely occupied. Thus

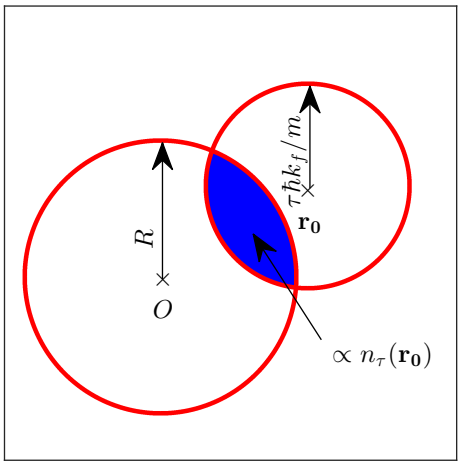

Figure 5.1: Graphical representation of the integral in Equation (5.4)

if a point $\mathbf{r_1}$ lies within the area of the ring trap ($r_1 < R$) and its distance to $\mathbf{r_0}$ is smaller than $\tau\hbar k_f/m$, then a certain fraction of the density originally located at $\mathbf{r_1}$ will have traveled to $\mathbf{r_0}$ within the time τ. If one of these two conditions is not fulfilled, there is no contribution from point $\mathbf{r_1}$ to the density at $\mathbf{r_0}$ after the time of flight. The integral in Equation (5.4) thus simply displays the overlap of a circle with a radius $\tau\hbar k_f/m$ around $\mathbf{r_0}$ with a second circle with a radius of R around the origin multiplied with the constant $(m/\hbar\tau)^2 n_0$ (see Figure 5.1). Proceeding with some maths on Equation (5.4) and replacing $\tau\hbar k_f/m = K$ one finds:

$$\begin{aligned} n_\tau(r_0,\varphi)\left(\frac{\hbar\tau}{m}\right)^2 =& K^2\frac{\pi}{2} - \frac{r_0^2+K^2-R^2}{2r_0}\sqrt{K^2-\left(\frac{r_0^2+K^2-R^2}{2r_0}\right)^2} \\ &- K^2\arctan\left(\frac{r_0^2+K^2-R^2}{2r_0}\Bigg/\sqrt{K^2-\left(\frac{r_0^2+K^2-R^2}{2r_0}\right)^2}\right) \\ &+ R^2\frac{\pi}{2} - \frac{r_0^2+R^2-K^2}{2r_0}\sqrt{R^2-\left(\frac{r_0^2+R^2-K^2}{2r_0}\right)^2} \\ &- R^2\arctan\left(\frac{r_0^2+R^2-K^2}{2r_0}\Bigg/\sqrt{R^2-\left(\frac{r_0^2+R^2-K^2}{2r_0}\right)^2}\right). \end{aligned} \tag{5.5}$$

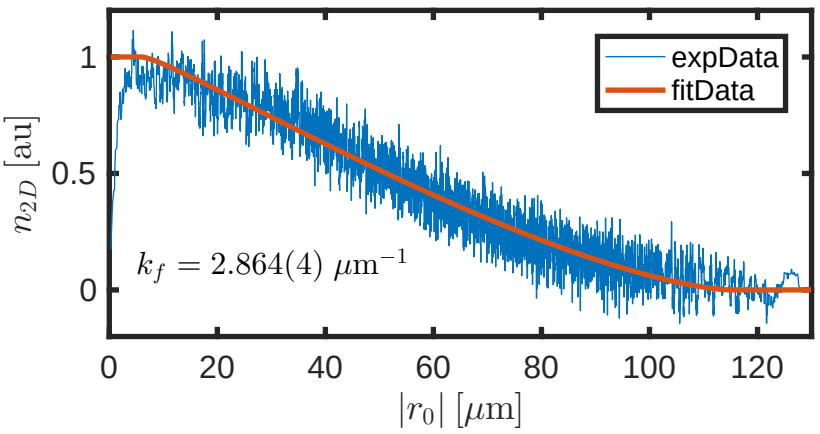

Figure 5.2: A fit of Equation (5.5) to the radially averaged measured density, where k_f serves as a fit parameter. The system was given $\tau = 2\,\mathrm{ms}$ time of flight. The data has been normalized.The error given for k_f only displays the fitting error, but does not account for the error due to approximations made in the calculation.

Logically this expression depends only on the distance of $\mathbf{r_0}$ from the origin, i.e. the resulting density distribution $n_\tau(r_0, \varphi)$ is again radially symmetric but not homogeneous in real space any more. A fit of this expression to the radially averaged density images as shown in Figure 5.2 delivers k_f as it is the only free parameter. The fit returns a Fermi wavevector of $k_f = 2.86\,\mu\mathrm{m}^{-1}$ corresponding to a density of $n_{2D} = 0.65\,\mu\mathrm{m}^{-2}$.[2] The density extracted from images using the Beer-Lamberts law is $n_{2D}^{\text{absorption}} \simeq 0.6\,\mu\mathrm{m}^{-2}$. This value shall just serve as a sanity check, hence no error has been calculated. The results roughly agree with one another and lie all within a reasonable range. Thus, they provide a first estimate for the Fermi wavevector. A corresponding wavelength of Friedel oscillations in the examined system would be $\lambda_F = \mathcal{O}(1\,\mu\mathrm{m})$. I tried to incorporate the temperature in this method by using a semi-classical description for the initial phase space density

$$n(\mathbf{r}, \mathbf{k}) = \frac{1}{(2\pi)^2} \frac{1}{\exp(\beta[\hat{H}(\mathbf{r}, \mathbf{k}) - \mu]) + 1}, \tag{5.6}$$

[2]The density was calculated with the formula $n_{2D} = k_f^2/4\pi$ which follows from the quantization of a quadratic 2D volume of constant potential.

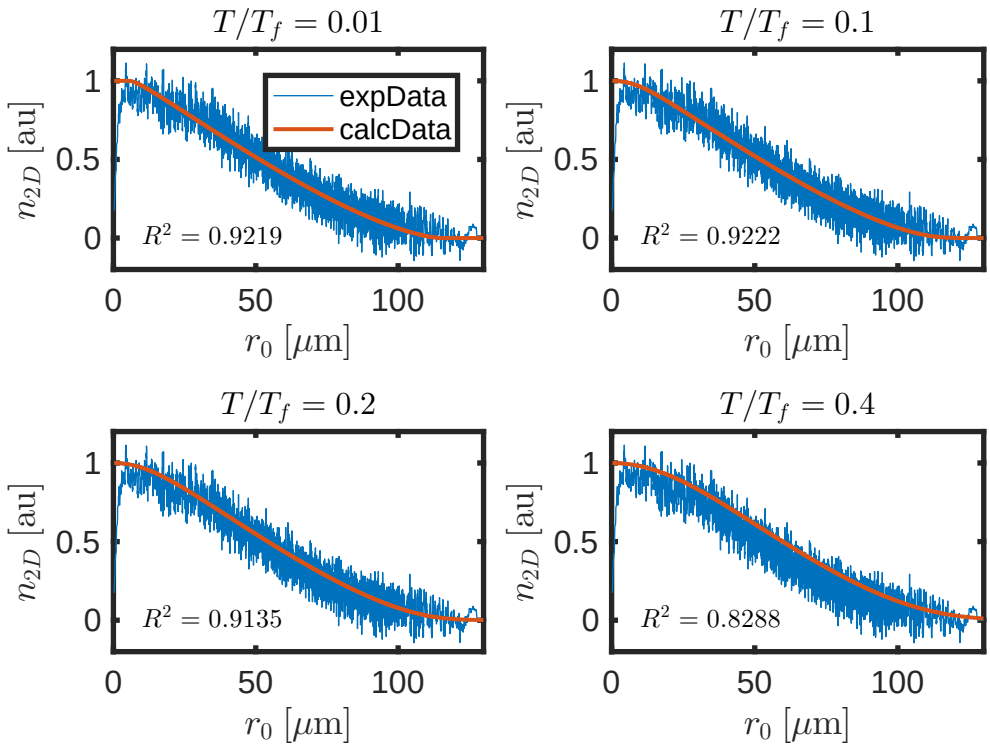

Figure 5.3: Calculated radial density distributions $n_\tau(r_0)$ based on an initial distribution given by Equation (5.6). The chemical potential was set to $\mu = \hbar^2 k_f^2/2m$ and the Hamilton operator is defined by the potential in Equation (5.2).

where $\hat{H}(\mathbf{r}, \mathbf{k}) = \hbar^2\mathbf{k}^2/2m + V(\mathbf{r})$ and μ is the chemical potential [69]. Respectively, after the time of flight the density is given by

$$n_\tau(\mathbf{r_0}) = \int d\mathbf{r} \frac{1}{(2\pi)^2} \left(\frac{m}{\hbar\tau}\right)^2 \frac{\Theta(|\mathbf{r}| - R)}{\exp(\beta[\frac{(\mathbf{r_0}-\mathbf{r})^2 m}{2\tau^2} - \mu]) + 1}. \tag{5.7}$$

Figure 5.3 displays calculated radial density distributions $n_\tau(r_0)$ for different temperatures together with the experimental data. The plots show that this method cannot serve as precise thermometer, but it delivers a first orientation regarding the temperature of the system. The results suggest that T/T_f lies rather in the range of 0.1 or 0.2 than 0.4. The R^2 value, giving a measure for the quality of a fit is the best for $T/T_f = 0.1$.[3] Nevertheless, it is obvious from the plots that the quality of the data does not permit to deduce the temperature to high level of precision.

[3] $R^2 = 1 - SSE/SST$, where $SSE = \sum_i (y_i - f_i)^2$ and $SST = \sum_i (y_i - \overline{y})^2$.. y_i is a measured value and f_i is the corresponding value of a fit expression. $\overline{y}$ is the average over the measured values.

5.3 Conclusion and outlook

Conclusively, analyzing time of flight density images of a two dimensional homogeneous and non-interacting Fermi gas allowed us to approximately calculate the Fermi wavevector $k_f \simeq 2.864(4)\,\mu\text{m}^{-1}$ and to give an upper limit for the temperature $T/T_f < 0.4$. The method requires little effort and thus is a suitable instrument to get a first benchmark on the system. Possibly, it could serve as a relative measure on the temperature. This could be realized by deriving a fit function for $n_\tau(r_0)$ with T as a free parameter or by observing the R^2 values resulting from the comparison of experimental data with calculated densities for different temperatures as done in Figure 5.3. If the R^2 value for zero temperature increases, while R^2 for $T/T_f = 0.5$ decreases in the cause of a change of the experimental cycle, it is likely that the system became cooler. A temperature dependent fit function requires an analytical solution for the integral in Equation (5.7), which I did not find so far. Maybe this method could also be extended to one-dimensional system. Consider a homogeneous one-dimensional potential bounded by the ring trap. Deactivating the ring trap allows a non-interacting Fermi gas to expand along the tube. Assuming zero temperature certainly allows to calculated a corresponding fit function with k_f as a free parameter. k_f is the same in all the tubes, despite their different lengths because it depends only on the density.

Bibliography

[1] J Friedel. The distribution of electrons round impurities in monovalent metals. *Philosophical Magazine Series 7*, 43(337):153–189, 1952.

[2] J Friedel. Electronic structure of primary solid solutions in metals. *Adv. Phys.*, 3(12):446–507, 1954.

[3] J Friedel. Metallic Alloys. *Del Nuovo Cimento*, 2:287–310, 1958.

[4] PT Sprunger, L Petersen, EW Plummer, E Laegsgaard, and F Besenbacher. Giant Friedel Oscillations on the Beryllium(0001) Surface. *Science*, 275(5307):1764–1767, 1997.

[5] B Briner, P Hofmann, M Doering, HP Rust, E Plummer, and A Bradshaw. Charge-density oscillations on Be(1010): Screening in a non-free two-dimensional electron gas. *Physical Review B*, 58(20):13931–13943, 1998.

[6] N Knorr, H Brune, M Epple, A Hirstein, M Schneider, and K Kern. Long-range adsorbate interactions mediated by a two-dimensional electron gas. *Physical Review B*, 65:1–5, 2002.

[7] C Bena. Friedel oscillations: Decoding the hidden physics. *Comptes Rendus Physique*, 17(3-4):302–321, 2016.

[8] MF Crommie, CP Lutz, and DM Eigler. Imaging standing waves in a two-dimensional electron gas. *Nature*, 363:524–527, 1993.

[9] Y Hasegawa and P Avouris. Direct observation of standing wave formation at surface steps using scanning tunneling spectroscopy. *Physical Review Letters*, 71(7):1071–1074, 1993.

[10] K Kanisawa, MJ Butcher, H Yamaguchi, and Y Hirayama. Imaging of friedel oscillation patterns of two-dimensionally accumulated electrons at epitaxially grown InAs(111)A surfaces. *Physical Review Letters*, 86(15):3384–3387, 2001.

[11] P Mallet, I Brihuega, V Cherkez, JM Gómez-Rodríguez, and JY Veuillen. Friedel oscillations in graphene-based systems probed by Scanning Tunneling Microscopy. *Comptes Rendus Physique*, 17:294–301, 2016.

[12] P Hofmann, B Briner, M Doering, HP Rust, E Plummer, and A Bradshaw. Anisotropic Two-Dimensional Friedel Oscillations. *Physical Review Letters*, 79(2):265–268, 1997.

[13] H Gawronski, J Fransson, and K Morgenstern. Real-space imaging of inelastic Friedel-like surface oscillations emerging from molecular adsorbates. *Nano Letters*, 11(7):2720–2724, 2011.

[14] T Yokoyama, M Okamoto, and K Takayanagi. Electron Waves in the π^* surface band ofthe Si(001) surface. *Physical Review Letters*, 80(16):3423–3426, 1998.

[15] C Desgranges, L Huber, and J Delhommelle. Impact of Friedel oscillations on vapor-liquid equilibria and supercritical properties in two and three dimensions. *Physical Review E*, 94(1):012612, 2016.

[16] M Bouhassoune, B Zimmermann, P Mavropoulos, D Wortmann, PH Dederichs, S Blügel, and S Lounis. Quantum well states and amplified spin-dependent Friedel oscillations in thin films. *Nature communications*, 5:5558, 2014.

[17] B DeMarco and DS Jin. Onset of Fermi Degeneracy in a Trapped Atomic Gas. *Science*, 285(5434):1703–1706, 1999.

[18] M Greiner, O Mandel, T Esslinger, TW Hänsch, and I Bloch. Quantum phase transition from a superfluid to a Mott insulator in a gas of ultracold atoms. *Nature*, 415(6867):39–44, 2002.

[19] M Greiner, CA Regal, and DS Jin. Emergence of a molecular Bose–Einstein condensate from a Fermi gas. *Nature*, 426(6966):537–540, 2003.

[20] S Jochim, M Bartenstein, A Altmeyer, G Hendl, S Riedl, C Chin, J Hecker Denschlag, and R Grimm. Bose-Einstein Condensation of Molecules. *Science*, 302(5653):2101–2103, 2003.

[21] MW Zwierlein, JR Abo-Shaeer, A Schirotzek, CH Schunck, and W Ketterle. Vortices and superfluidity in a strongly interacting Fermi gas. *Nature*, 435(7045):1047–1051, 2005.

[22] C Chin, R Grimm, P Julienne, and E Tiesinga. Feshbach resonances in ultracold gases. *Reviews of Modern Physics*, 82(2):1225–1286, 2010.

[23] Thierry Giamarchi. *Quantum Physics in One Dimension*. Oxford University Press, Oxford, 2004.

[24] R Egger and H Grabert. Friedel Oscillations for Interacting Fermions in One Dimension Reinhold. *Physical Review Letters*, 75(19):3505–3508, 1995.

[25] W Weimer, K Morgener, VP Singh, J Siegl, K Hueck, N Luick, L Mathey, and H Moritz. Critical velocity in the BEC-BCS crossover. *Physical Review Letters*, 114(9):095301, 2015.

[26] N Luick. *Local probing of the Berezinskii – Kosterlitz – Thouless transition in a two-dimensional Bose gas*. Master thesis, University of Hamburg, Hamburg, 2014.

[27] HJ Metcalf and P Van der Straten. *Laser cooling and trapping*. Springer Verlag, New York.

[28] W Weimer. *Probing superfluid properties in strongly correlated Fermi gases with high spatial resolution*. PhD thesis, University of Hamburg, Hamburg, 2014.

[29] K Morgener. *Microscopy of 2d Fermi Gases Exploring excitations and thermodynamics*. PhD thesis, University of Hamburg, Hamburg, 2014.

[30] I Bloch, J Dalibard, and W Zwerger. Many-body physics with ultracold gases. *Reviews of Modern Physics*, 80(3):885–964, 2008.

[31] KB Davis, MO Mewes, MR Andrews, NJ Van Druten, DS Durfee, DM Kurn, and W Ketterle. Bose-Einstein condensation in a gas of sodium atoms. *Physical Review Letters*, 75(22):3969–3973, 1995.

[32] MH Anderson, JR Ensher, MR Matthews, CE Wieman, and EA Cornell. Observation of Bose-Einstein Condensation in a Dilute Atomic Vapor. *Science*, 269(5221):198–201, 1995.

[33] M Bartenstein, A Altmeyer, S Riedl, S Jochim, C Chin, J Hecker Denschlag, and R Grimm. Crossover from a molecular Bose-Einstein condensate to a degenerate Fermi gas. *Physical Review Letters*, 92(12):120401, 2004.

[34] EL Raab, M Prentiss, A Cable, S Chu, and DE Pritchard. Trapping of Neutral Sodium Atoms with Radiation Pressure. *Physical Review Letters*, 59(23):2631–2634, 1987.

[35] HF Hess. Evaporative cooling of magnetically trapped and compressed spin-polarized hydrogen. *Physical Review B*, 34(5):3476–3479, 1986.

[36] Klaus Hueck. *Erzeugung und Untersuchung von ultrakalten , zweidimensionalen Fermi-Gasen*. Master thesis, University of Hamburg, Hamburg, 2013.

[37] A Görlitz, JM Vogels, AE Leanhardt, C Raman, TL Gustavson, JR Abo-Shaeer, AP Chikkatur, S Gupta, S Inouye, T Rosenband, and W Ketterle. Realization of Bose-Einstein Condensates in Lower Dimensions. *Physical Review Letters*, 87(13):130402, 2001.

[38] G Modugno, F Ferlaino, R Heidemann, G Roati, and M Inguscio. Production of a Fermi gas of atoms in an optical lattice. *Phys Rev A*, 68:11601, 2003.

[39] K Günter, T Stöferle, H Moritz, M Köhl, and T Esslinger. P-Wave interactions in low-dimensional fermionic gases. *Physical Review Letters*, 95(23):230401, 2005.

[40] H Moritz, T Stöferle, M Köhl, and T Esslinger. Exciting Collective Oscillations in a Trapped 1D Gas. *Physical Review Letters*, 91(25):250402, 2003.

[41] H Moritz, T Stöferle, K Günter, M Köhl, and T Esslinger. Confinement induced molecules in a 1D fermi gas. *Physical Review Letters*, 94(21):210401, 2005.

[42] C Kittel. *Introduction to Solid State Physics*. Wiley, 8 edition, 2004.

[43] NW Ashcroft and ND Mermin. *Solid State Physics*. Saunders College, Philadelphia, 1 edition, 1976.

[44] P Debye and E Huckel. The theory of electrolytes I. The lowering of the freezing point and related occurrences. *Physikalische Zeitschrift*, 24:185–206, 1923.

[45] J Villain, M Lavagna, and P Bruno. Jacques Friedel and the physics of metals and alloys. *Comptes Rendus Physique*, 17:276–290, 2016.

[46] Gerd Czycholl. *Theoretische Festkörperphysik*. Springer Verlag, Berlin, 3 edition, 2008.

[47] G.F. Giuliani and G. Vignale. *Quantum Theory of Electron Liquid*. Cambridge University Press, Cambridge, 1 edition, 2005.

[48] GE Simion and GF Giuliani. Friedel oscillations in a Fermi liquid. *Physical Review B*, 72(4):045127, 2005.

[49] R Egger and H Grabert. Friedel oscillations in Luttinger liquids. In *Quantum Transport in Semiconductor Submicron Structures*, pages 133–158. Springer Netherlands, Dordrecht, 1996.

[50] G Binning and H Rohrer. Scanning Tunneling Microscopy. *IBM Journal of Research and Development*, 44(1/2):279–293, 2000.

[51] ND Lang. Spectroscopy of single atoms in the scanning tunneling microscope. *Physical Review B*, 34(8):5947–5950, 1986.

[52] A Zangwill. *Physics at Surfaces*. Cambridge University Press, Cambridge, 1988.

[53] W Ketterle and MW Zwierlein. Making, probing and understanding ultracold Fermi gases. In *Ultracold Fermi Gases, Proceedings of the International School of Physics "En- rico Fermi"*, number Course CLXIV, Varenna, 20-30 June 2006, pages 95–287. IOS Press, Amsterdam, 2008.

[54] P Zupancic, PM Preiss, R Ma, A Lukin, ME Tai, M Rispoli, R Islam, and M Greiner. Ultra-precise holographic beam shaping for microscopic quantum control. *arXiv preprint*, arXiv:1604.07653, 2016.

[55] CJ Foot. *Atomic Physics*. Oxford University Press, Oxford, 2005.

[56] JH Drewes. *Aufbau eines hochauflösenden optischen Systems zur Untersuchung ultrakalter Quantengase*. Master thesis, University of Hamburg, Hamburg, 2012.

[57] ME Gehm. Properties of 6Li. `https://www.physics.ncsu.edu/jet/techdocs/pdf/PropertiesOfLi.pdf`, 2003.

[58] G Reinaudi, T Lahaye, Z Wang, and D Guéry-Odelin. Strong saturation absorption imaging of dense clouds of ultracold atoms. *Optics Letters*, 32(21):3143–3145, 2007.

[59] MO Scully and MS Zubairy. *Quantum Optics*. Cambridge University Press, Cambridge, 1997.

[60] Andor Learning Center. Sensitivity of CCD cameras. `http://www.andor.com/learning-academy/sensitivity-of-ccd-cameras-key-factors-to-consider`, September 2016.

[61] M Horikoshi, A Ito, T Ikemachi, Y Aratake, M Kuwata-Gonokami, and M Koashi. Accurate in-situ acquisition of column density of a dense cloud of ultracold 6Li atoms using absorption imaging. *arXiv preprint*, arXiv:1608.07152v1, 2016.

[62] PL Kapitza and PAM Dirac. Reflection of electrons from standing light waves. *Proc. Cambridge Philos. Soc.*, 29:297–300, 1933.

[63] DL Freimund, A Kayvan, and H Batelaan. Observation of the Kapitza - Dirac effect. *Nature*, 413(September):142–143, 2001.

[64] PL Gould, GA Ruff, and DE Pritchard. Diffraction of Atoms by Light: The Near-Resonant Kapitza-Dirac Effect. *Physical Review Letters*, 56(8):827–830, 1986.

[65] H Batelaan. Colloquium: Illuminating the Kapitza-Dirac effect with electron matter optics. *Reviews of Modern Physics*, 79(3):929–941, 2007.

[66] B Gadway, D Pertot, R Reimann, MG Cohen, and D Schneble. Analysis of Kapitza-Dirac diffraction patterns beyond the Raman-Nath regime. *Optics express*, 17(2002):19173–19180, 2009.

[67] R Grimm, M Weidemüller, and Y Ovchinnikov. Optical dipole trap for neutral atoms. *Adv. At. Mol. Opt. Phys.*, 42:95–170, 2000.

[68] YB Ovchinnikov, JH Müller, MR Doery, EJD Vredenbregt, K Helmerson, SL Rolston, and WD Phillips. Diffraction of a Released Bose-Einstein Condensate by a Pulsed Standing Light Wave. *Physical Review Letters*, 83(2):284–287, 1999.

[69] DA Butts and DS Rokhsar. Trapped Fermi gases. *Physical Review A*, 55(6):4346–4350, 1997.

Danksagung

Hiermit möchte ich mich bei all denjenigen, die zu der Entstehung dieser Masterarbeit beigetragen haben bedanken. Insbesondere richtet sich mein Dank an Prof. Dr. Henning Moritz, der mir ermöglicht hat diese Arbeit in der von ihm geleiteten Forschungsgruppe durchzuführen. Du standest stets als Ansprechpartner zur Verfügung und hast die Arbeit vor allem in ihren letzten Zügen unmittelbar begleitet. Besonders geschätzt habe ich an der Arbeit in deiner Gruppe, dass sich die Gruppenmitglieder inklusive dir in Diskussionen stets auf Augenhöhe begegnen und das Argumenten von vermeintlich Unerfahreneren die gleiche Beachtung geschenkt wird, wie den Argumenten derer die schon länger dabei sind. Aus deiner überaus konstruktiven Kritik habe ich sehr viel lernen können.

Ein weiterer Dank gilt allen Mitgliedern der Arbeitsgruppe. Ihr seid meinen oft detaillierten Nachfragen stets mit großer Geduld begegnet und habt mich unterstützt, wann immer ich eure Hilfe benötigte. Jeder einzelne von euch hat zu den Erfahrungen und den Lernfortschritten beigetragen, die ich während des letztens Jahres gemacht habe. Außerdem habe ich jede Menge 'side facts' gesammelt, die mit Physik nichts zu tun haben und auf die ich ohne euch wohl auch nie gestoßen wäre.

Darüber hinaus möchte ich mit bei Prof Dr Ludwig Mathey bedanken, der die Erstellungen des Zweitgutachtens zu dieser Arbeit übernommen hat.

Außerdem bedanke ich mich bei meiner Familie und meinen Freunden, die mich ebenfalls während der Dauer dieser Masterarbeit unterstützt haben.

Eidesstattliche Erklärung

Hiermit bestätige ich, dass die vorliegende Arbeit von mir selbständig verfasst wurde und ich keine anderen als die angegebenen Hilfsmittel – insbesondere keine im Quellenverzeichnis nicht benannten Internet-Quellen – benutzt habe und die Arbeit von mir vorher nicht einem anderen Prüfungsverfahren eingereicht wurde. Die eingereichte schriftliche Fassung entspricht der auf dem elektronischen Speichermedium. Ich bin damit einverstanden, dass die Masterarbeit veröffentlicht wird.

Hamburg, den December 5, 2016 _____